DEVELOPMENT OF A NOVEL BALLOON-MESH DEVICE TO IMPROVE THE EMBOLIZATION OF ANEURYSMS

By Omid Asgari

A Dissertation

Submitted in Partial Fulfillment

of the Requirements for the Degree of

Doctor of Philosophy

in Bioengineering

Northern Arizona University

October 2023

Approved:

Timothy Becker, Ph.D., Chair

Gabriel Montaño, Ph.D.

Hesam Moghaddam, Ph.D.

Zhongwang Dou, Ph.D.

ABSTRACT

DEVELOPMENT OF A NOVEL BALLOON-MESH DEVICE TO IMPROVE THE EMBOLIZATION OF ANEURYSMS

OMID ASGARI

The rupture of an intracranial aneurysm is the cause of death for 500,000 people each year, with half of them being younger than 50 years old. It is estimated that 3-6 million Americans harbor a brain aneurysm and thus are at risk from this condition. While the neurointerventional field has progressed dramatically over the past few years, existing embolization devices suffer from significant limitations. Major challenges to successful treatment of brain aneurysms of varying sizes and geometries include ensuring the aneurysm sac remains occluded in the long-term (reducing recanalization risk) while avoiding downstream thrombus and subsequent ischemia. A supporting medical device that can improve the efficiency of aneurysm treatment, without significantly affecting parent artery blood flow, is needed.

The purpose of this translational research is to develop and validate an endovascular device – Balloon-Mesh – which improves aneurysm neck protection during embolic device placement and reduces blood flow obstruction in the parent artery, thereby minimizing ischemic risk. This project includes two aims. Aim I, a design, validate, and manufacture a new prototype w. Aim II, test the efficacy of the prototypes as in an *in-vitro* model and compared to current commercial devices. The prototypes were be delivered to our portable blood flow system utilizing simulated

neurointerventional surgical techniques under fluoroscopic imaging, coordinated by the Bioengineering Devices Lab (BDL) at NAU.

This device has the potential to alleviate current time constraints imposed by temporary balloon protection, provide a smooth surface at the aneurysm neck for consistent device placement, eliminate ischemic effects distal to the parent artery, and minimize intra-aneurysmal flow remnants pre- and post-treatment.

Acknowledgments

I want to express my gratitude to the many individuals and organizations who have been instrumental in my academic endeavor from start to finish. First, I would like to thank my academic advisor, Dr. Timothy Becker, for giving me the opportunity to be a part of the Bioengineering Device Lab (BDL) and for being a steadfast pillar of support throughout this journey. Dr. Becker's guidance not only helped me grow academically but also provided a supportive and welcoming environment.

I am thankful for the guidance and feedback from my committee members, Dr. Gabriel Montano, Dr. Hesam Moghaddam, and Dr. Zhongwang Dou, throughout my PhD program. Their assistance was invaluable in shaping my dissertation.

I am also appreciative of the financial contribution from Aneuvas Technologies, Inc., the Flinn Foundation, and the Brain Aneurysm Foundation, which played a crucial role in my research. Additionally, I would like to thank Pivot Medical for their assistance in developing and prototyping the Balloon-Mesh device.

My time at the BDL was enriched by the friendships and encouragement of my friends and lab mates, who became like a second family to me. The memories we created together, from my first day to my last, will always hold a special place in my heart.

Last but not least, I want to extend a special and heartfelt appreciation to my dear wife, Dr. Sara Sadeghpour. Her unwavering support and countless sacrifices throughout my PhD journey have been nothing short of remarkable and have been the driving force behind my successful completion of this dissertation. During the highs and lows of my PhD program, my wife was consistently there for me, offering encouragement and unwavering belief in my abilities. I also

want to express how much I miss my parents and siblings, whom I have not seen since starting my PhD program. The sacrifices we all made to get me here mean the world. They continuously went above and beyond to ensure that I had the support and encouragement I needed to persevere.

Omid Asgari

Table of Contents

List of Tables

List of Figures

CHAPTER 1 – BACKGROUND AND SIGNIFICANCE

Aneurysm

An aneurysm, having an outward ballooning or bulge shape, is an abnormal enlargement on the vessel wall. An aneurysm is formed on the weakened segment of the vessel. Forming and growing an aneurysm results in a thinner and weaker vessel wall, which is prone to rupture.[1–3] Any vessel can have aneurysms, however, aortic and brain (cerebral) vessels are more commonly considered for treatment (**Figure 1**). Rupture of an aortic aneurysm can result in massive, often fatal, internal bleeding. When Intracranial Aneurysms (IA) – aneurysms on brain vessels – rupture, they can lead to bleeding in the subarachnoid space, where cerebrospinal fluid (CSF) circulates, thereby increasing the intracranial pressure and resulting in Subarachnoid Hemorrhage Stroke (SAH) and related complications. The SAH is frequently fatal and when not, often produces significant permanent morbidity.[3,4]

Figure 1: Aortic aneurysm[5] (right), intracranial aneurysm[6] (left).

It is estimated that 3-5% of the adult population worldwide has an Unruptured Intracranial Aneurysm (UIA),[2,4,7] most prevalent in people ages 35 to 60. Approximately 20-30% of people with UIA have more than one aneurysm.[4,7] In the United States, approximately 6.5 million people have UIAs (1 in 50 people). Each year, 30,000 people in the United States suffer a rupture of IA, which means an IA ruptures every 18 minutes. Annually, about 500,000 people die from IAs worldwide, half of which are younger than 50 years of age. After IA rupture, half of these people die. 15% of these patients die before they reach the hospital, due to the fact that aneurysms often

go unnoticed. About 66% of those who survive a ruptured aneurysm suffer permanent neurological damages (**Figure 2**).[7] In general, women have more intracranial aneurysms and are more prone to rupture aneurysms (ratio 3:2).[7,8]

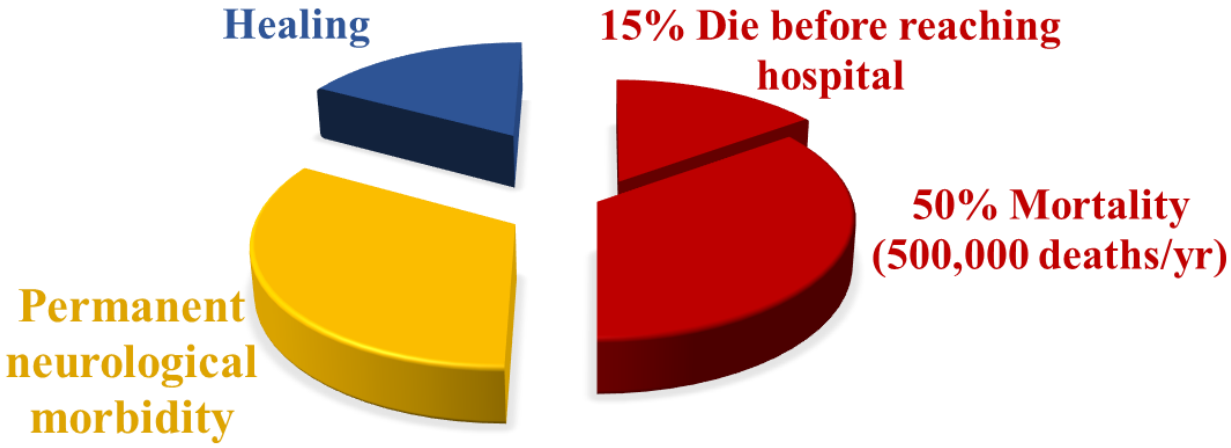

Figure 2: Morbidity and mortality rates associated with rupture aneurysms.

Formation, Growing, and Rupture of an Aneurysm

Intracranial aneurysm formation process involves pathological changes of vessel wall structures due to presence of predisposing genetic, environmental, and other risk factors. Although the exact process of aneurysm formation is not completely understood, hemodynamic stresses, hypertension, and history of smoking are the main risk factors for UIA development. Additionally, patients with first-degree relatives with UIAs and previous SAH are 3 times more likely to develop UIAs.[3]

The cerebral vascular system, compared to cardiovascular systems, has an extremely thin tunica adventitia, the 3rd layer of vascular wall. The density of elastic fibers in tunica media, the second layer of vascular wall, is also lower. In addition, cerebrovascular flow system is surrounded by the subarachnoid cerebrospinal fluid system. Due to lack of external elastic lamina, located

between tunica media and adventitia, the internal elastic lamina (IEL), located between the tunica media and tunica intima - is responsible for maintaining the structural framework of vessel wall.[3] IEL damage, initiated by hemodynamic stress, will affect vessel wall elasticity, leading to the development of a cerebral aneurysm.[3] Vascular smooth muscle cells (SMCs), located in tunica media, begin to grow at the IEL tear, which represents an adaptive response to vessel wall damage. Additionally, endothelial cell (EC) death leads to luminal surface abnormalities. Furthermore, an aneurysm with an IEL and EC disfunctions as well as disorganization of SMCs exhibits a significant vessel wall weakening, increasing the likelihood of aneurysm growth and a rupture event.[3] (**Figure 3**).

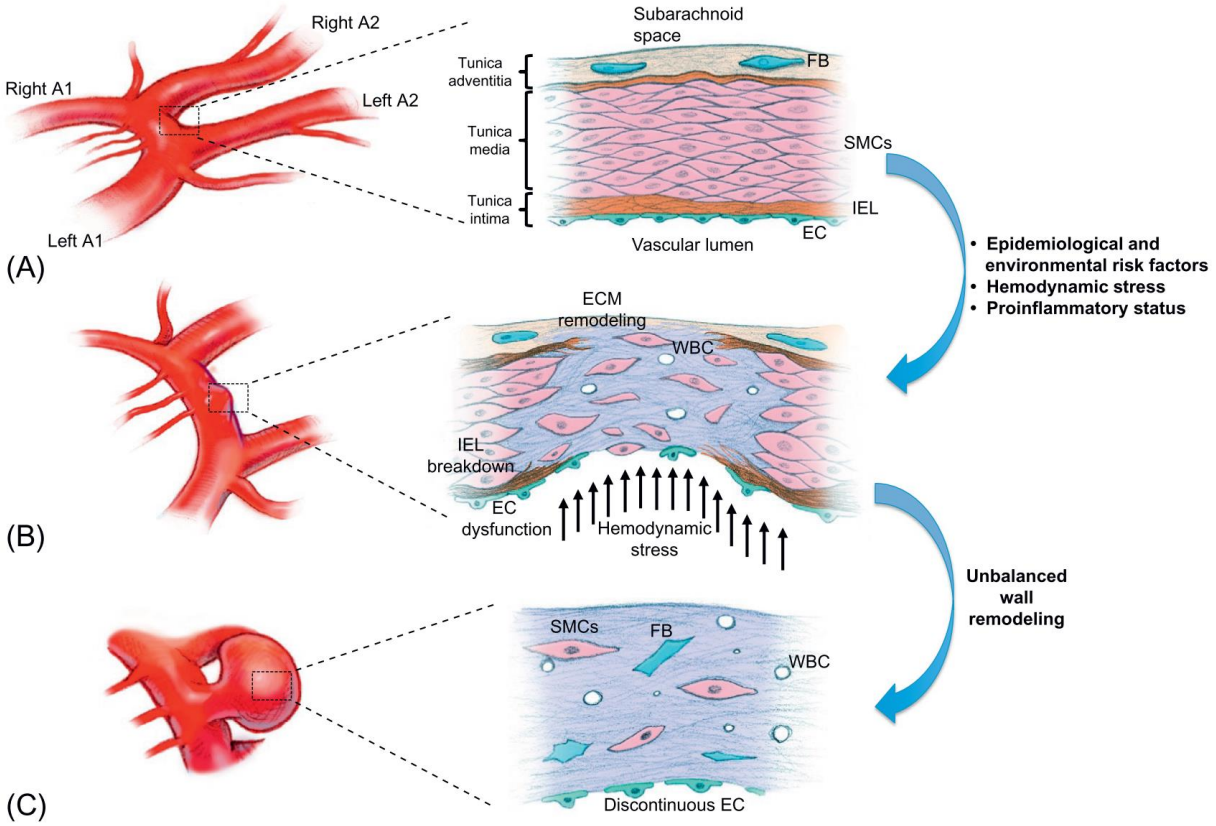

Figure 3: Formation and growth of a cerebral aneurysm.[3]

Aneurysm Classification

Intracranial Aneurysms can be grouped by size, anatomical location, and morphology.[9] The size of aneurysms less than 10 mm are considered small aneurysms. Aneurysms with a size of 10-25 mm and more than 25 mm are considered large and giant aneurysms, respectively.[9,10] **Figure 4** shows these anterior and posterior circulations in the Circle of Willis. Circle of Willis is a ring-like structure in the base of the brain, connecting the anterior and posterior arteries. It plays a crucial role by providing collateral circulation, ensuring a sufficient blood flow to the entire brain even in the event of interruption.[11] An aneurysm can be located in both anterior and posterior vessels of the CW – including internal carotid artery (ICA), middle cerebral artery (MCA), anterior communicating artery (ACoA), and posterior communicating artery (PCoA), vertebral artery (VA), posterior inferior cerebellar artery (PICA), basilar artery (BA), superior cerebral artery (SCA), and posterior cerebral artery (PCA) aneurysms.[9]

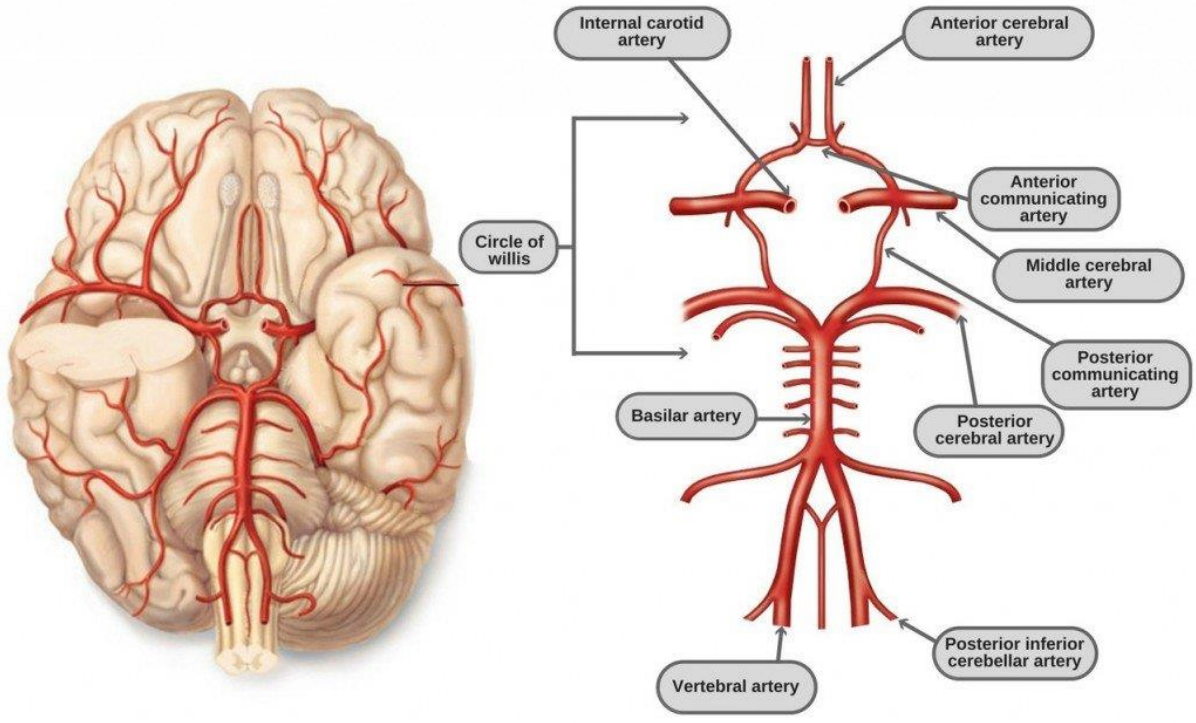

Figure 4: Anterior and Posterior circulations of arteries in the brain (Circle of Willis). [11]

Based on morphology, Intracranial Aneurysms are classified as saccular, fusiform, or dissecting aneurysms.[9] Saccular aneurysms, the most common morphology of intracranial aneurysms, have a neck that connects the dome of the aneurysm to the parent artery and are divided into two categories – sidewall and bifurcation – based on the location of the aneurysm. Fusiform aneurysms, rare in the brain (about 6% of all Intracranial Aneurysms) and often located in MCA (48%), do not have a neck and involve 180-360˚ circumference of arteries.[12] Dissecting aneurysms result from longitudinal tears in the vessel wall and represent 3% of all intracranial aneurysms).[13,14]

Current Embolization Techniques

Rupture of an aneurysm results in bleeding into the subarachnoid space, between the dura matter lining the skull and pia matter covering the brain (**Figure 5**).[15,16] The main goal of treating an intracranial aneurysm is to prevent rupture of the aneurysm and thereby preventing the subarachnoid hemorrhage (SAH).[17]

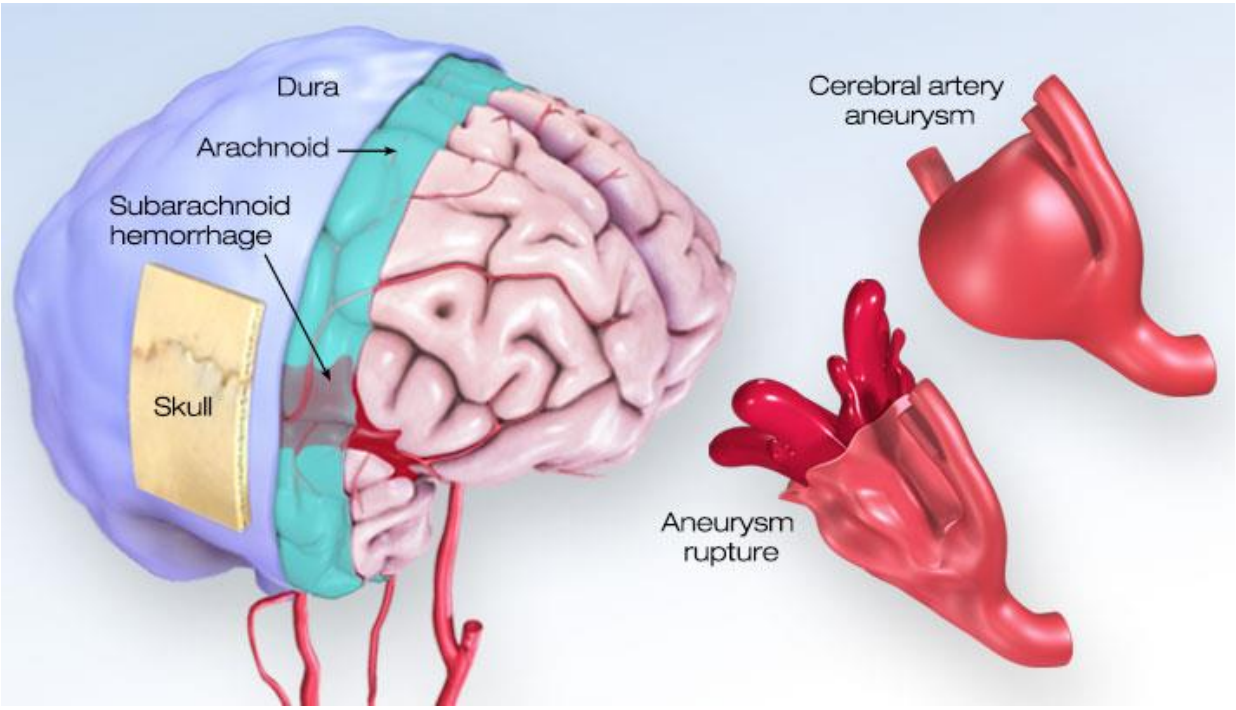

Figure 5: Rupture of intracranial aneurysm results in bleeding in subarachnoid space (SAH).[16]

Microsurgical clipping: Microsurgical clipping was introduced in 1937 as the first method of the treatment of intracranial aneurysms. The main goal of microsurgical clipping is to maintain blood flow in the parent artery and eliminate the aneurysm from circulation by placing a microsurgical clip at the aneurysm neck. The microsurgical clipping technique is an invasive method of surgery, and postoperative antiplatelet therapy is neccessary.[18,19] Craniotomy with clipping can be used for both ruptured and unruptured aneurysms, however, improved brain imaging and endovascular device technology led to an established role of minimally invasive methods for treating of aneurysms.[17] An alternative to clipping is delivery of embolic devices from inside the vessel (endovascular). Current endovascular embolic devices include:

Coil Embolization: Coil embolization was introduced in 1989 as a minimally-invasive method of treating an intracranial aneurysm. Minimally invasive methods increased the patient outcome, decreased the hospital stay time for patient, and decreased the mortality rate. However, the endovascular treatment involves significant such as vessel/aneurysm perforation and thromboembolic strokes.[20]

Initially, coiling was limited to small aneurysms with a narrow neck, however, by improving the adjunctive devices – balloons and stents, coiling was used to treat wide-neck sidewall aneurysm as well as bifurcation aneurysms.[17] The coil embolization method, in which an aneurysm with a small and medium dome-to-neck ratio is filled with platinum-based metal coils in order to reduce the intra-aneurysmal flow, is the "gold standard" method of treating intracranial aneurysms but is not as effective for wide-neck and large aneurysms. Coil embolization requires a delivery catheter placed inside the aneurysm sac in order to deploy coils. The coiling procedure is continued until forming a dense pack of coils inside the aneurysm until there is no evidence of intra-aneurysmal flow. It has been reported that primary coiling is limited by the low volume

packing of aneurysms (< 30%) and high recanalization rates.[21,22] Recanalization rates for small-neck aneurysms (dome to neck ratio > 2:1) are 15-35%, whereas wide-neck aneurysms (d:n < 2:1) rates are as high as 70%.[23] Complex and wide-neck aneurysm treatment with coils is difficult because their shape rarely keeps the coils inside the aneurysm sac, thereby increasing the risk of coil migration of and blockage of the parent artery.

Flow Diversion: Flow diversion is a novel treatment technique based on two concepts: First, flow diverters, braided stent devices with well-defined mesh density, divert blood away from entering the aneurysm sac by creating an impedance/cover. This is supposed to generate a stasis flow in the aneurysm sac, which can lead to the formation of thrombus within the aneurysm sac. Second, flow diverters are supposed to act as a scaffold for neoendothelization at the aneurysm neck, leading to vessel wall remodeling. However, in tortuous vessels, flow diverters (i.e., Pipeline®) can be difficult to navigate, deploy, and expand. Resulting aneurysm flow stasis and neck endothelialization results are also inconsistent. Flow diverters also have limited utility in bifurcation aneurysms. Therefore, flow diverters are currently approved for internal carotid artery use, proximal to the circle of Willis (CW).[23–27] Moreover, patients treated with flow diverter must remain on dual-antiplatelet therapy, which limits use of flow diverters with ruptured aneurysms.[28–34]

Flow Disruption: Flow disruption technology, which has been developed for treating wide-neck bifurcation aneurysms, was first introduced into clinical practice in 2011.[35] The main concept of flow disruption technique is the same as a flow diversion technique. However, the flow disruption device is located inside the aneurysm sac disrupt intra-aneurysmal flow.[36–42] Therefore, the formation of neoendothelization in the aneurysm sac and along the aneurysm neck/vessel is supposed to exclude the aneurysm from circulation. Since the flow disruptor is an intra-aneurysmal

device located inside the aneurysm sac, dual antiplatelet therapy (DAPT) is not required. The flow disruption technique is suitable for treating both rupture and unruptured aneurysms.[43–45]

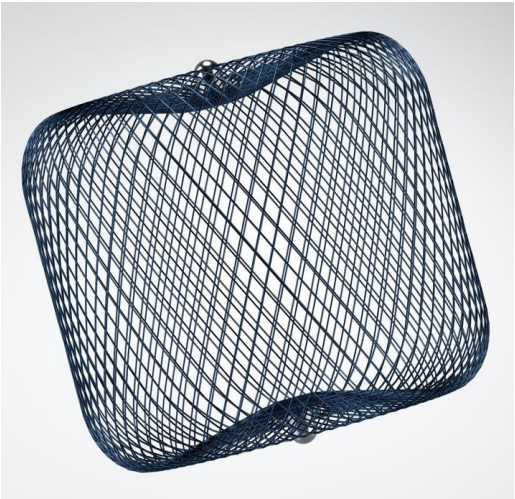

Figure 6: Woven EndoBridge device.[46]

The Woven EndoBridge (WEB, Microvention, Alliso Viejo, CA) – a self-expandable braided nitinol mesh – is currently the only FDA-approved flow disruptor for treating simple-shaped, small wide-neck aneurysms ranging 3 mm to 10 mm (**Figure 6**).[47] The delivery system is very stiff, which creates challenges for placement in complex or distal vasculature. Placement often results in residual filling at the aneurysm neck, possibly leading to recanalization.

Liquid Embolic: A liquid embolic is a new method of treating intracerebral aneurysms, which uses a delivery microcatheter to inject the liquid agents into the aneurysm sac. Liquid embolics can fill 100% of the aneurysm sac, and after solidifying, there is no intra-aneurysmal flow. In comparison, coil embolization can only fill 30% space of the aneurysm sac, leaving 70% of the space susceptible to residual flow or thrombus formation.[21,22] By placing a temporary balloon device across the aneurysm neck, liquid embolics can be injected without migrating liquid materials into the parent vessel and blocking downstream vessels. There has been some concern that previous **liquid embolics** (i.e., Onyx HD-500®) are cytotoxic and unstable within the aneurysm sac.[48–56] A more effective liquid embolic delivery could be implemented by the use of temporary balloons, fine mesh stents, or metal coils (to hold the embolic in place until it solidifies), but the data on their effectiveness have been limited to this point.[57–63]

Adjunctive devices: Stents or temporary balloons can be used as adjunct devices to facilitate the delivery of embolization agents such as platinum coils or liquid embolics into the aneurysm sac. As part of both balloon- and stent-assisted embolization techniques (**Figure 7**-Error! Reference source not found.), adjunctive devices are placed in the parent artery in front of the aneurysm neck in order to provide support during the embolization process.

Balloon-assisted technique: With the use of a temporary balloon, a smooth surface can be created at the neck of the aneurysm to facilitate remodeling of the vessel wall by providing a smooth surface at the neck – serving as a scaffold for tissue growth. However, having an inflated balloon in the parent artery occludes the blood flow in the artery, which causes an increase in ischemic events.[64] Onyx, although it is no longer widely used, sets a precedent for temporary occlusion with multiple inflations and deflations (every 5 minutes to prevent ischemia). Inflation/deflation cycles, however, result in vessel trauma and potential embolic device migration.[65] Nevertheless, temporary ultra-compliant urethane balloons and coatings provide consistent aneurysm neck protection and eliminate the need for dual antiplatelet therapy, which is particularly useful in the treatment of ruptured aneurysms. During device delivery, the balloon isolates the delivery microcatheter (jailed catheter) in place, minimizes migration of the device, and avoids placement of permanent stents in the parent artery. However, ischemia remains a significant limitation when temporary parent artery occlusion is used with coils or liquid embolic materials.

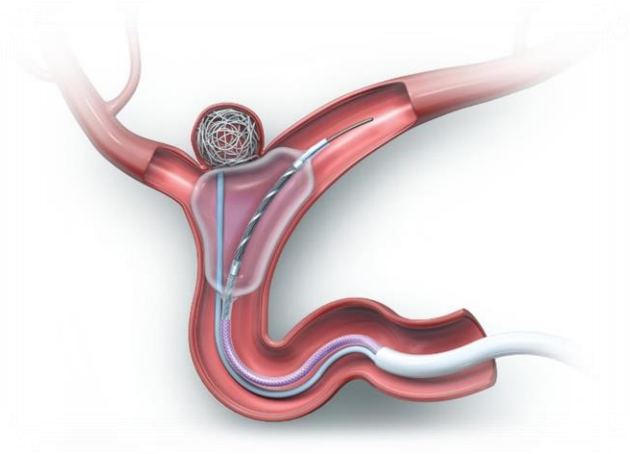

Figure 7: Balloon-assisted coil embolization.

Stent-assisted technique: The stent-assist embolization technique allows easy blood flow through the parent artery, but it cannot completely protect the neck of the aneurysm. While retrievable stents (Comaneci®) exist, their large pores do not consistently protect aneurysm necks from coils and liquid embolics without potentially protruding into the parent vessel or entangling with the stent. Significant rates of vasospasm, vessel damage, and thrombo-embolic complications are associate with using this permanent device.[66,67] Stent-assisted coiling requires to dual antiplatelet therapy, which limits its use in ruptured aneurysms.[28–34,68]

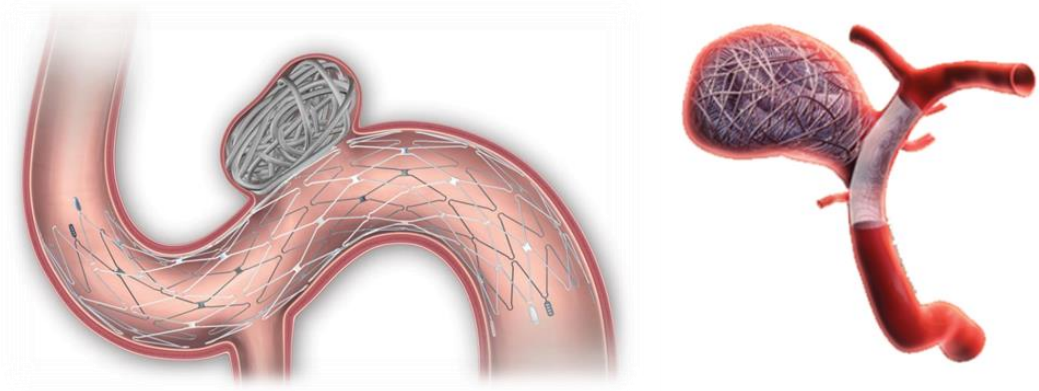

Figure 8: Stent-assisted coil embolization (left). A flow diverter can also be used for assessing the coil embolization procedure (right).

Initial Balloon-Mesh Design

The success of adjunctive medical devices depends on their ability to maximize uniform coverage across the aneurysm neck during placement and minimize device interactions with the parent artery (avoiding distal ischemia and reducing the need for dual antiplatelet therapy). The balloon-mesh device (**Figure 9**) has the potential to increase the effectiveness of vascular neointimal healing at the neck by providing a more complete treatment of the aneurysm sac with an embolic device, thereby reducing long-term recanalization rates.[61,63,69–72] It is hypothesized that this translational research leads to the development of a balloon-mesh device that can temporarily protect aneurysm necks during complementary device deployment, maintain blood flow in the parent artery, maximize device placement in the aneurysm sac, provide a smooth surface at the neck for neointimal vessel healing, prevent device migration into the parent artery in the short-term, and reduce the rate of recanalization in the long term.

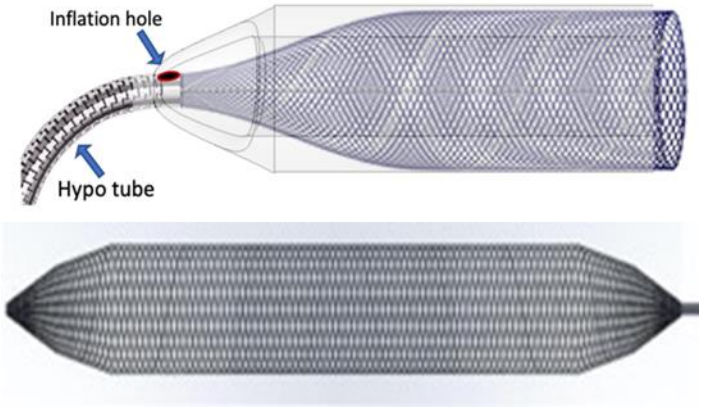

Figure 9: Balloon-mesh designs –**Top**: balloon coating inflated from the attached hypotube, **Bottom**: braided fine mesh with a conformable "balloon" shape.

The initial balloon-mesh design (**Figure 9-Top**) is composed of an ultra-compliant urethane balloon coating over a small self-expandable and retrievable nitinol braided stent/mesh (3-5mm expanded diameter). The balloon-coated stent/mesh is connected to a microwire/hypotube and can

be delivered through various 2.5-3F microcatheters.[73–76] Blood flow in the parent artery is maintained through the deployed stent and the balloon coating provides a smooth-consistent seal along the aneurysm neck and parent vessel wall. Blood flow in the parent artery is maintained through the deployed stent and the balloon coating provides a smooth-consistent seal along the aneurysm neck and parent vessel wall.

The second design is nitinol fine braided mesh (**Figure 9-Bottom**). It is designed to be both retrievable and self-expandable forming a mesh with a balloon-like shape. The mesh is connected to a microwire/push wire and can be delivered and retrieved from various 2-3F microcatheters.

To deliver the embolic device (such as coils, liquid embolics, or flow disrupters), a microcatheter is placed in the aneurysm sac. The adjunctive device (balloon-mesh device) is inserted across the neck of the aneurysm in the parent artery. Upon expansion of the stent/mesh from the microcatheter tip, the microcatheter is retracted and the balloon-mesh expands across the aneurysm neck (**Figure 9-Bottom**). In the case of initial design (**Figure 9-Top**), the ultra-compliant balloon coating can be inflated via the hypo tube to conform to various aneurysm neck types, providing aneurysm neck protection and "jailing" the delivery microcatheter between the parent artery and the adjunctive device. By using the delivery microcatheter, an embolic device is then inserted within the aneurysm sac. Providing a continuous and smooth surface at the aneurysm neck allows device delivery to be contained, minimizing the risk of device migration downstream, and minimizing aneurysmal inflow/outflow. In addition, the stent component provides an open path for continuous blood flow through the parent artery. Following aneurysm treatment, the jailed microcatheter is removed, the balloon coating from the hypo tube is deflated (if inflated), and the stent/mesh is retrieved into the end of the microcatheter. This balloon-mesh device is designed for 3-5 mm diameter parent arteries with sidewall aneurysms (**Figure 10B**). Nonetheless, with ultra-

compliant balloon options that conform to the vessel shape, placing the balloon-mesh in the parent artery and inflating it across the neck of a bifurcation aneurysm is possible. Even though the Scepter-XC/Hyperform balloon or the Comaneci device can provide similar coverage, the balloon-mesh device can maintain the parent artery flow in a primary vessel branch (**Figure 10A**).

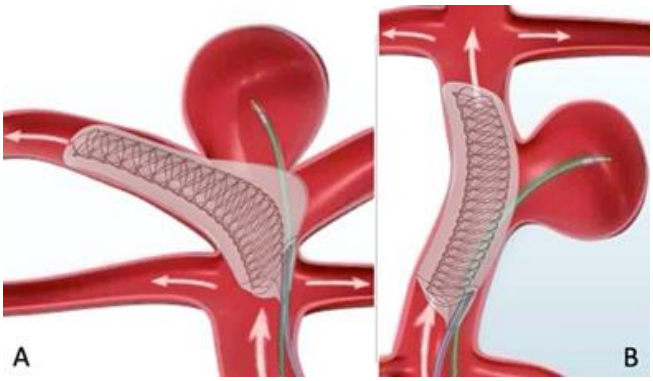

Figure 10: Anterior and Posterior circulations of arteries in the brain (Circle of Willis)

In neurointerventional surgery, one of the most challenging aspects is completing the treatment of aneurysms within a short period of time and minimizing long-term recanalization risk. It is essential to have a complementary medical device that supports the embolization procedure without interfering with the blood flow of the parent artery. In this translational research project, we describe the development and testing of novel adjunctive temporary device, Balloon-Mesh, (submitted **US Provisional Patent #63176122)**, which provides a protective and cohesive surface at the aneurysm neck while minimizing the risk of downstream ischemic events.

Aims and Hypotheses of Research

In spite of the significant progress made in the field of neurointerventional surgery over the past few years, existing embolization devices have significant limitations. Successful treatment of brain aneurysms of varying sizes and shapes includes preventing downstream thrombo-embolic and ischemic events, which are often associated with stent devices, and ensuring the sac remains occluded in the long term. There is a need for a medical device that can improve aneurysm

treatment efficiency while maintaining parent artery blood flow (unlike temporary balloon remodeling). Adjunctive stent devices (temporary or permanent implants) maintain parent artery flow but can cause negative interactions with embolic devices placed in the aneurysm sac: such as entanglement, protrusion, migration, and downstream particulation. Thus, adjunctive stenting requires long-term dual antiplatelet therapy in order to reduce the risk of ischemic complications. Using temporary balloon protection, aneurysm treatment efficiency and device placement are improved by creating a seal at the aneurysm neck. There is no requirement for dual-antiplatelet therapy in the case of temporary balloons, but balloon obstruction can cause distal ischemia. Therefore, ***developing a device that improves the effectiveness of aneurysm treatment while maintaining adequate blood flow in the parent arteries is necessary***.

The project is based on a solid foundation of modeling, manufacturing technology, and clinical expertise. In order to develop a medical device, we leveraged the medical device development experience of Aneuvas Technologies Inc. (ATI), the computer and neurovascular modeling experience at the NAU-BDL, prototyping experience of Pivot Medical, and clinical experience of Barrow Neurological Institute (BNI).

This translational research aimed to ***develop, build, and validate an endovascular device that improves aneurysm neck protection during embolic device placement, while reducing blood flow obstruction in the parent artery and minimizing ischemic risk***. The main objective of this research was divided into two aims:

Proposed Aim I

Design, model, and build a novel balloon-mesh prototype for endovascular treatment of aneurysms.

Current adjunctive stent devices that are implanted maintain the downstream perfusion, but are susceptible to entanglement, protrusion, migration and downstream particulation. To reduce downstream thrombo-embolic risks associated with stents, patients should receive dual-antiplatelet therapy for a prolonged period of time. Temporary compliant balloons, which seal embolic materials in place during delivery without requiring dual antiplatelet therapy, can induce downstream ischemia due to the temporary obstruction of parent-artery blood flow.

Hypothesis 1: *We hypothesize a novel endovascular device can be designed and optimized utilizing computational fluid dynamic (CFD) as well as benchtop testing techniques to create a prototype that maximizes blood flow perfusion past the device during device placement and minimizes flow into the aneurysm by protecting the aneurysm neck.*

We verified device designs that maximized aneurysm neck protection and maintained parent artery flow. These designs were manufactured into prototype devices that minimize intra-aneurysmal flow and reduce downstream thrombo-embolic risk during embolization procedures. This aim involved the development of a novel endovascular device, the balloon stent, involving a three-step process:

Step 1: Computational fluid dynamics modeling (CFD). A balloon-mesh design was modeled based on a device ID to the parent artery ratio (levels: 1.0 - 0.25) variable to analyze the resulting flow effects. The level of 1.0 represents the best-case scenario: an uninflated balloon or an fully expanded stent. An ID of 0.25 represents the worst-case scenario: an overinflated balloon, or a narrowed stent. According to the literature, pulsatile flow waveforms were prescribed for vessel inlets. High-resolution hemodynamic data was obtained by solving the Navier-Stokes equation with SimVascular software. Monsoon®, NAU's high-performance computing cluster,

was utilized to perform the simulations. We compared preliminary CFD calculations of the parent artery flow rate and pressure changes to guidelines for fractional pressure ratios (FFRs).

Step 2: Bench-top testing. BDL team have developed sophisticated 3D-printed *in vitro* vessel models that are controlled by a programmable, digitally controlled hydraulic pulsatile pump (SuperPump AR, ViVitro Labs). Blood analog exits the programmable pump, enters the vessel model, and returns to the pump. With the help of real-time pressure data, the model function has been validated. A similar approach to CFD modeling was utilized to model the flow effects caused by the balloon-mesh device with respect to the ratio of the ID of the device to the ID of the parent artery (level: 1.0 - 0.25). A comparison was made between real-time pressure and flow data resulting from bench-top tests and CFD results as well as FPR guidelines. The results provided the balloon-mesh size range that addresses the minimized ischemia risk due to the interruption of flow.

Step 3: Prototyping the balloon-mesh device. The balloon-mesh designs with optimal CFD and bench-top results was manufactured in collaboration with resources from Barrow Neurological Institute (BNI), NAU's Bioengineering Device Laboratory (BDL), Aneuvas Technology Inc. (ATI), and Pivot Medical, and prototypes optimized to meet or exceed acceptance testing and validation criteria – in comparison to existing control devices.

Proposed Aim II

Assess, optimize, and validate the effectiveness of balloon-mesh prototypes in an *in vitro* aneurysm model, and test the prototypes for mechanical integrity.

A current *in vitro* model does not accurately simulate both the mechanical properties of the human vessel wall and the flow characteristics of the vessel. The importance of verifying the flow effects in specific vessel branches and adjusting the flow resistance in accordance with the human condition is often overlooked. The testing of a new device that minimally affects local blood flow

when deployed, however, requires a model system that is capable of detecting minute changes in the flow of blood within a vessel.

Hypothesis 2: *We hypothesize that the prototype can be tested in a physiologically-relevant benchtop flow model and provide aneurysm neck protection while maintaining blood flow in the parent artery, which maximizes aneurysm sac treatment during complementary device deployment and prevents device entanglement or device migration into the parent artery. In this study, the complex hemodynamics of cerebral vessels can be monitored and analyzed with the benchtop model to provide insights into endovascular aneurysm treatments.*

This proposed aim took a four-step approach to characterize the mechanical integrity of the balloon-mesh prototypes and evaluate the ease of device delivery, the hemodynamic effects, and efficacy of the prototypes implanted in an *in-vitro* model.

Step 1: Prototype delivery testing. The delivery, extract, inflation/deflation, and retraction of the prototypes were tested in the level 1.0 model (ID = 4mm) in order to assess the ease of prototypes delivery/retraction of the prototypes. All the results were compared with control devices.

Step 2: *In-vitro* CW Tests. CW The functionality and integrity of balloon-mesh prototype were tested in the 3D-printed advanced *in vitro* model (clinically derived model that incorporates a blood analog, both with material properties that approximate the human condition). The use of *in vitro* modeling allowed us to supplement the current understanding of endovascular medical devices by proposing new insights into their deployment and their effect on local human vessels. Pressure and flow effects were monitored in individual vessel branches during and after balloon-mesh prototype delivery for comparison to control device deliveries and FPR guidelines. This data can be used to optimize the final balloon-mesh design. It is anticipated that a working prototype,

with ease of delivery and retrieval (when compared to control devices), offers superior aneurysm neck protection, combined with patent parent artery flow.

Step 3: Mechanical integrity testing. Tracking force (push/pull) tests using a setup previously validated by the FDA, and radial force testing were performed and we compared the results with control devices/

Step 4: Aneurysm Neck Coverage Evaluation. Placement of aneurysm treatment device in conjunction with the balloon-mesh device. While the prototypes and control device were placed across the aneurysm neck in the CW model a contract material injected and the fluoroscopic imaging were utilized to evaluate the aneurysm neck coverage of devices.

CHAPTER 2 – AIM I

Aim of Research

Design, model, and build a novel balloon-mesh prototype for endovascular treatment of aneurysms.

Hypothesis: *We hypothesize a novel endovascular device can be designed and optimized utilizing computational fluid dynamic (CFD) as well as bench-top testing techniques to create a prototype that maximizes blood flow perfusion past the device during device placement and minimizes pulsatile flow into the aneurysm by protecting the aneurysm neck.*

Introduction

In the complex field of neurovascular disease assessment and the development of endovascular devices, precise blood flow evaluation is essential. This study presents a comprehensive exploration of different testing methodologies utilized to assess the significance of blood flow and pressures in ischemic risk evaluation. By employing different approaches, this investigation highlights the strengths and limitations in theoretical calculations, numerical CFD simulations, and the accuracy offered by an advanced bench-top system. The results illuminate the potential synergy among these methods in increasing our understanding of neurovascular defects, thereby contributing to the progression of balloon-mesh device designing and development. The primary objective of this initial study was to show the flow effects within cerebral arteries resulting from variations in vessel flow resistance.

Fractional Pressure Ratio (FPR)

An understanding of the fractional pressure ratio is crucial for determining the appropriate size of the balloon-mesh device, thereby ensuring sufficient blood flow downstream. After implanting the balloon-mesh device, blood flow will be restricted, which is similar to the loss of pressure in a vessel as a result of stenosis (**Figure 11**). Fractional Flow Reserve (FFR) was proposed by Pijls et al. as a lesion-specific index of functional severity in coronary artery disease (CAD) more than 20 years ago and has been the subject of numerous studies investigating its use in both invasive and non-invasive assessment of CAD. The FFR is the ratio of maximum flow in coronary artery stenosis to maximum flow in the same territory without a stenosis. FFR, taken at hyperemia, can also be calculated using distal pressure and aortic pressure (P_d/P_a).[77] Fractional Pressure Ratio (FPR), driven from FFR, is the criteria for evaluating neurovascular stenosis.[78] The unique physiology of the cerebrovascular system, characterized by complex collateral circulation and blood flow regulation mechanisms, poses challenges in assessing cerebrovascular disease compared to cardiovascular disease, and thus, there is a need to explore new and reliable methods for evaluating the functional severity of cerebral stenosis.[79] FPR, the ratio of distal to proximal pressures across neurovascular stenosis, can be measured at rest, which reduces the risk of patient neurovascular flow disruptions and the potential for hyperemic stimuli in cerebral arteries. FPR of 1 indicates that there is no loss of pressure in an artery due to a restriction. Moreover, an FPR of 0.75 is an acceptable threshold, and below that is considered an ischemic risk (FPR < 0.75 or $\Delta P > 25\%$). Therefore FPR, with a $p_d/p_p \geq 0.75$, is a strong indicator of patent artery flow and was used to determine the acceptable

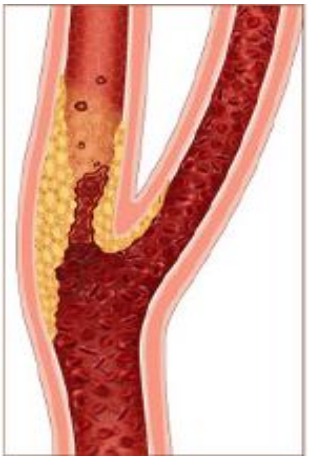

Figure 11: Stenosis. FPR is the proximal to distal pressure ratio across neurovascular stenosis

dimensions of a balloon-mesh device. FPR can be measured either invasively or non-invasively, similar to the measurements of FFR. In the invasive method, a pressure monitoring wire is used to obtain two pressure waveforms across a neurovascular stenosis, one at the proximal end and the other at the distal end. This method carries a significant risk of morbidity and mortality due to its invasive nature.[80] On the other hand, non-invasive measurement can be performed using computational fluid dynamics (CFD) simulations based on 3D anatomical modeling of pulsatile blood flow in neurovascular arteries to understand the hemodynamics of stenosis. This method offers a safer and non-invasive alternative to invasive measurements, making it a promising technique for clinical use.[78,80] Additionally, it has the potential to provide more detailed information about the blood flow and its changes in response to stenosis, which may not be possible with invasive methods. FPR has been a key design parameter for justification of the balloon-mesh device safety in the future FDA submission.

Although numerical techniques such as computational fluid dynamics (CFD) have been utilized in numerous studies to investigate the hemodynamics of vessels, very few studies have comprehensively assessed the hemodynamics of vessels in a real physiological representative environment. The lack of research in this area is a significant drawback that limits our understanding of the physiology of vessels, which is crucial for developing a new endovascular device and treatment methods for vascular diseases. Therefore, there is a need to conduct more studies that explore the hemodynamics of vessels using realistic models and accurate techniques. Our research group has designed a benchtop system that is capable of simulating the physiological properties of a human vasculature system. To the best of our knowledge, this system is unique, and it is the only benchtop system that can measure real-time physiological parameters.

We established an FPR baseline using idealized cerebral stenoses and evaluated the hemodynamics to gain a better understanding of the flow disruption effects using three different methods – theoretical estimation, CFD, and benchtop modeling. These results aimed to enhance our understanding of the potential flow disruption effects resulting from different balloon-mesh designs. The evaluation of hemodynamics and pressure differences across the stenoses and endovascular devices is crucial for predicting not only potential vascular diseases and identifying suitable treatment plans, but also for understanding device development and optimizing designs.

Methods

To accomplish the objectives of this study, we used three different methods for assessing the hemodynamic of blood. The first method involved theoretical estimation by utilizing the Hagen-Poiseuille equation (simplification of Navier-Stokes accounting for viscosity effects). Next, we conducted Computational Fluid Dynamics (CFD) modeling for idealized stenoses. Finally, we analyzed the hemodynamic data for the same idealized stenosis utilizing an advanced bench-top system.

Theoretical Estimation

Hagen-Poiseuille flow equation **(1)** can be used to calculate the pressure drop/FPR. From **(1**, the variables affecting vessel resistance (R) are vessel length (L), vessel diameter (ID), and blood viscosity (μ) – **(2**. These flow resistance changes can occur slowly from vessel stenosis buildup, thrombosis, embolism, or even rapidly from temporary balloon occlusion.[81,82] These variables also influence new balloon-mesh design (L - device length, ID - stent diameter). Therefore, pressure drop (ΔP, pressure proximal (p_p) minus pressure distal (p_d)) and flow rate (Q) can be calculated (for vessels of the CW or for a balloon-mesh prototype) which depends on the length and inner diameter of stent/stenosis as well as viscosity of blood. The diameter in the resistance equation (**(2**) has a power of 4th, meaning that small changes in diameter significantly change the resistance and the pressure drops/FPR value.

$$\Delta P = QR \tag{1}$$

$$R = \frac{128\ \mu L}{\pi\ (ID^4)} \tag{2}$$

Where:
ΔP = Pressure drops across a stenosis/Balloon-mesh device
Q = Flow rate
R = Resistance

μ = Viscosity of blood
ID = Inner diameter of stenosis/stent.

Computational Fluid Dynamics

We designed idealized stenosis models with a length of 170mm and a diameter of 4mm, having one inlet and one outlet as well as different levels of stenosis severity. The stenosis severity was represented by the ratio of the narrowing diameter of stenosis to the vessel's inner diameter, ranging from level 1.0 represents a fully deployed stent with no mesh pores across the vessel diameter and level 0.25 represents extensive mesh area (i.e., <50μm pores across 4mm ID vessel). This resulted in a total of five models, including one upper and one lower limit with stenosis/vessel ID ratios of 0.75 and 0.25, respectively. Additionally, we included three models with stenosis/vessel ID ratios of 0.56, 0.40, and 0.32 (**Figure 12**).

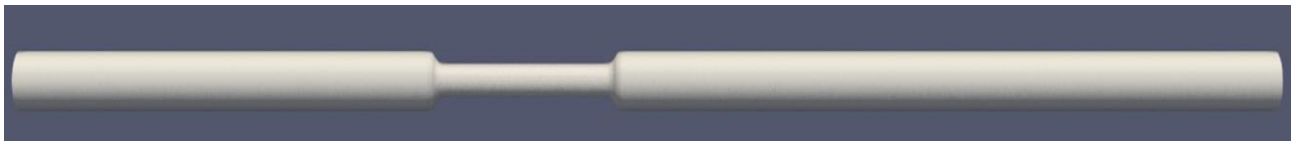

Figure 12: A CAD version of idealized stenosis model with the stenosis/vessel ratio of 0.56.

Using SimVascular software, we created volumetric computational meshes of unstructured tetrahedral elements. The use of an unstructured mesh can provide greater flexibility in

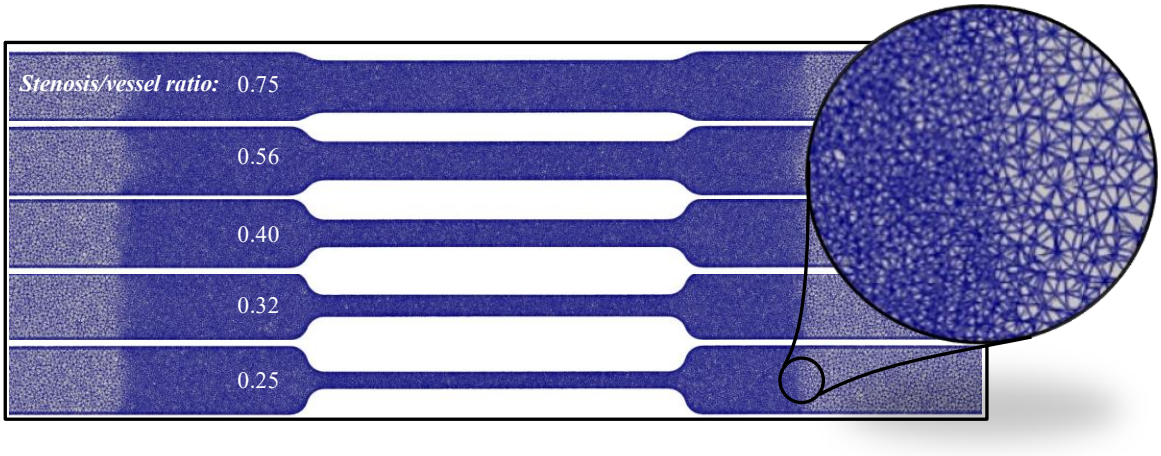

Figure 13: Longitudinal cross-section of mesh elements in the idealized model with more mesh elements in the stenosis section. From top to bottom: Stenosis(stent) ID/vessel ID = 0.75, 0.56, 0.40, 0.32, and 0.25.

concentrating mesh density on the geometry, allowing for finer resolution near the stenosis section and coarser meshing in other regions. 3.8 – 5 M mesh was created for models with more mesh elements focused on the stenosis section (**Figure 13**) and four boundary layers to improve the near-wall resolution of pressure, velocity, and shear calculations (**Figure 14**). We used SimVascular's incompressible Navier-Stokes equations to model blood flow under three pulsatile flow rates, based on neurovascular flow data, simulating both autoregulation and constant resistance models.[83,84] To run the SimVascular svSolver, we utilized a high-performance cluster (HPC – NAU's Monsoon). Postprocessing of the simulation results was performed using ParaView software.

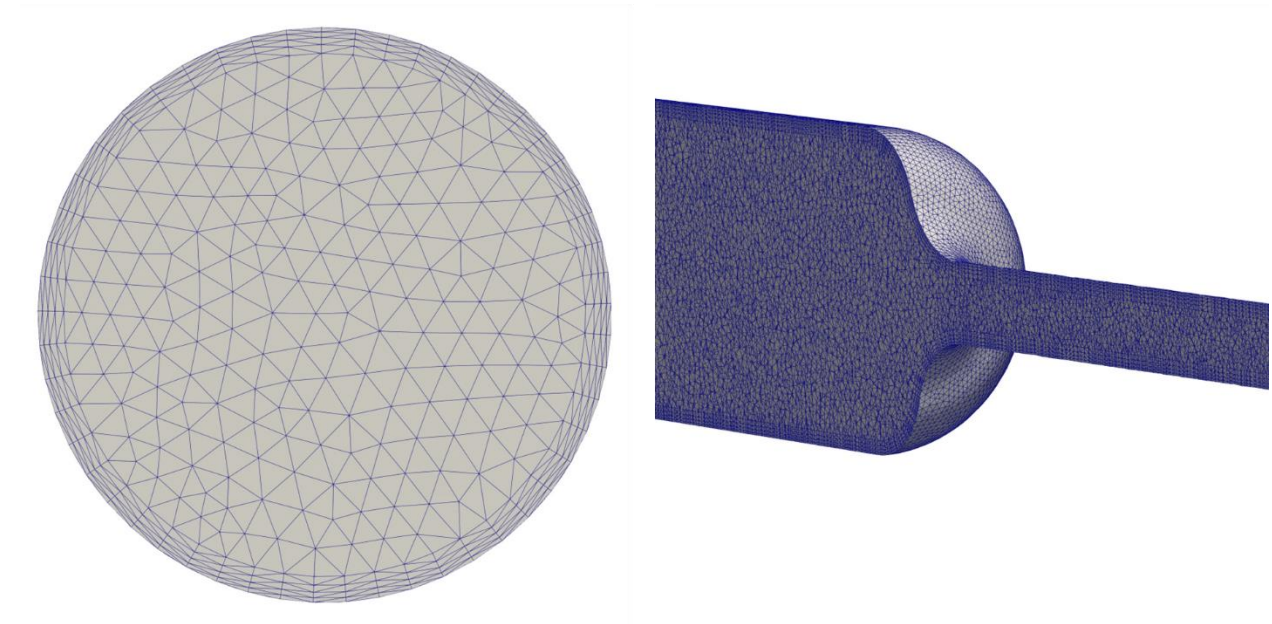

Figure 14: Left: Cross section, right: longitudinal cross-section of the model. Both sections display the utilization of four boundary layers to improve the data resolution near the walls.

Bench-top system

The benchtop setup is comprised of three fundamental segments: 3D-printed models characterized by physiologically and mechanically relevant properties, a pump system replicating

physiological flows, and a blood analogue formulated to match blood viscosity and blood shear-thinning behavior.

3D-printed models: In our study, we utilized the advanced capabilities of the Stratasys Object260 Connex3 3D printer to create vessel models with high accuracy (30 μm) enabling us to achieve the precise dimensions required to create anatomically correct vessel models. To produce the models, we used a combination of elastic UV-cured polymers called VeroClear and Agilus 30, or VC-A30. In order to ensure the models had the necessary physiological properties, our team conducted a thorough mechanical characterization study on the VC-A30 material.[85] Our results confirmed that 3D-printed models using VC-A30 displayed mechanical properties similar to human vessels. The rheometer friction and radial force results are shown in **Figure 15**.

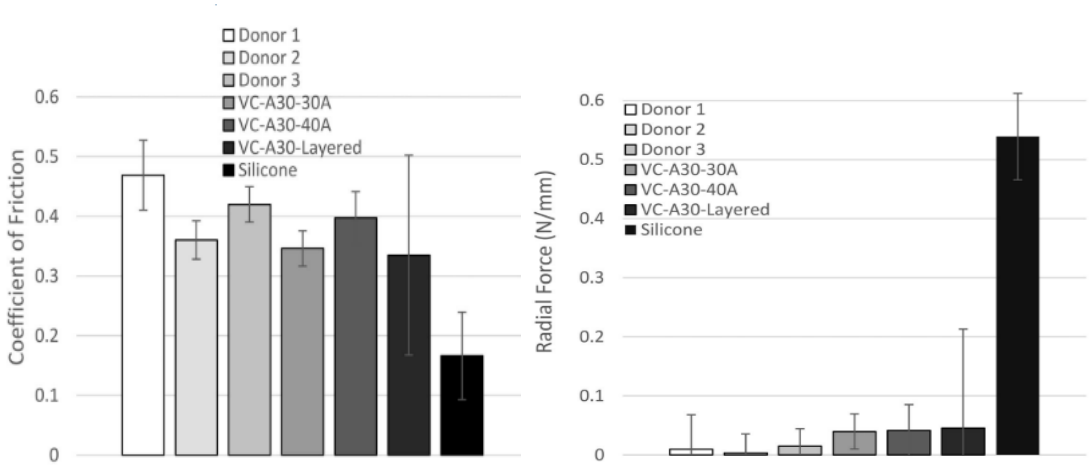

Figure 15: Coefficient of friction (left) and radial force flat plat (right) tests of human vessels, VC-A 30, and silicone samples.[85]

VC-A30 was superior to more traditional modeling materials like glass and silicone, which are frequently used for device testing and surgical training.[85] With the printing process complete, we had a total of eight stenosis vessel models, including the 5 levels of CFD vessel models (**Figure 16**). The 3D-print models were connected to Deltran© pressure transducers (proximal and distal

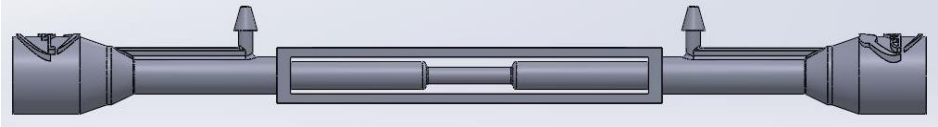

Figure 16: CAD idealized stenosis model for *in vitro* pressure measurement.

to each vessel branch) to obtain the flow and pressure data from various levels of stent ID/vessel IDs.

Pump system: Physiological neurovascular flows were simulated by a digitally controlled, programmable hydraulic pulsatile pump system (SuperPump AR, ViVitro Labs) developed by the BDL team. Blood flow can exit the programmable pump, enter 3D-printed vessels, and return to the pump. Real-time pressure data acquisition is used to validate the model function. (DAQ - **Figure 17**).

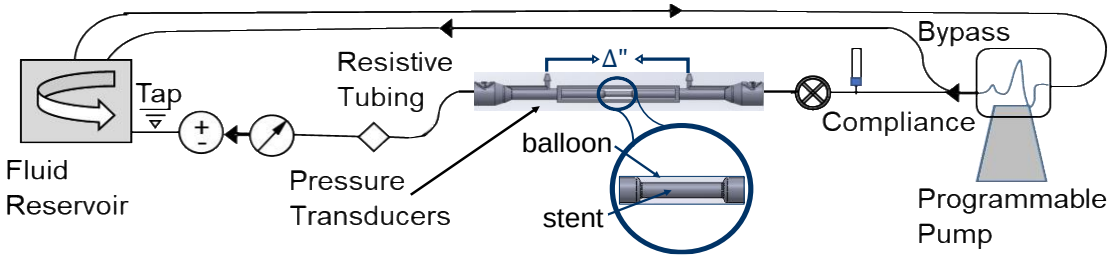

Figure 17: ViVitro Superpump connected to a blood vessel model with real-time pressure and flowrate data acquisition (DAQ).

Human Blood analog: Heparinized blood, being a biohazard with considerable handling constraints and limited shelf life, was not used in the model. Instead, the flow system uses a novel and stable polymer fluid developed by the research team (patent disclosure NAU-2020-24). The viscosity of water, which is typically utilized in surgical training models, is 3-6 times lower than that of blood. As shown in **(2**, viscosity (μ) is inversely proportional to blood flow pressure. The

viscosity of blood also decreases as the shear rate increases (shear-thinning). Utilizing a solution comprising 1 wt% Hydroxypropyl methylcellulose (HPMC) polymer, the flow model exhibits the capability to precisely predict physiological FPR and device performance.

We examined three different physiologically pulsatile flows (Q = 100, 150, and 200 mL/min) in order to analyze the different flow rates in the brain's vessels for both CFD and benchtop testing. We also established two resistance conditions for each flow set - constant

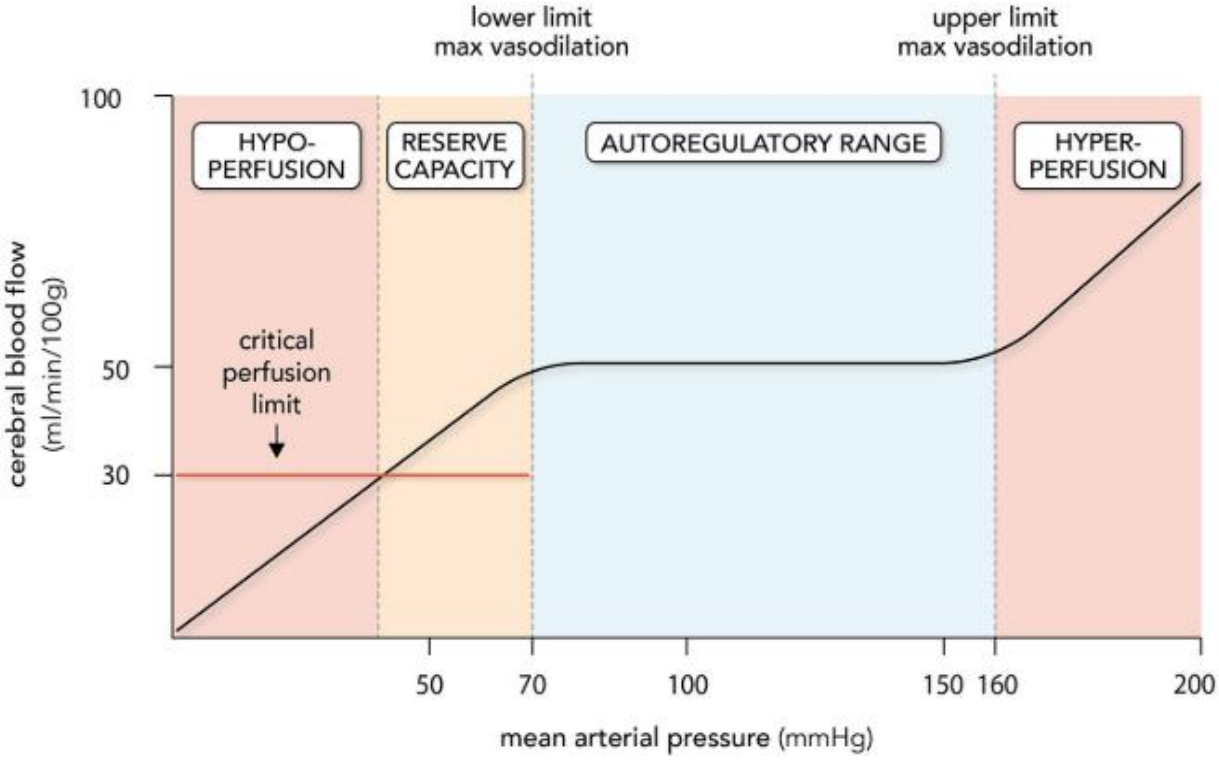

Figure 18: Cerebral autoregulation.[86]

resistance and non-constant resistance (autoregulation). The non-constant condition was created to mimic cerebrovascular autoregulation, which maintains a steady cerebral flow rate across a wide range of cerebral perfusion pressure (70-160mmHg - **Figure 18**).[86]

Results

In this study, we employed a three-part approach to comprehensively assess the hemodynamics of blood. Through theoretical estimation, CFD modeling, and utilization of an advanced bench-top system, we explored the complex dynamics of blood flow within stenosed vessels. These various methods allowed us to understand the pressure-drop phenomena, flow characteristics, and device performance, revealing the complex interaction between vessel geometry, blood viscosity, and resistance. In this section, we present the outcomes, explaining the findings from each methodology and collectively to a comprehensive understanding of hemodynamic behavior under varying conditions of balloon-mesh designs and blood flow rates. Mesh ID can be determined from mesh pore size by calculating the reduction in parent vessel cross sectional area due to the mesh wire area versus pore-size area.

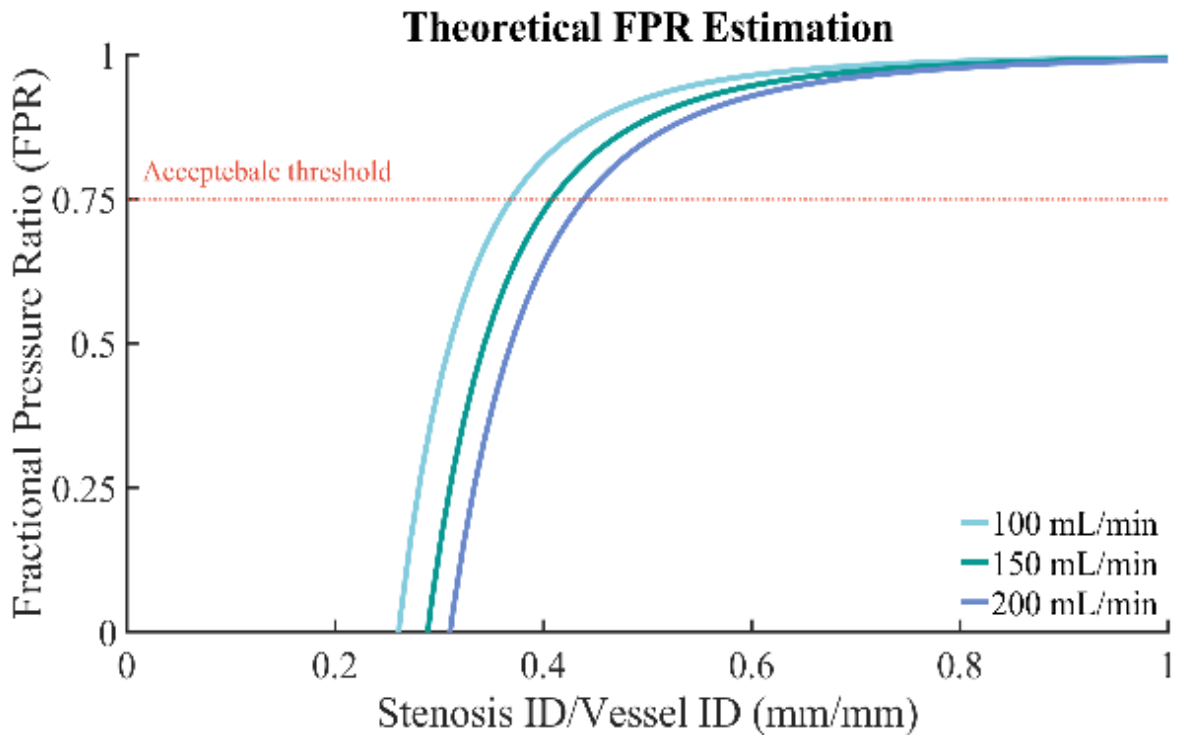

Figure 19: Theoretical estimation of Fractional Pressure Ratio for three flow rates (Q= 100, 150, and 200 mL/min).

Figure 19 illustrates the theoretical estimations of the Fractional Pressure Ratio (FPR) calculated using **Equation 1** for three flow rates: Q = 100, 150, and 200 mL/min. As shown in the figure, higher flow rates are associated with a higher risk of ischemia, assuming an identical ratio of stenosis severity or stent diameter. Notably, a sudden decrease in pressures occurs for stenoses with a severity rate of 50% or higher. In the evaluation of ischemic risk associated with a stenosis, an FPR value of 0.75 serves as a crucial threshold and any FPR value below 0.75 is considered an indication of an ischemic risk.

The CFD and bench-top results for both constant resistance and autoregulation conditions are presented in **Figure 20**. Under the constant resistance condition in the CFD results (**Figure 20-A**), an FPR of 0.75 is observed at stenosis to vessel ratios of 0.27, 0.30, and 0.31 for flow rates of 100, 150, and 200 mL/min, respectively. However, under autoregulated conditions, an FPR of 0.75 is observed at stenosis to vessel ratios of 0.32, 0.37, and 0.42 for the same range of flow rates

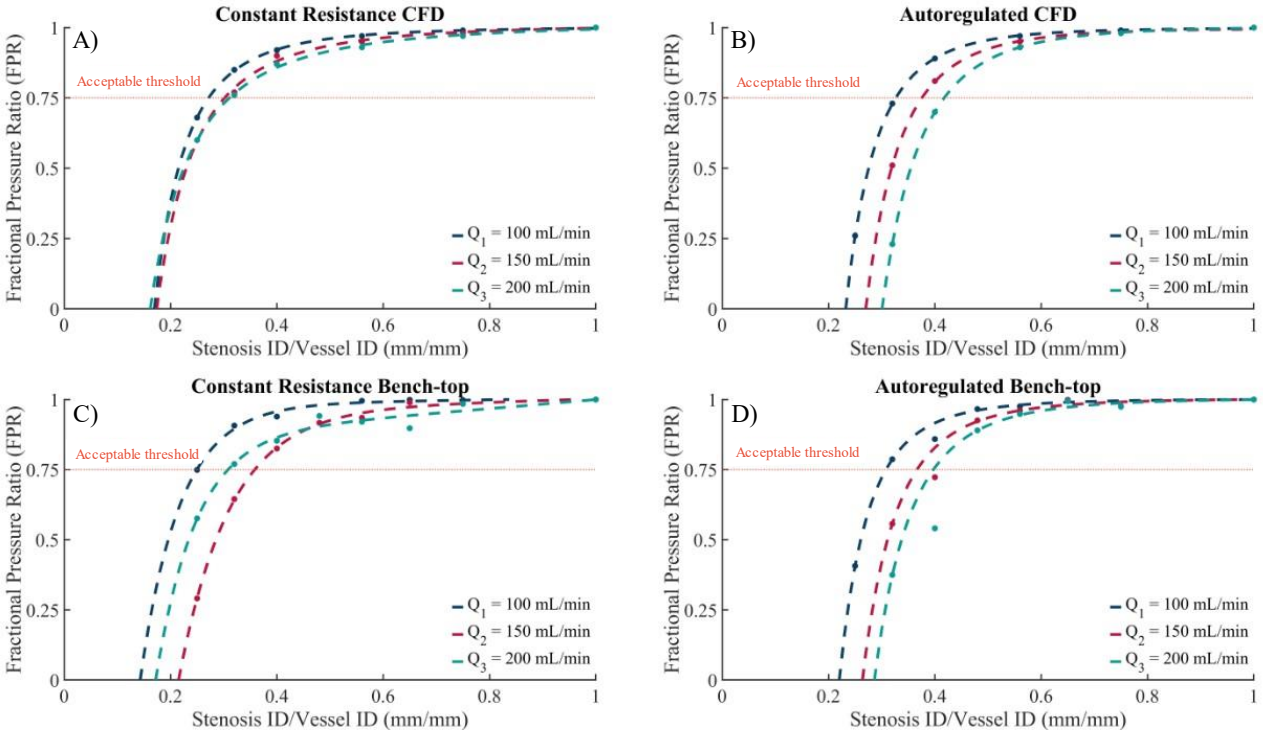

Figure 20: CFD and bench-top results of Fractional Pressure Ratio under constant resistance and autoregulation conditions for three flow rates (Q= 100, 150, and 200 mL/min).

(**Figure 20-B**). Bench-top testing were performed under the same conditions, and the results are shown in **Figure 20-C, D.** For the constant resistance condition, an FPR of 0.75 is observed at stenosis to vessel ratios of 0.25, 0.36, and 0.31 for the flow rates of 100, 150, and 200 mL/min, respectively (**Figure 20-C**). On the other hand, autoregulated FPR of 0.75 is observed at stenosis to vessel ratios of 0.31, 0.37, and 0.40 for the same range of flow rates (**Figure 20-D**). **Figure 21**

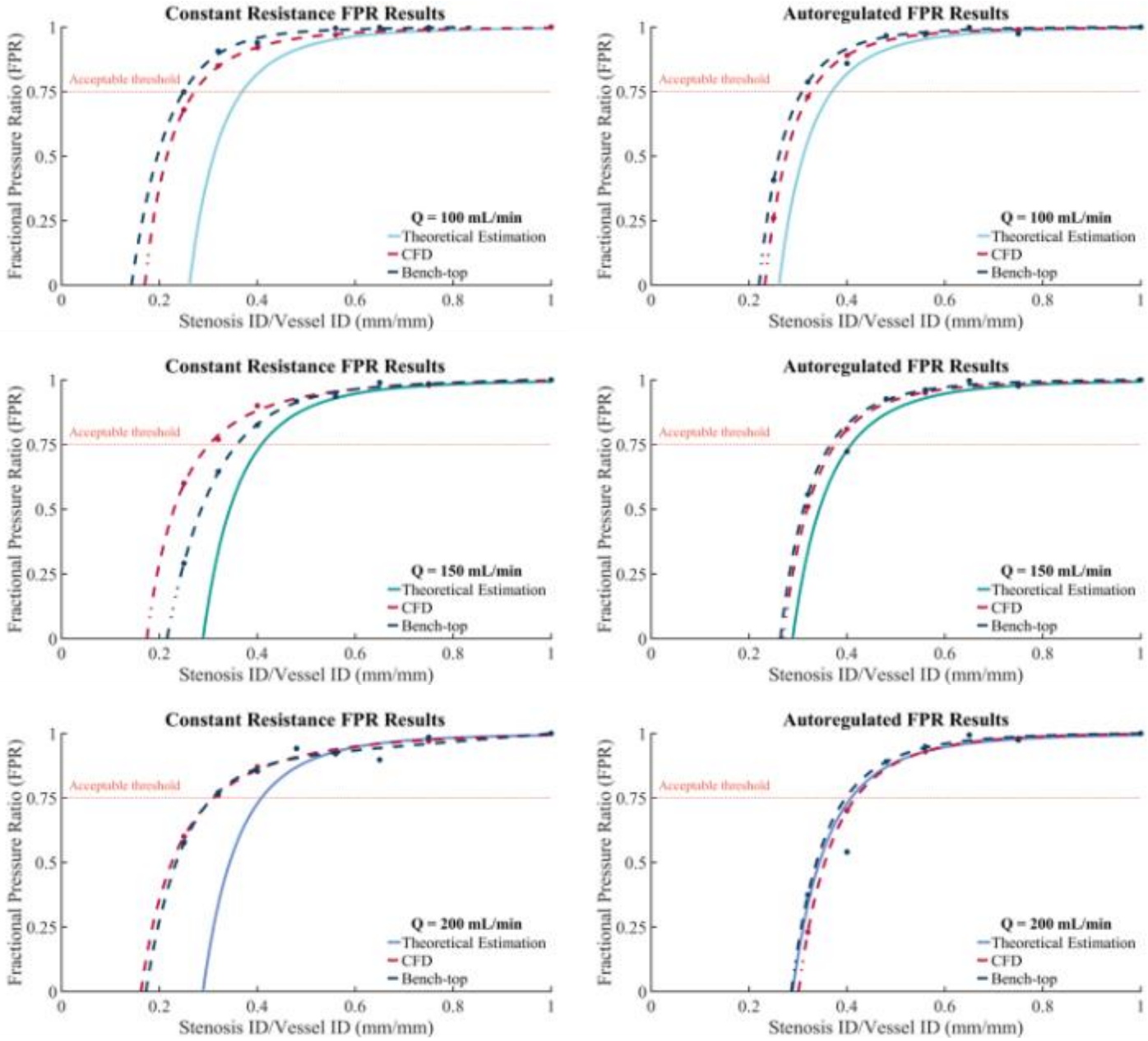

Figure 21: Theoretical estimation, CFD, and bench-top results of Fractional Pressure Ratio under constant resistance and autoregulation conditions for three flow rates (Q= 100, 150, and 200 mL/min).

displays the FPR results obtained from both CFD simulations and bench-top modeling, illustrating their correlation with the theory estimations.

Table 1 shows an analysis of percent differences, comparing theoretical estimation, CFD, and benchtop testing at an FPR of 0.75. The autoregulation method showed a comparatively lower difference among the different methods. When comparing CFD and benchtop results under constant resistance condition with theoretical estimates, a significant difference (> 25%) became evident. In contrast, these difference percentages decrease to less than 15% in the autoregulation condition, implying a closer match between Hagen-Poiseuille's Equation (Equation 1) and the autoregulation condition. Additionally, when comparing benchtop and CFD results, the percentage differences between datasets are below 10%, indicating that the benchtop reproduces CFD data in both constant and autoregulation scenarios. An exception happened with a flow rate of 150 mL/min (% difference = 20%), potentially due to an error in the benchtop's data recording process. This difference could be due to a temporary blockage of the model caused by residual printing material or other particles, leading to an added disruption in flow.

Table 1: Percent difference analysis for FPR of 0.75 between theory estimation, CFD, and benchtop results.

Flow rate	*Constant Resistance*			*Autoregulation*		
mL/min	*CFD vs Theory*	*Bench vs Theory*	*Bench vs CFD*	*CFD vs Theory*	*Bench vs Theory*	*Bench vs CFD*
100	-25.0%	-30.6%	-7.4%	-11.1%	-13.9%	-3.1%
150	-25.0%	-10.0%	20.0%	-6.3%	-7.5%	-1.3%
200	-26.7%	-27.9%	-1.6%	-2.3%	-7.0%	-4.8%

Discussion

The outcomes show valuable insights into the relationship between flow rates, stenosis severity, and ischemic risk, as assessed by FPR. The results of theoretical estimations, CFD simulations, and bench-top testing are discussed to provide a comprehensive understanding of the evaluation of FPR and the associated ischemic risk. Additionally, we will address the study's limitations and suggest potential areas for future research and clinical applications.

Theoretical estimation, using the Hagen-Poiseuille flow equation, is a basic method for understanding the pressure drop and flow reduction caused by narrowing of blood vessels in the brain. The results show that even a small decrease in the inner diameter of the narrowing can have a significant impact on both pressure drops and flow rates. The theoretical estimations, as shown in **Figure 19**, indicate that higher flow rates are linked to an increased risk of ischemia when stenosis severity remains constant. The sudden decrease in pressures observed for stenoses with a severity rate of 50% or higher is noteworthy. Furthermore, an FPR value of 0.75 serves as a crucial threshold for evaluating the ischemic risk associated with stenosis, with FPR values below 0.75 indicating ischemic risk. The theoretical FPR endpoint indicates that, in order to maintain sufficient blood flow and reduce the risk of ischemia, the narrowing should not exceed 37%, 41%, and 44% of the vessel size for flow rates of 100, 150, and 200 mL/min, respectively. The analysis of percent differences between theoretical estimation, CFD, and benchtop testing at an FPR of 0.75 shows that the autoregulation method exhibits a lower difference compared to other methods. Under constant resistance conditions, both CFD and benchtop methods deviate significantly (> 25%) from theoretical estimates. However, introducing autoregulation reduces these differences to less than 15%, indicating better agreement with theoretical estimation. These findings highlight the importance of considering the severity of narrowing when evaluating its impact on brain

function and the need for appropriate treatment. While theoretical estimation is an initial step in assessing blood flow, further validation through experiments or computer simulations is necessary.

CFD modeling provides a detailed understanding of blood flow in idealized stenosis, allowing for simulations of different types of pulsatile flows and levels of narrowing severity. The results show that CFD simulations accurately capture flow patterns and pressure differences across the stenosis. These findings align with previous studies by Perina-jová et al., who used CFD to study turbulence, wall shear stress, and blood flow in aortic and cerebral arteries, respectively.[77] However, it is important to note that computational models, including idealized stenosis, may not fully represent the complex physiological environment of actual cerebral blood vessels.

A comparison of the autoregulated results obtained from CFD simulations and bench-top testing shows a strong agreement between the two (% difference < %10). This indicates that both experimental setups accurately collect both constant resistance and autoregulation mechanisms, confirming their reliability in replicating physiological conditions. Furthermore, the close agreement between autoregulated CFD simulations and bench-top results highlights their effectiveness in accurately capturing physiological conditions. These findings significantly contribute to our understanding of the factors influencing the ischemic risk associated with stenosis.

Conclusion

In conclusion, this research aimed to design and model a novel balloon-mesh prototype for endovascular treatment of aneurysms. The study utilized theoretical estimation, computational fluid dynamics (CFD) simulations, and an advanced bench-top system to comprehensively assess the hemodynamics of blood flow in neurovascular vessels. The Fractional Pressure Ratio (FPR) was employed as a crucial parameter for evaluating the ischemic risk associated with device placement in brain vessels. Theoretical estimation highlighted the impact of flow rates and stenosis severity on ischemic risk. CFD simulations accurately captured flow patterns and pressure differences, while bench-top testing replicated physiological conditions, revealing a strong agreement between the two methods. The agreement between theoretical estimation, CFD simulations, and bench-top measurements established a reliable foundation for understanding the complex relationship between vessel geometry, blood viscosity, and resistance. However, the study's limitation of using simplified models emphasizes the need for future research with more realistic and patient-specific models. Overall, this research contributes valuable insights into optimizing device design and evaluating ischemic risk, advancing the field of endovascular treatment for aneurysms and neurovascular diseases.

CHAPTER 3 – AIM II – Prototype Development and Mechanical Integrity

Aim of Research

Develop a balloon-mesh prototype and test the prototypes for mechanical integrity to assess its structural strength and performance.

Hypothesis: *We hypothesize that the balloon-mesh prototypes exhibit sufficient mechanical integrity, demonstrating structural strength and performance during testing, indicating that they are suitable for practical applications.*

Introduction

Introduction of a balloon-mesh device

Through our collaborations with medical companies, we have determined that the technology required to create a device combining balloon and stent devices is not yet fully practical for device manufacture. Furthermore, the proposed balloon and stent device would complicate the treatment process for neurointerventionalists. Considering the urgency and short-time window associated with treating cerebral aneurysms, the simultaneous control of two devices - a balloon and a stent - in conjunction with embolic devices could complicate the aneurysm treatment process. These complications might result in less desirable outcomes. Moreover, neurointerventional must ensure accurate placement of both the balloon and stent across the aneurysm neck using fluoroscopy, which requires additional training. To address these concerns and ensure the feasibility of the design for medical companies, we have proceeded with the development an alternative design, utilizing a fine mesh structure with a conformable “balloon” shape. Under seed grant funding from the Arizona Flinn Foundation, initial prototypes have been developed in cooperation with Pivot Medical (Minneapolis, MN). Detailed illustrations of initial prototypes can

be found in **Appendix A - Figure 59**. The designs are optimized to maximize FPR, minimize intra-aneurysmal flow velocities, and minimize turbulent effects throughout.

A balloon-mesh device is being developed to test the hypothesis: a device that can temporarily provide aneurysm neck protection during complementary device deployment, while maintaining blood flow in the parent artery, would maximize device placement in the aneurysm

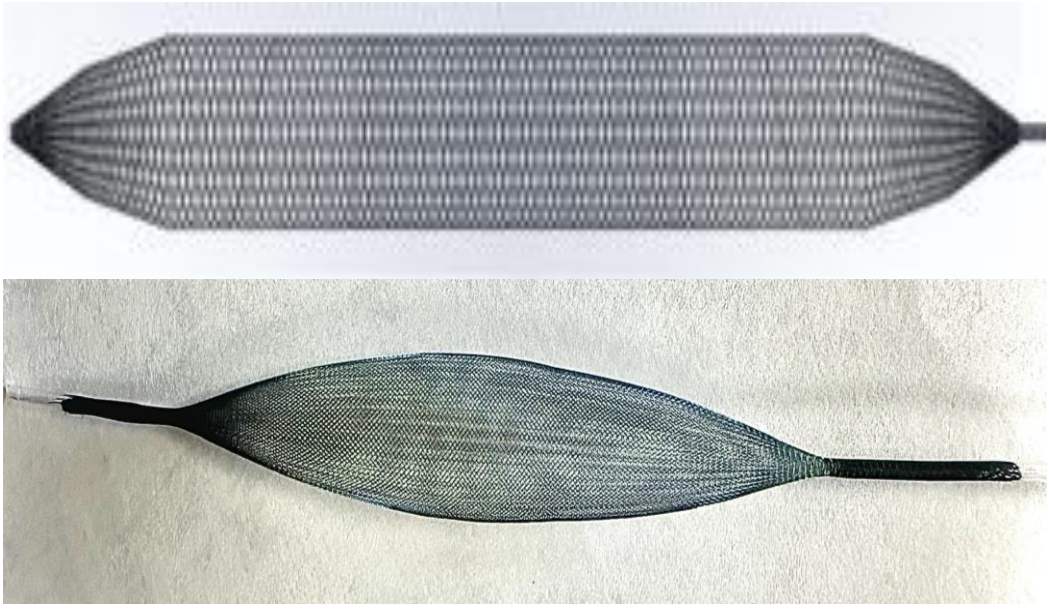

Figure 22: Balloon-mesh device – Top: braided fine mesh with a conformable "balloon" shape. Bottom: initial balloon-shaped mesh prototype

sac, provide a smooth surface at the neck to promote maximal neointimal vessel healing, prevent device migration into the parent artery in the short-term, and reduce aneurysm recanalization rates in the long-term (**Figure 22**).

Material properties: The initial balloon-mesh device consists of 144 nitinol braided wires, each with a diameter of 20 nm. It is designed to be both retrievable and self-expandable forming a mesh with a balloon-like shape. The mesh has a pore-size of 200 μm (**Figure 24**) and maximum diameter up to 6 mm. The mesh is connected to a microwire/push wire and can be delivered and retrieved from various 4-5F microcatheters. To determine the porosity of the device, we conducted a series

of tests involving the injection of a liquid embolic material – NeuroCURE – through mesh strainers of varying sizes, ranging from 20 μm to 1000 μm. NeuroCURE was selected as the worst-case scenario device with highest potential migration risk. Among the three trials conducted using mesh strainers of sizes 500 μm, 750 μm, and 1000 μm, diffusion of NeuroCURE was observed only in one case of the 750 μm mesh strainer (**Figure 23**). Therefore, we selected a maximum mesh size of 500 μm for the balloon-mesh device. In addition, the use of smaller sizes (i.e., 20 μm) increases flow disruption (increasing resistance – **Equation 1**) and has the potential to result in a pressure drop exceeding 25% across the device. As a results, we chose an initial mesh size of 200 μm for the purposes of mechanical and pressure investigations. The balloon-mesh device with a 200 μm mesh size, distributes applied forces across the vessel wall, minimizing the likelihood of vessel trauma.

Figure 23: Mesh strainer (750 μm) used for NeuroCURE diffusion tests.

For a final marketable-version of the device, future dimensions will be downscaled to fit within in a 2-3 Fr catheter, with a maximum diameter ranging from 2-5 mm. Blood flow in the parent artery is maintained through the proximal and distal mesh and the fine mesh design provides

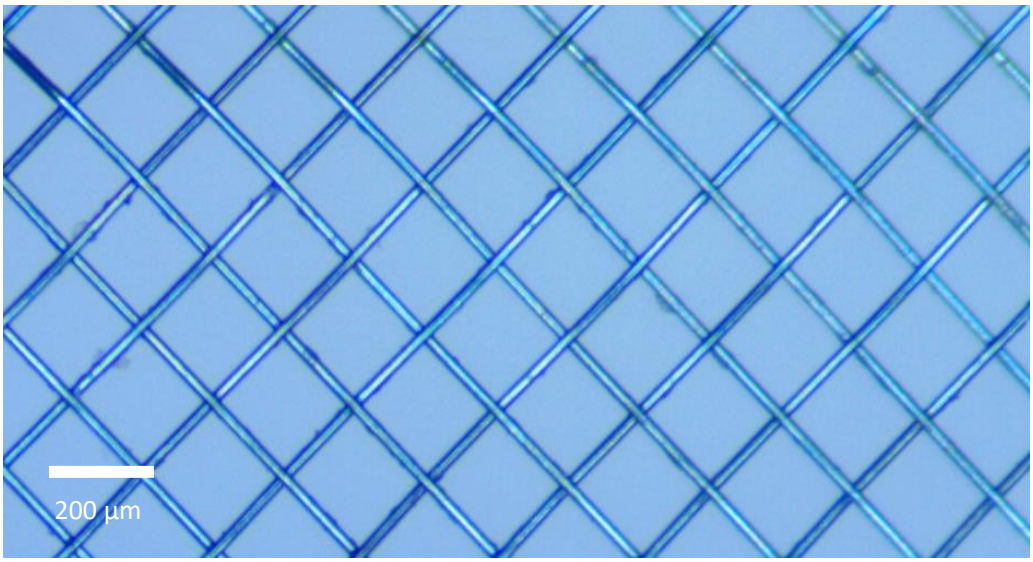

Figure 24: Mesh structure of the balloon-mesh device (200 µm).

a smooth and consistent balloon-shaped support across the aneurysm neck and parent vessel wall. Safer embolic delivery: A microcatheter is placed in the aneurysm sac for device delivery (i.e., SL-10® for coil, liquid embolic, or flow disruptor placement). The adjunctive device (balloon-mesh catheter) is placed in the parent artery across the aneurysm neck. The balloon-mesh is delivered from the microcatheter tip via an attached push wire/retriever (microwire). As the balloon-mesh

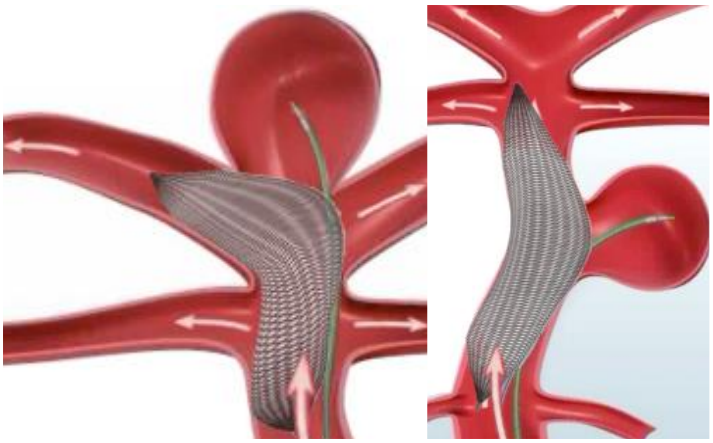

Figure 25: Balloon-mesh conforming to the aneurysm neck and jailing a delivery microcatheter (green) for (**Left**) bifurcation and (**Right**) sidewall aneurysm treatment, while maintaining parent artery blood flow.

expands form the microcatheter tip, the microcatheter is retracted and the balloon-mesh expands across the aneurysm neck. The balloon-mesh, which is a highly elastic alternative to traditional flow diverters and stents, can easily conform to various aneurysm neck morphologies to provide aneurysm neck protection and jailing of the delivery microcatheter. The preferred embolic device is then delivered inside the aneurysm sac from the delivery microcatheter. The fine mesh structure of the balloon-mesh provides a continuous and smooth surface at the aneurysm neck to contain device delivery, minimize aneurysm sac inflow and outflow, minimize downstream migration risk, and maintain continuous parent artery blood flow. After deployment of the balloon-mesh, there will be adequate blood flow in the parent artery (verified by FPR). Once the aneurysm is treated, the jailed microcatheter is removed, and the balloon-mesh is retrieved into the microcatheter tip. The balloon-mesh device is intended for 3-5 mm diameter parent vessels and for sidewall aneurysms (**Figure 25**-Right). Additionally, ultra-compliant mesh options are under investigation that will form to open volume shapes, such as expanding across the neck of a bifurcation aneurysm (similar coverage as a current Scepter-XC/Hyperform balloon), while maintaining parent artery flow in all primary vessel branches (**Figure 25**-Left).

In the preliminary stage of developing the balloon-mesh device, we created three prototypes, all featuring a woven nitional mesh structure with a mesh size of 200 μm (**Figure 26**). These prototypes were made using the resources at Pivot Medical. The prototypes were attached to a push wire to control the delivery, tracking, and retraction of the device. Within this phase, we experimented with different shapes and length of the device to assess the efficacy of both the closed

Figure 26: Three balloon-mesh prototypes with the different shapes. Balloon mesh 1 with a close distal end. Balloon-mesh 2 and 3 with the open end and different length.

In the following sections, we will discuss the development and mechanical integrity testing of the balloon-mesh prototypes in detail. We will explore the material properties of the device, including size, design, radial force, and tracking force. Furthermore, we will explore potential approaches to enhance the performance of these prototypes. Through these discussions, we aim to validate our

hypothesis that the balloon-mesh prototypes exhibit sufficient mechanical integrity, making them suitable for practical applications in the treatment of cerebral aneurysms.

Methods

This section presents the methodology employed for assessing the mechanical integrity of the balloon-mesh prototypes. The primary objective of these tests was to evaluate the mechanical properties of the prototypes and compare them to an FDA-approved medical devices, serving as the control. To accomplish this, we utilized well-established mechanical testing designs at BDL. In addition, various data collection and analysis procedures were utilized to obtain accurate and reliable results.

The study design employed in this research focused on mechanical testing, specifically radial force and tracking force studies. These studies were conducted to investigate the mechanical performance of balloon-mesh prototypes and compare them with control devices. To collect the necessary data, we utilized the BDL's HR-2 hybrid rheometer (TA Instruments, New Castle, DE), an advanced instrument for measuring and analyzing the rheological and mechanical properties of materials. The study involved three balloon-mesh prototypes and two commercially-available control devices: a Pipeline™ Flex embolization device (PED, Covidien/Medtronic), and a Low-Profile Visualized Intraluminal Support Junior stent (LVIS Jr., MicroVention). Detailed information regarding the size of these devices is provided in **Table 2**.

Table 2: Balloon-mesh prototypes and control devices size information.

Devices	***OD (mm)***	***Length (mm)***
Balloon-mesh 1 (BM1)	6.40	48.14
Balloon-mesh 2 (BM2)	6.40	35.09
Balloon-mesh 3 (BM3)	6.40	28.11
PED	4.5	15
LVIS Jr	2.5	20

Radial Force Study

Three balloon-mesh prototypes, one PED, and one LVIS Jr, were subjected to radial force testing. The "radial force flat plate test" method was employed, which involved comparing the forces at 50% compression of the sample's outer diameter (OD) per unit length of the device. To accurately measure force and displacement, a 40 mm mirrored rheometer plate (**Figure 27**) was

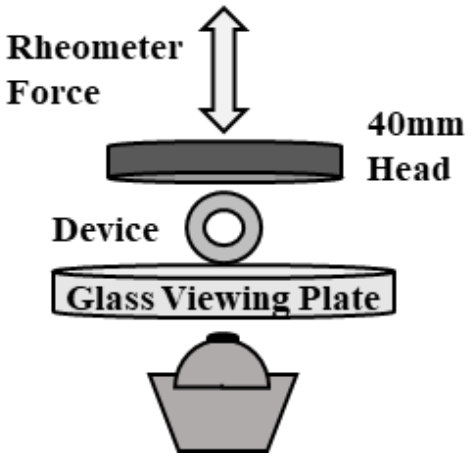

Figure 27: mirror rheometer plate used for radial force testing.

utilized. The plate was carefully lowered onto the prototypes and control devices to record their OD. Force measurements were taken as the devices were compressed by the rheometer at a controlled rate of 2.1 mm/min. The resulting force at 50% compression of the device OD was reported per unit length of the device in N/mm. Each device underwent four radial force measurements (n=4 repeats per device).

Tracking Force Study

This study aims to evaluate the force and energy effects involved in the placement of endovascular catheters into (push) and out of (pull) tortuous neurovascular structures. The delivery microcatheters were positioned at the M1 segment of the middle cerebral artery (MCA) in the BDL's 3D-printed CW model. The balloon-mesh prototypes (n=3) and one control device (PED, n=1) were pushed through the last 8.5 cm of the delivery microcatheter, traversing the cavernous

and ICA terminus segments of the CW model (**Figure 28**). More detailed information regarding the delivery microcatheters used for each device can be found in **Table 3**.

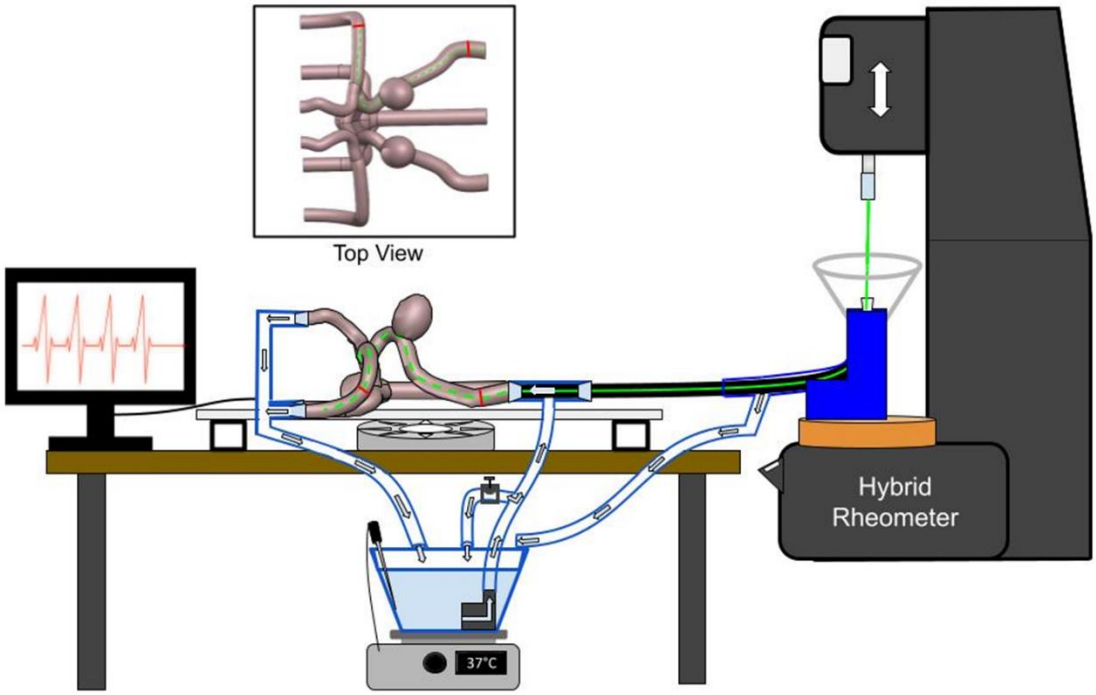

Figure 28: Device tracking. Push and pull friction test with a rheometer force plate.

The experimental procedure involved the following steps for the balloon-mesh prototypes and PED: The devices were carefully fed into the delivery microcatheter and placed in the model. The distal push microwire was connected to a movable rheometer force plate, allowing for controlled movement inside the CW model. To simulate the clinical scenario, the rheometer force plate steadily moved at a constant rate of 0.25 cm/s, while recording the force required push the devices through the tortuous model (from cervical, through cavernous to the ICA terminus and then MCA M1 ~ 8.5 cm). After completing the push test, the rheometer automatically reversed direction and performed the pull test: moving the force plate at the same rate (0.25 cm/s) and same distance (8.5 cm) back to the starting point. The test was repeated (n = 4) per each device and results averaged for statistical comparison (t-test, 95 % confidence) for the following factors:

- ICA straightening in the flexible CW model (n = 4, prototypes = 3, control = 1, total tests = 16)
- complications from the progression technique (n = 4, prototypes = 3, control = 1, total tests = 16)
- Post inspection: kinking (n = 1, prototypes = 3, control = 1, total tests = 4)
- Post inspection: fatigue points (n = 1, prototypes = 3, control = 1, total tests = 4)
- Post inspection: stent, integrity, damage, or delamination

Table 3: Delivery microcatheters and size information. ZOOM (ImperativeCARE™) – Headway (MicroVention™).

DELIVERY MICROCATHETER	Used for delivering	OD (F/mm)	ID (in/mm)
ZOOM 45	Balloon-mesh 1	5/1.52	0.045/1.14
ZOOM 55	Balloon-mesh 2 and 3	5/1.75	0.055/1.4
HEADWAY 27	PED	2.6/0.86	0.027/0.69

Results

This section presents the results of the study, which investigates the mechanical integrity of the balloon-mesh prototypes and compares them with the control devices. The analysis focused on radial force and tracking force to assess the applicability of the prototypes and determine if any modification is necessary. Of particular significance, the analysis uncovered that the balloon-mesh prototypes demonstrated significantly lower radial forces and tracking force compared to the FDA-approved control devices, LVIS Jr and PED. The results section provides a detailed analysis of the radial forces of devices, followed by an examination of tracking force of devices in a CW model.

Radial force study

This study involved three balloon-mesh prototypes and control devices – PED and LVIS Jr (**Table 2**). The dataset consists of experimental measurements of radial force at 50% compression of the device OD per unit length (N/mm). In order to evaluate the relationship between the prototypes and control devices, a set of statistical analyses including f-test, t-tests, and percent differences were performed.

The following **Figure 29**-**Figure 31** illustrate the relationship between radial force per unit length and the gap for balloon-meshes prototypes. The gap corresponds to the OD of the device during testing. When the force exerted on the device is zero, the reading gap matches the OD of the device. As additional force is applied, the device compresses, leading to a decrease in the gap or OD. The radial force of the device is reported when it reaches 50% of its initial gap (initial OD of the device).

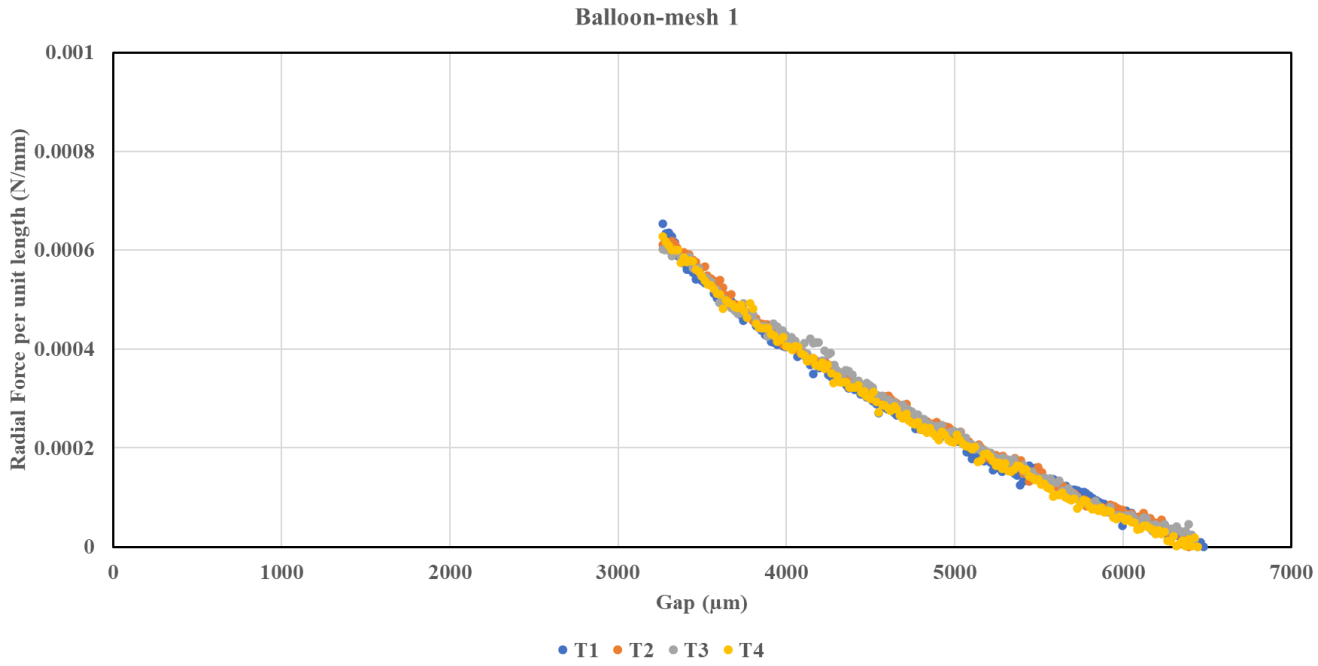

Figure 29: Radial force per unit length with respect to gap (OD of the device) for balloon-mesh 1.

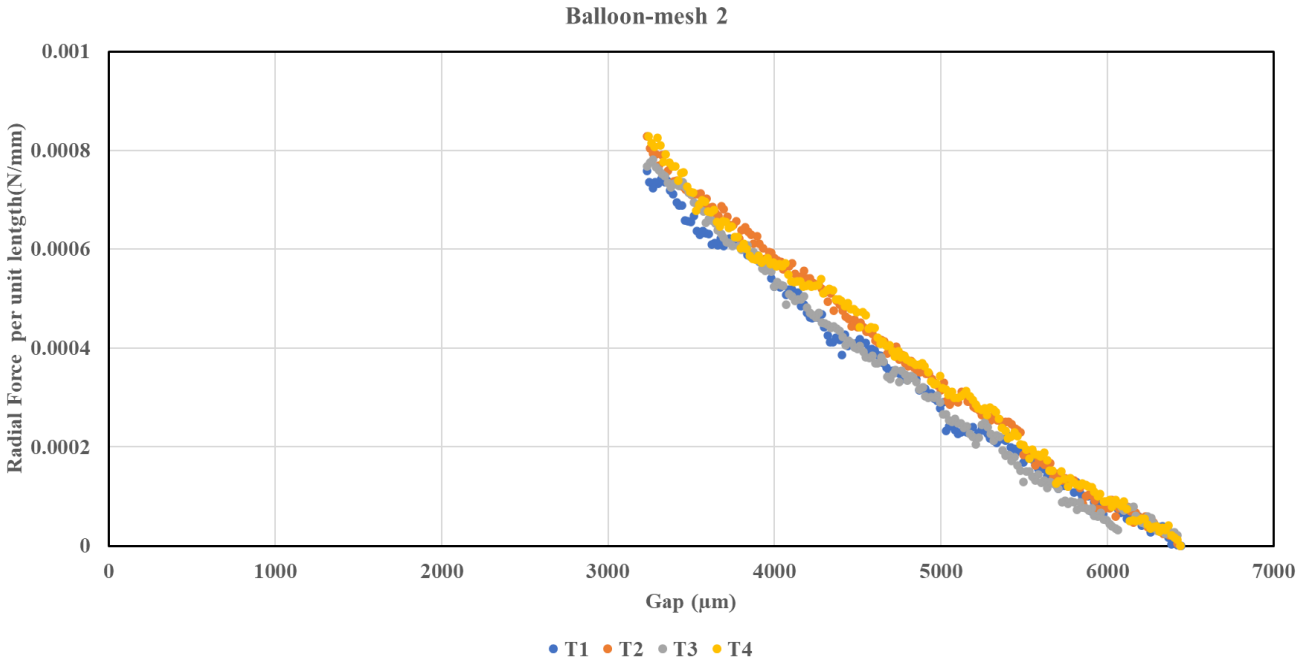

Figure 30: Radial force per unit length with respect to gap (OD of the device) for balloon-mesh 2.

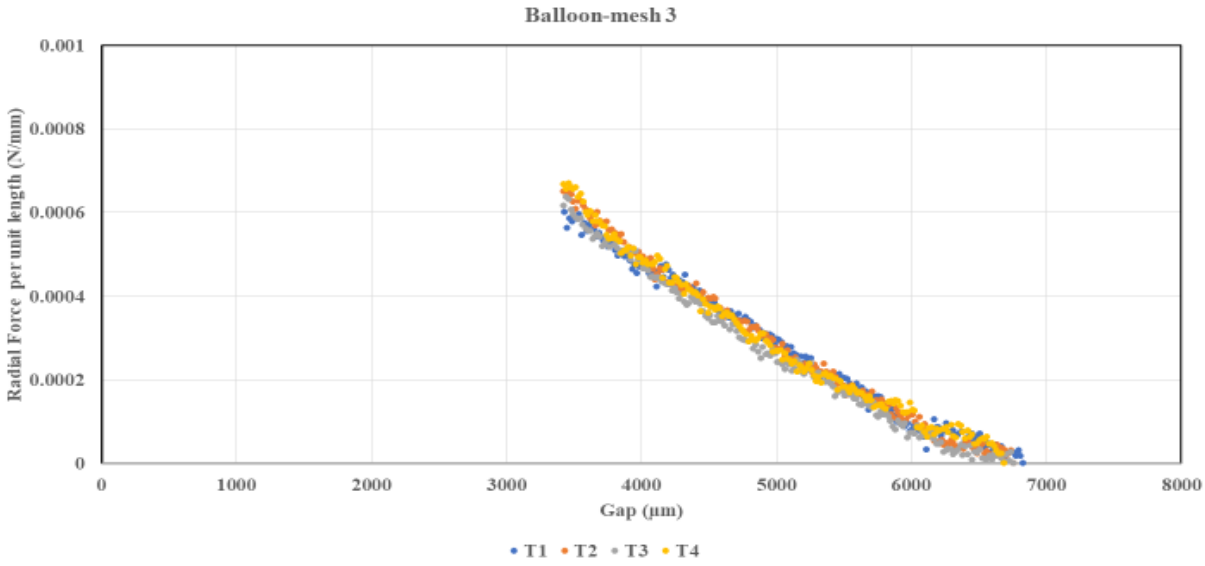

Figure 31: Radial force per unit length with respect to gap (OD of the device) for balloon-mesh 3.

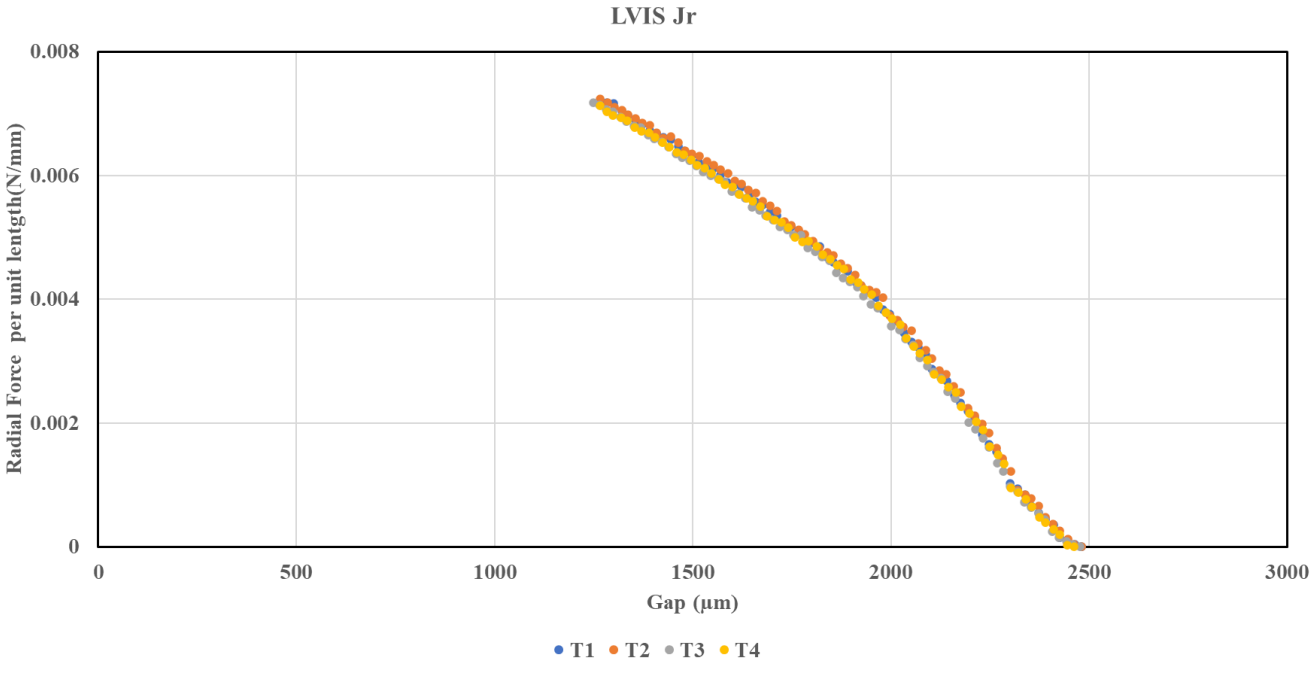

Figure 32: Radial force per unit length with respect to gap (OD of the device) for LVIS Jr.

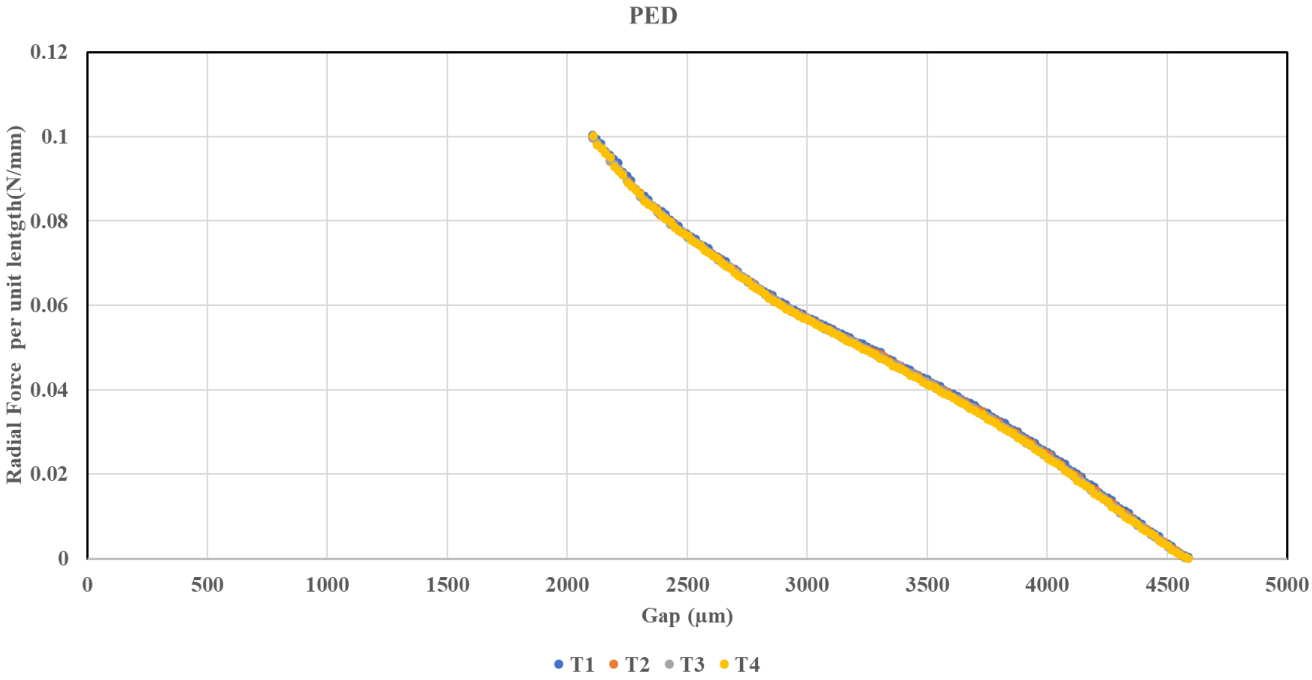

Figure 33: Radial force per unit length with respect to gap (OD of the device) for PED.

Control devices, PED and LVIS Jr, are permanent endovascular stents that can also function as temporary devices if they are not fully deployed in the parent artery. Radial force measurements were conducted for both control devices in fully deployed and half deployed conditions. The **Figure 32**-**Figure 33** depict the radial force measurement results for the fully deployed conditions of the control devices. In addition, the **Appendix A - Radial Force Study** contains the half-expanded plots.

The **Table 4:** Four repetitions of radial force at 50% compression of the devices' OD. reports the radial forces at 50% compression of the devices' OD. Four repetitions were performed for each device to ensure accuracy and obtain reliable measurements. **Error! Reference source not found.** presents a statistical comparison among the devices. The percent difference method, f-test, and t-test were employed for each comparison. For all comparisons except those involving PED, the f-test indicates no significant evidence to reject the null hypotheses ($p > 0.05$), allowing

for the application of the equal variance t-test. However, in comparisons with PED, the null hypotheses of the f-test were rejected, suggesting unequal variances and necessitating the use of non-equal variance t-test.

Table 4: Four repetitions of radial force at 50% compression of the devices' OD.

Device	*T1*	*T2*	*T3*	*T4*	*Ave*	*σ*
BM1	0.00065	0.00061	0.00060	0.00063	0.00062	0.00002
BM2	0.00067	0.00073	0.00068	0.00073	0.00070	0.00003
BM3	0.00057	0.00061	0.00058	0.00063	0.00060	0.00003
LVIS Jr_Half expanded	0.01110	0.01114	0.01104	0.01097	0.01106	0.00008
LVIS Jr	0.00722	0.00724	0.00717	0.00713	0.00719	0.00005
PED_Half expanded	0.09309	0.09214	0.09229	0.09249	0.09250	0.00042
PED	0.08501	0.08424	0.08507	0.08716	0.08537	0.00125

When comparing any devices with LVIS Jr and PED, there is compelling evidence to reject the null hypothesis of the t-test, signifying a significant difference between the devices ($p < 0.05$). Regarding the comparison of the balloon-mesh prototypes, the results indicate no significant evidence to reject the t-test hypothesis when comparing balloon-mesh 1 with balloon-mesh 3 ($p = 0.21$). However, when comparing with balloon-mesh 2, the null hypothesis was rejected ($p_{BM1} = 0.0073$, $p_{BM3} = 0.029$). These results suggest that balloon-mesh 2 shows distinct characteristics or performance when compared to both balloon-mesh 1 and balloon-mesh 3. However, when comparing the percent differences across all balloon-mesh prototypes, the percentage differences remained below 20%, which is an acceptable difference for the initial

Table 5: a statistical comparison of radial force at 50% compression.

Device	**BM1**			**BM2**			**BM3**			**LVIS_Jr**			**PED**		
	% diff	**f.test**	**t.test**	**% diff**	**f.test**	**t.test**	**% diff**	**f.test**	**t.test**	**% diff**	**f.test**	**t.test**	**% diff**	**f.test**	**t.test**
BM1				-11%	0.56	0.0073	4%	0.72	0.2120	-91%	0.23	0.0000	-99%	0.00	0.0000
BM2	13%	0.56	0.0073				18%	0.81	0.0029	-90%	0.52	0.0000	-99%	0.00	0.0000
BM3	-4%	0.72	0.2120	-15%	0.81	0.0029				-92%	0.39	0.0000	-99%	0.00	0.0000
LVIS_Jr	1053%	0.23	0.0000	922%	0.52	0.0000	1102%	0.39	0.0000				-92%	0.00	0.0000
PED	13590%	0.00	0.0000	12033%	0.00	0.0000	14176%	0.00	0.0000	1087%	0.00	0.0000			

iteration of prototyping given the variations in shapes and dimensions among the prototypes. Further analysis and investigation are necessary to understand the specific factors contributing to these differences and their implications for the overall effectiveness and functionality of the prototypes.

Figure 34: Radial force per unit length at 50% compression for all devices.-**Figure 35** present the radial forces for all devices combined in a single graph. **Figure 34:** Radial force per unit length at 50% compression for all devices. specifically displays these values at 50% compression of the devices' outer diameter (OD), while **Figure 35** illustrates the force versus gap relationship for all devices. As evident from the figures, the radial force of LVIS Jr is approximately 10 times greater than that of the balloon-mesh prototypes. Additionally, the radial force of PED surpasses LVIS Jr by approximately 10 times and exceeds the radial force of the balloon-mesh prototypes by approximately 100 times.

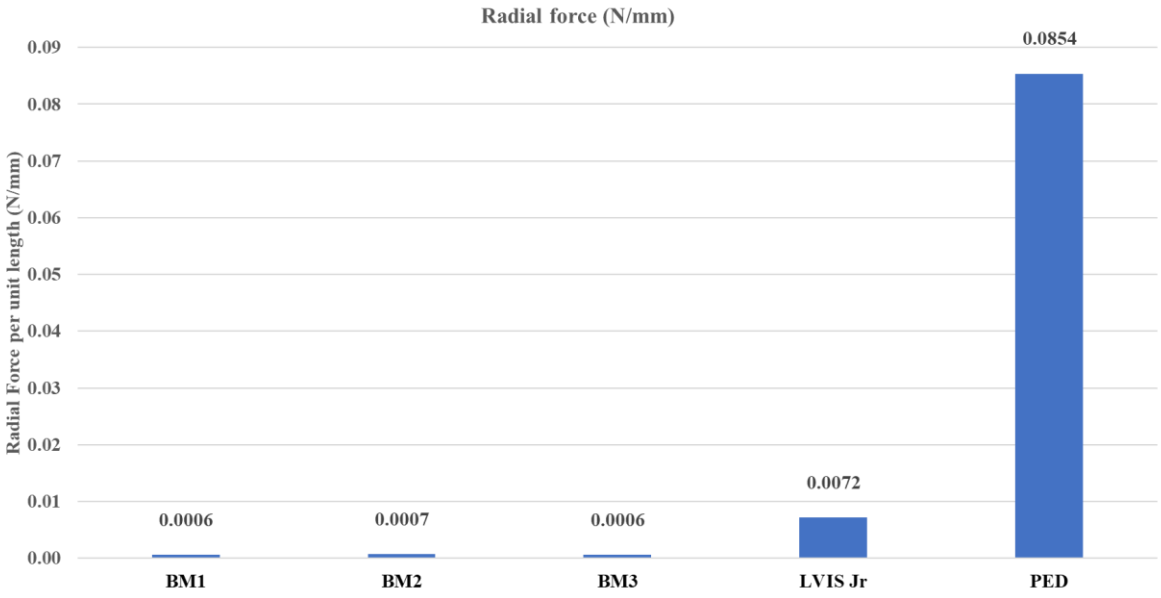

Figure 34: Radial force per unit length at 50% compression for all devices.

Further figures, which include the radial forces for the control devices in a half-expanded condition, as well as the radial forces of only the balloon-mesh prototypes at 50% compression, can be found in the **Appendix - Radial Force Study.**

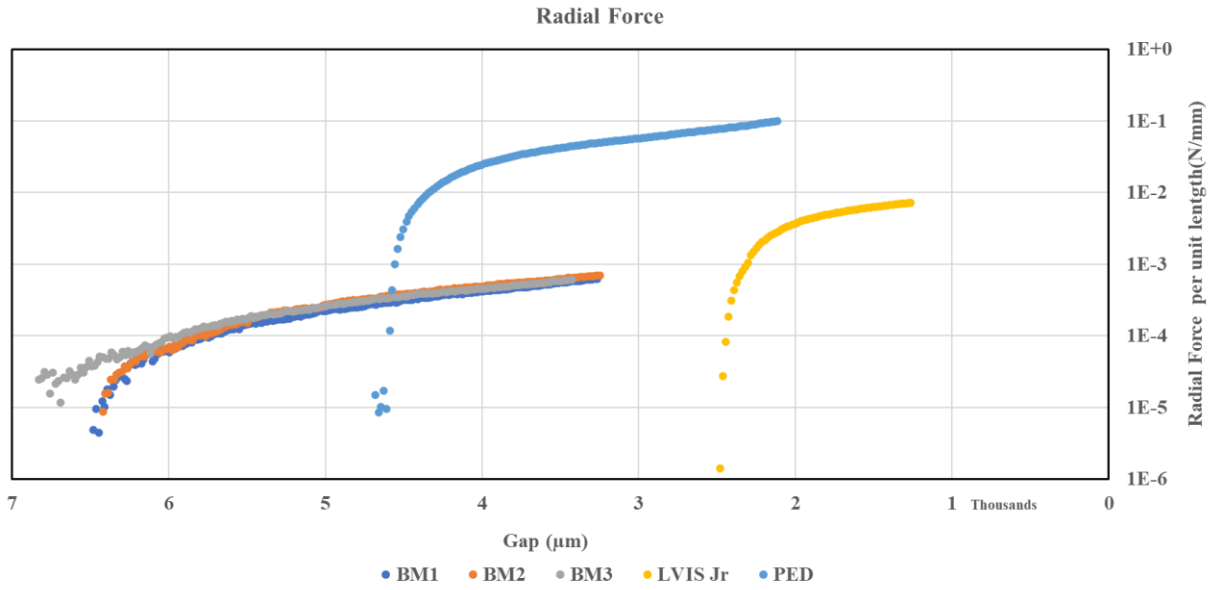

Figure 35: Radial force versus gap relationship for all devices.

Tacking Force Study

This study involved three balloon-mesh prototypes and one control device – PED (**Table 2**). The dataset consists of experimental measurements of tracking force (Push/pull - N) of device in a 3D-printed CW model (**Figure 28**). To assess the relationship between the prototypes and the control device, a series of statistical analyses, including f-test, t-tests, and percent differences were performed. We used the PED device as a control in this study due to the non-retrievable nature of the LVIS device. Once the LVIS device was utilized for the radial force study, it could not be reinserted in the catheter for reuse.

The following **Figure 36-Figure 38** show the force required to push the device inside the catheter, placed in the MCA of the CW model. The orange dataset represents the baseline force needed to overcome catheter friction in a straight segment. The gray dataset indicates the force required to overcome the friction caused only by the vessel's tortuosity. The blue dataset represents the overall force necessary to overcome the friction caused by the movement of the device within the catheter (orange dataset) plus the vessel tortuosity (gray dataset). In all four repetitions across all devices, the maximum force was typically observed around the distance of 50 to 70 mm, corresponding to the ICA cavernous segment - the sharp curvature in the ICA before branching into the MCA and ACA. The figures showing the pulling forces can be found in the **Appendix A - Tracking Force Study.**

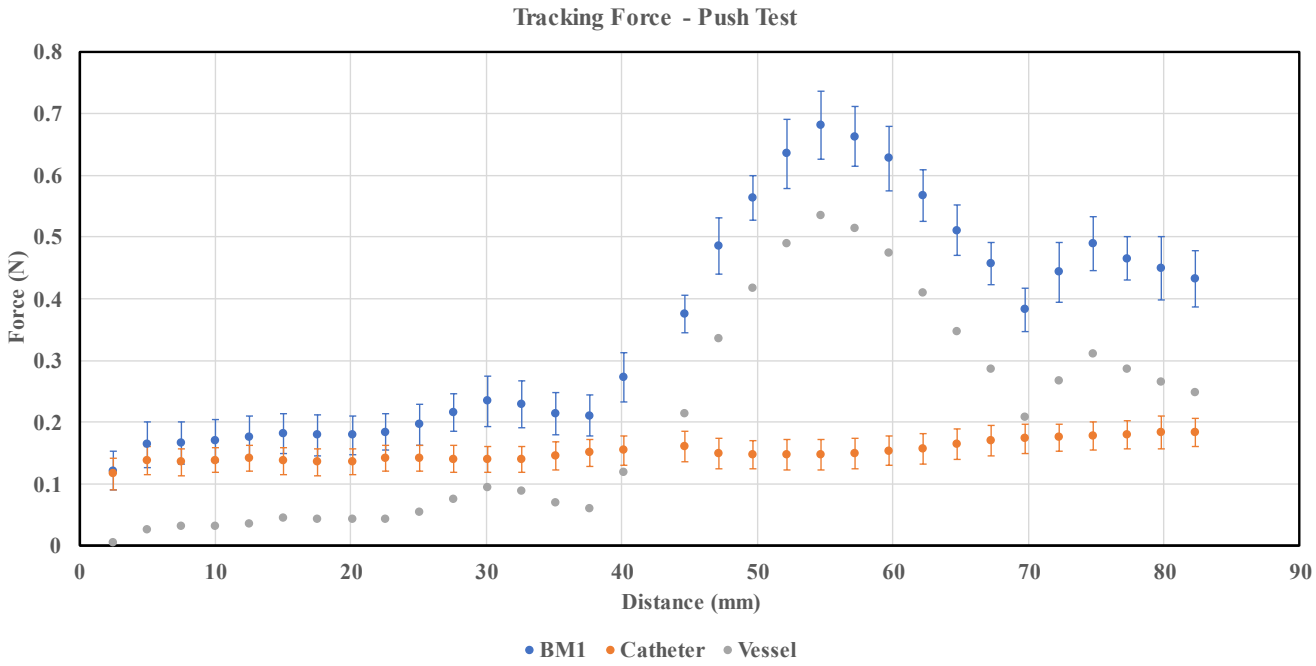

Figure 36: Tracking force to push BM1 into the CW model. Blue: total force with device and vessel tortuosity friction, orange: vessel tortuosity friction, and gray: vessel tortuosity friction alone.

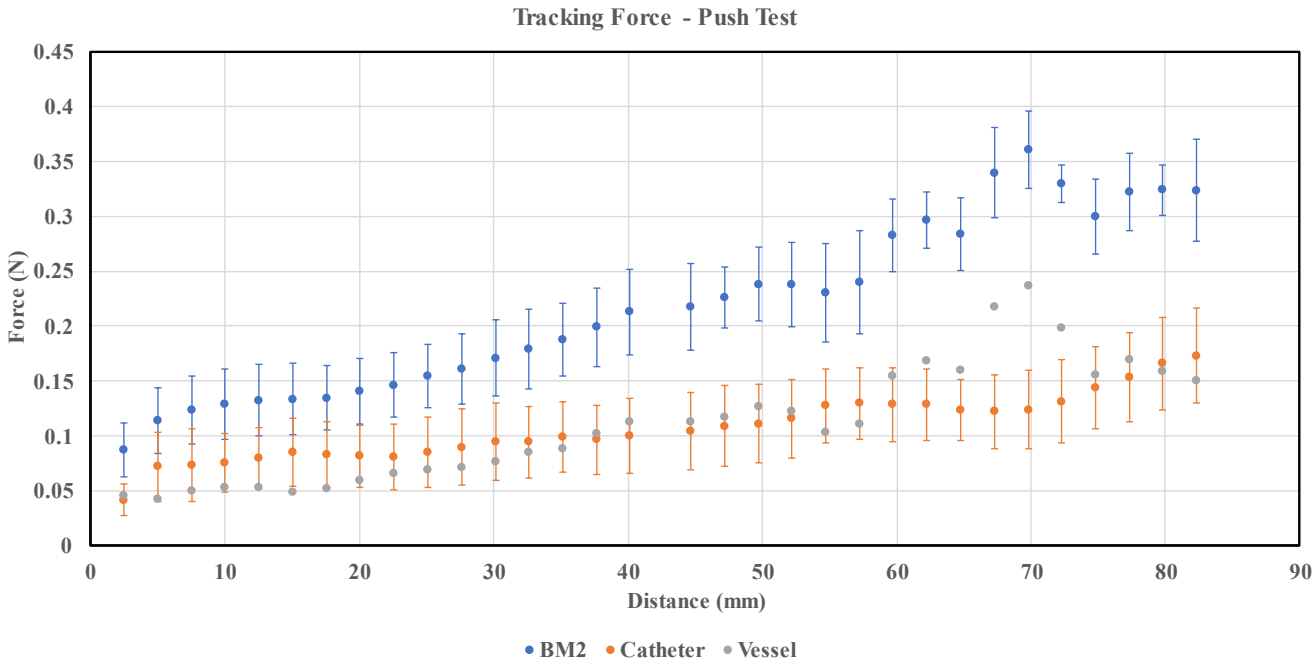

Figure 37: Tracking force to push BM2 into the CW model. Blue: total force with device and vessel tortuosity friction, orange: vessel tortuosity friction, and gray: vessel tortuosity friction alone.

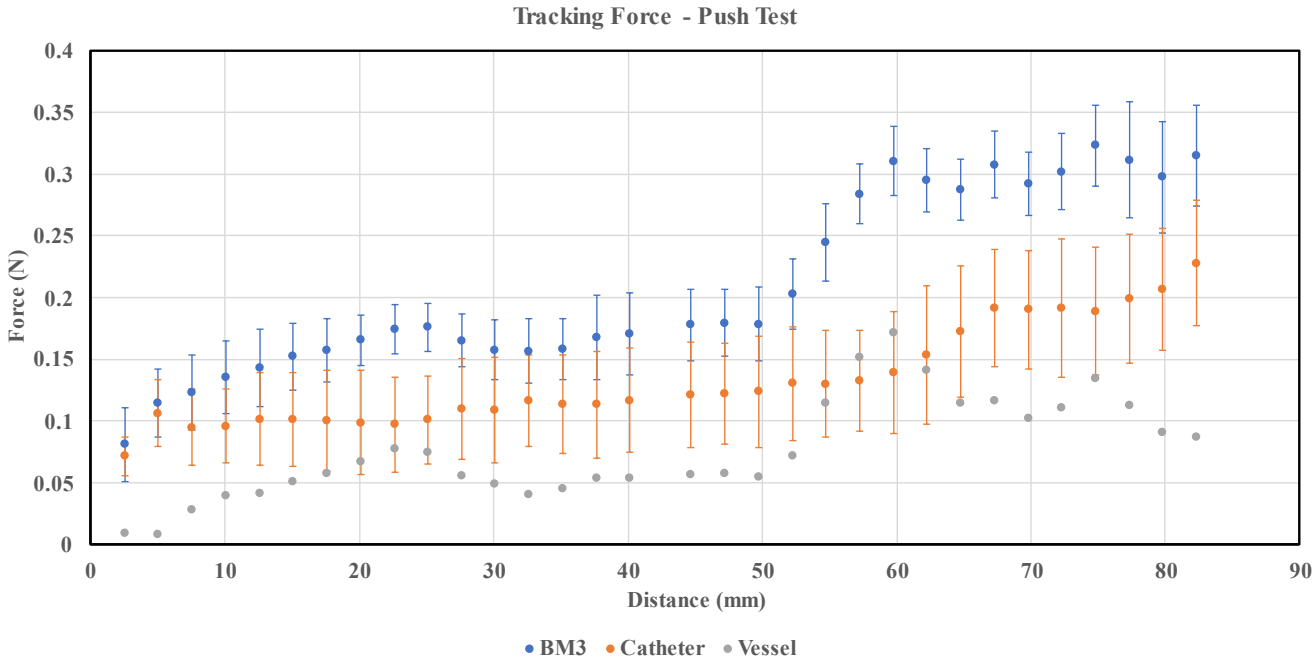

Figure 38: Tracking force to push BM3 into the CW model. Blue: total force with device and vessel tortuosity friction, orange: vessel tortuosity friction, and gray: vessel tortuosity friction alone.

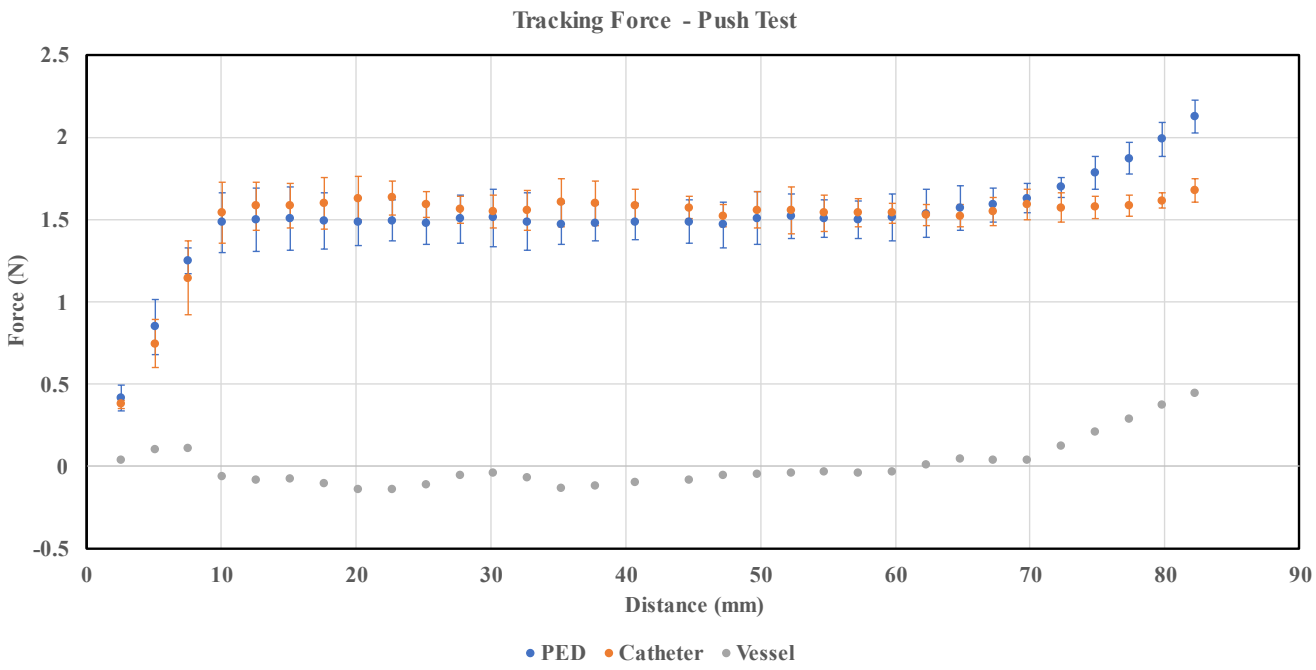

Figure 39: Tracking force to push PED into the CW model. Blue: total force with device and vessel tortuosity friction, orange: vessel tortuosity friction, and gray: vessel tortuosity friction alone.

The next two figures (**Figure 40**-**Figure 41**) provide a comparison of the pushing force for all devices in one figure. **Figure 40** presents a comparison of the total force (catheter plus vessel)

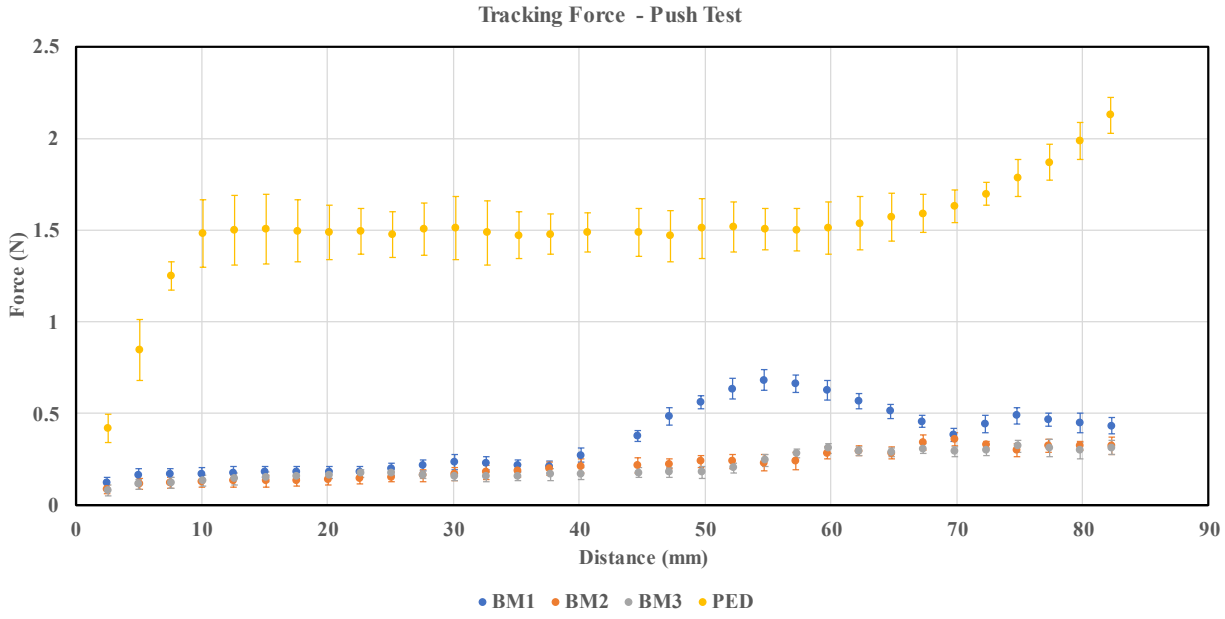

Figure 40: Total push force for all devices in CW model.

for all devices. As shown, a higher force is required to push the PED in the catheter (headway 27) inside the CW model compared to that of the balloon-mesh prototypes. The balloon-mesh prototypes exhibit similar behavior, except for balloon-mesh 1, where a higher amount of force is required to pass through the ICA cavernous segment, particularly around the 45-65 mm distance. This difference might be attributed to the varying lengths of the prototypes. Specifically, balloon-mesh 1 is approximately 40% and 70% larger than balloon-mesh 2 and 3, respectively (**Table 2**).

Figure 41 also presents a comparison of the average total push force across all devices - force required to overcome both friction in a straight catheter and the tortuosity of the vessel section. As shown, the total force for pushing the PED inside the catheter and model is significantly higher compared to the balloon-mesh prototypes, with the majority of the force attributed to passing through the catheter rather than overcoming the tortuosity of the vessel (F_{vessel} = 0.01 N). **Figure 42** can provide further insight into this observation.

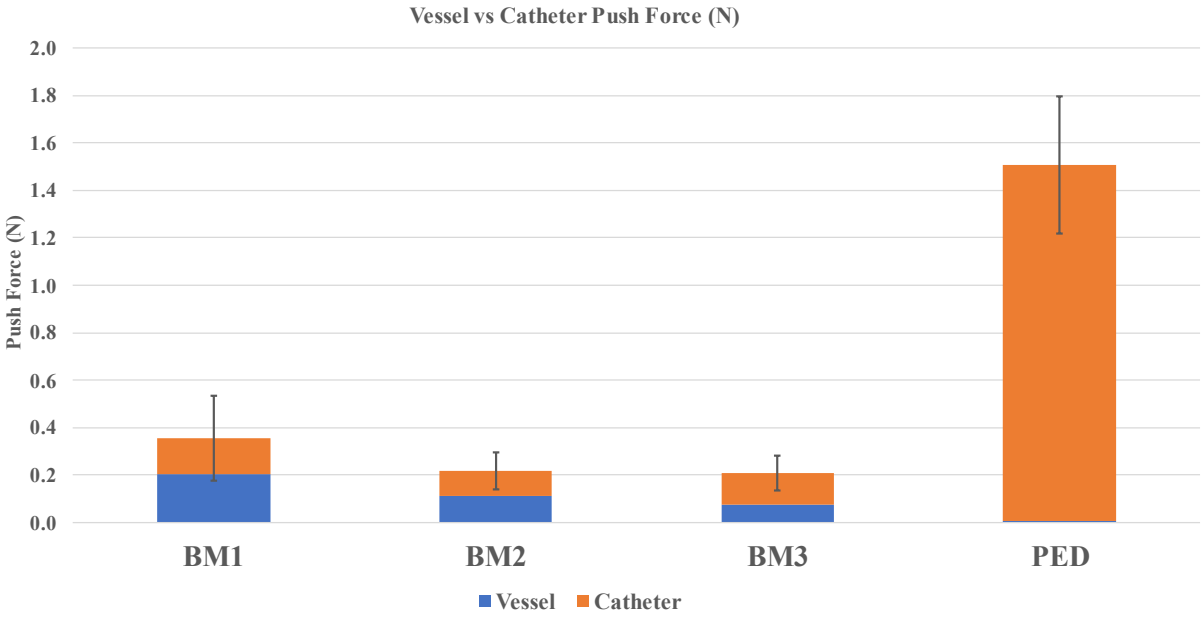

Figure 41: Push force in CW model - blue: force to overcome catheter movement, orange: force to overcome vessel tortuosity.

As shown in this figure, the PED delivery catheter is much smaller than the balloon-mesh delivery catheters (size information regarding the delivery catheters can be found in **Table 3**). Consequently, the tortuosity of the model does not contribute significantly to the additional force required for the PED to move within the catheter. Conversely, since we used larger catheters for delivering the balloon-mesh prototypes, the contact between the catheter and the vessel wall introduces additional friction, requiring more force for the balloon-mesh prototypes to pass through the same path. In the next stage of this research, as we optimize and scale the size of the balloon-mesh prototypes, we anticipate observing reduced force required to overcome vessel tortuosity (blue section) and, potentially, increased resistance inside the catheter (orange section).

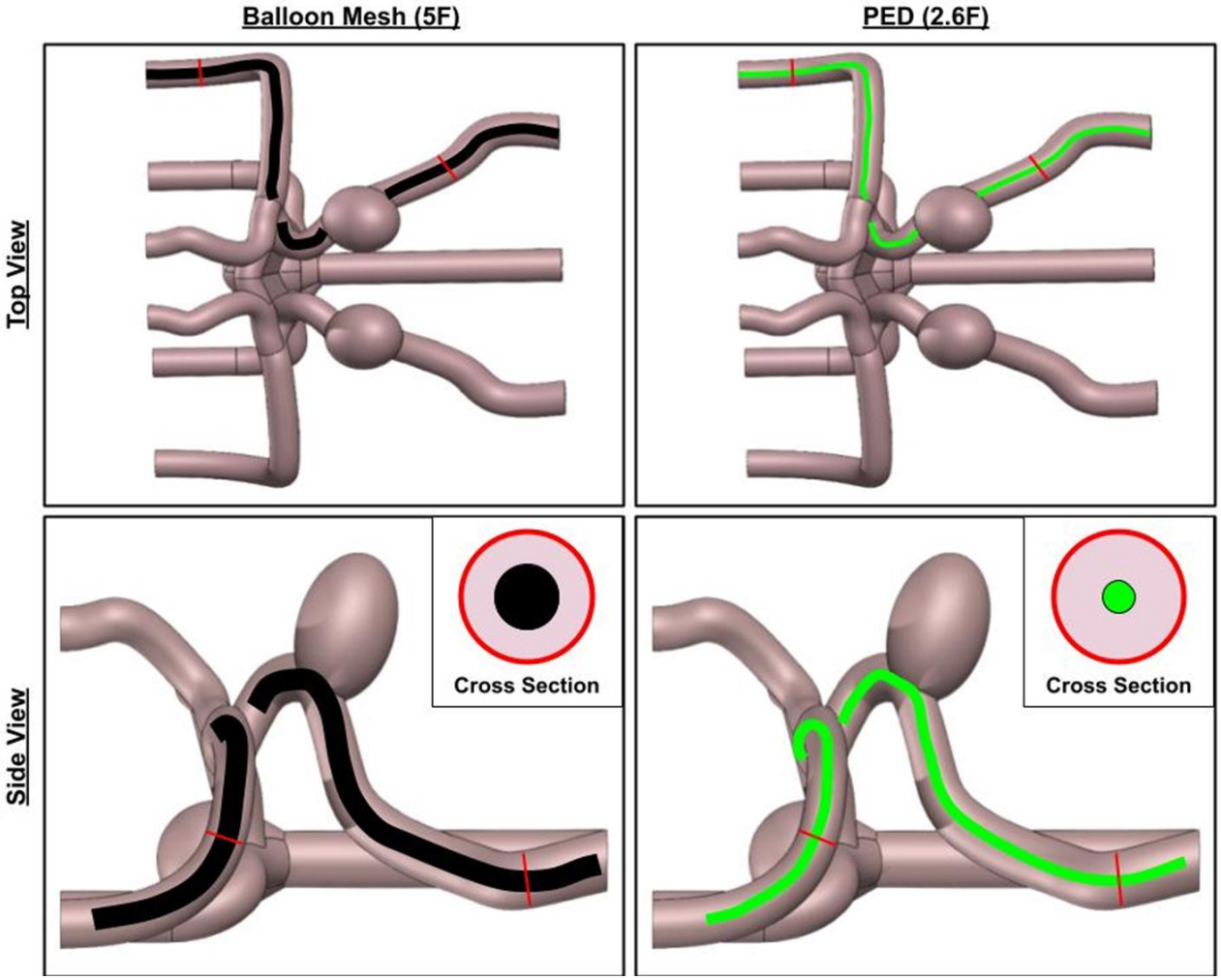

Figure 42: An illustration of two different delivery catheters in the CW model.

Table 6 presents a comprehensive statistical comparison among the devices, focusing only on the force required to overcome the tortuosity of the vessel. The percent difference, f-test, and t-test were applied for each comparison. For all comparisons except balloon-mesh 2 vs. balloon-mesh 3 and balloon-mesh 1 vs. PED, the f-test does not provide significant evidence to reject the null hypotheses ($p > 0.05$), allowing for the use of the equal variance t-test. However, in the comparison of balloon-mesh 2 with balloon-mesh 3 and balloon-mesh 1 with PED, the null hypotheses of the f-test were rejected, indicating unequal variances and requiring the usage of the non-equal variance t-test. The results of the t-test demonstrate significant evidence to reject the null hypothesis, indicating that there are significant differences between all devices ($p < 0.05$). It is essential to consider that the prototypes are made from the same materials and the same manufacturing process, but there are device size differences that may have influenced the results. The sensitivity of the t-test allowed us to detect even small differences in force results among the prototypes. Therefore, while the results indicate variations in force requirements, we must take into account the impact of the device size differences.

Table 6: a statistical comparison of push force considering only the tortuosity of vessel.

Device	BM1			BM2			BM3			PED		
	%diff	f.test	t.test	%diff	f.test	t.test	%diff	f.test	t.test	%diff	f.test	t.test
BM1				83%	0.000	0.006	165%	0.000	0.000	2390%	0.393	0.000
BM2	-45%	0.000	0.006				45%	0.126	0.006	1260%	0.000	0.001
BM3	-62%	0.000	0.000	-31%	0.126	0.006				840%	0.000	0.015
PED	-96%	0.393	0.000	-93%	0.000	0.001	-89%	0.000	0.015			

The **Figure 43** shows the energy required to push the devices inside the catheter placed in the CW model. The energy was calculated based on the area under the push force vs. distance curve (**Figure 43**). The energy needed to push the PED in the model was approximately five times greater than that required for the balloon-mesh prototypes.

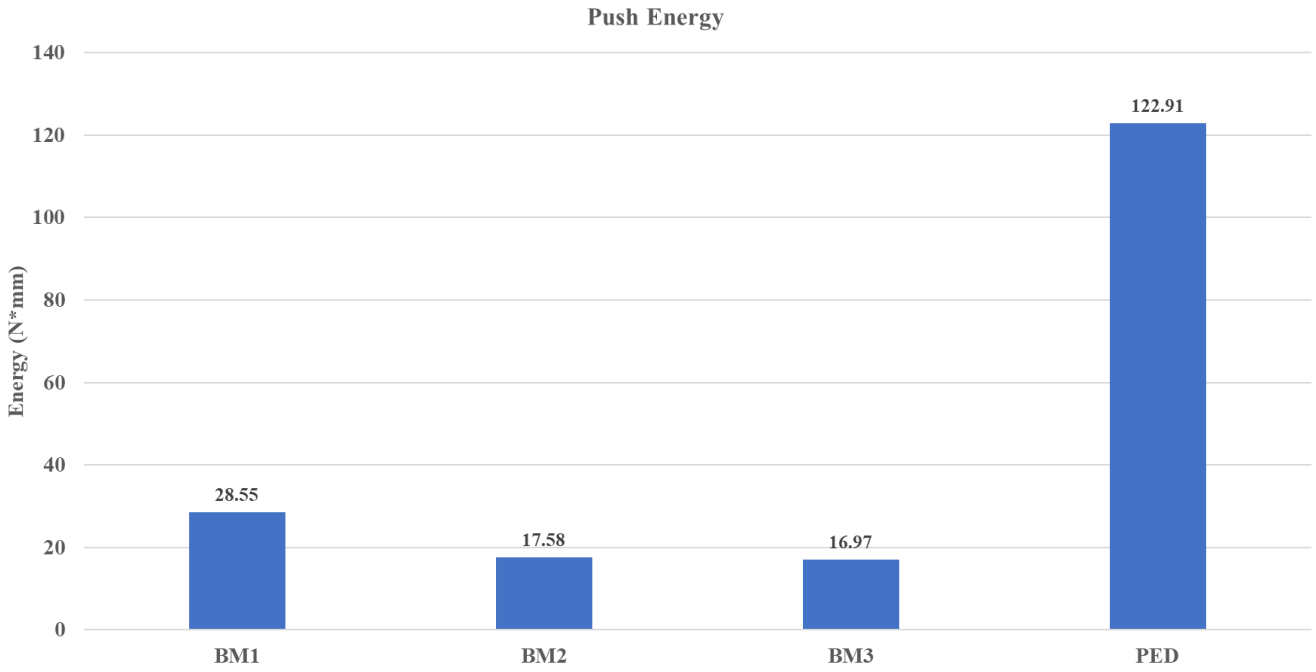

Figure 43: Push energy required to push the devices inside the CW model.

Discussion

The aim of this study was to develop a balloon-mesh prototype and assess its mechanical integrity to determine its suitability for practical applications in the treatment of cerebral aneurysms. The hypothesis was that the balloon-mesh prototypes would exhibit sufficient mechanical integrity, demonstrating structural strength and performance during testing. To assess the mechanical integrity of the balloon-mesh prototypes, we conducted radial force and tracking force studies.

The radial force study involved measuring the force at 50% compression of the device's outer diameter per unit length of the devices. This study aimed to compare the balloon-mesh prototypes with FDA-approved control devices, namely the Pipeline™ Flex embolization device (PED) and the Low-Profile Visualized Intraluminal Support Junior stent (LVIS Jr.).

The findings showed that the radial forces of the balloon-mesh prototypes were significantly lower compared to the control devices. The statistical analysis indicated significant differences between the balloon-mesh prototypes and the control devices, with LVIS Jr exhibiting approximately 10 times greater radial force than the prototypes, while PED exceeded LVIS Jr by approximately 10 times. Due to the absence of an FDA-approved temporary adjunctive stent device available for use as a control, PED and LVIS Jr, which are permanent devices, were selected for comparison. When considering permanent devices, an adequate level of radial force is crucial to secure the device at the aneurysm neck without damaging the vessel's endothelial layer. Insufficient radial force in such cases can lead to various risks, including device movement after deployment, blockage of downstream arteries leading to ischemic stroke, and potential endothelial damage as the stent moves within the artery. Therefore, maintaining sufficient radial force is vital to mitigate these risks. However, in terms of the temporary application of balloon-mesh devices,

as they are attached to a push wire, the risk of migration within the artery is minimized. Consequently, a minimum amount of radial force is required to support the embolization procedure. Further testing is necessary to determine whether the current radial forces exerted by the prototypes are adequate for this purpose.

The unexpected outcome was that there were noticeable variations in radial force between balloon-mesh 2 and the other prototypes (balloon-mesh 1 and balloon-mesh 3). However, the percentage difference in radial forces is below 20%, which is considered acceptable for the initial phase of prototyping, even with consideration of the different shape and size of the prototypes. Further analysis and investigation are needed to understand the factors contributing to these differences and their implications for the overall effectiveness and functionality of the prototypes.

The tracking force results of this study offer valuable insights into the force requirements for different balloon-mesh prototypes and a control device (PED) during navigation through a 3D-printed CW model. The measurements revealed that the maximum force was typically observed around 50 to 70 mm, corresponding to the challenging ICA cavernous segment due to vessel tortuosity. Comparing all devices, the PED required higher force to navigate the CW model than the balloon-mesh prototypes. Balloon-mesh 1 exhibited higher force requirements within the 45-65 mm distance, likely due to its larger size compared to the other prototypes.

The total force required to push the PED inside the catheter and model was significantly higher than the balloon-mesh prototypes, mainly due to overcoming friction inside the catheter. The smaller catheter used for PED delivery experienced less vessel tortuosity influence but introduced additional friction, requiring more force. Conversely, the larger catheters used for balloon-mesh prototypes experienced more vessel tortuosity impact but less friction within the catheter. In future research, as the size of the balloon-mesh prototypes is optimized and scaled, it

is expected that the force required to overcome vessel tortuosity may decrease, while resistance inside the catheter may increase, a crucial consideration for prototype development.

The comprehensive statistical comparison highlighted significant differences in force requirements between all devices, except for the comparisons of balloon-mesh 1 vs. balloon-mesh 3 and balloon-mesh 1 vs. PED. The f-test results indicated unequal variances in these comparisons, requiring the use of the non-equal variance t-test. In all cases, the t-test results showed significant differences in force requirements, suggesting that despite the same materials and manufacturing process of balloon-mesh prototypes, the size differences among the devices influenced the results. Once the final prototype design is finalized, it is anticipated that these significant differences will reduce through the consistent sizes manufacturing. This will result in a consistent outcome in subsequent iterations of prototype development.

Conclusion

The development and mechanical integrity testing of the balloon-mesh prototypes provided valuable insights into their potential as a novel device for the treatment of cerebral aneurysms. The radial force study revealed that the balloon-mesh prototypes exhibit significantly lower radial forces compared to the FDA-approved control devices, LVIS Jr and PED. These lower radial forces are expected since the balloon-mesh devices are intended for temporary application and attachment to a push wire, minimizing the risk of migration within the artery. Considering the modifications planned for the next iterations of prototyping, such as altering the braid angle, using larger wires, and implementing a heat treatment process to modify the nitinol shape-memory activation force, the radial force is expected to vary. However, further testing is required to determine whether the current radial forces are adequate for the intended purpose.

The tracking force study highlighted the force requirements for navigating the balloon-mesh prototypes and the control device (PED) through a 3D-printed CW model. The study demonstrated that the maximum force required was typically observed around the ICA cavernous segment due to vessel tortuosity. The balloon-mesh prototypes required less force than the PED to navigate the model, with balloon-mesh 1 exhibiting slightly higher force requirements, likely due to its larger size. After finalizing the design, maintaining consistent manufacturing sizes will validate uniform mechanical outcomes.

In conclusion, the balloon-mesh prototypes show promise as a potential device for the treatment of cerebral aneurysms, offering a unique combination of temporary aneurysm neck protection and continuous parent artery blood flow. Further optimization and scaling of the prototypes may lead to reduced push force requirements to overcome vessel tortuosity while potentially increasing resistance inside the catheter. This research provides a foundation for the

future development and refinement of balloon-mesh prototypes, ultimately aiming to improve the outcomes of cerebral aneurysm treatments and patient care.

CHAPTER 4 – AIM II – *In-vitro* Evaluation

Aim of Research

Assess, optimize, and validate the effectiveness of balloon-mesh prototypes in an *in vitro* aneurysm model.

Hypothesis: *We hypothesize that the prototype can be tested in a physiologically-relevant benchtop flow model and provide aneurysm neck protection while maintaining blood flow in the parent artery, which maximizes aneurysm sac treatment during complementary device deployment and prevents device entanglement or device migration into the parent artery. In this study, the complex hemodynamics of cerebral vessels can be monitored and analyzed with the benchtop model to provide insights into endovascular aneurysm treatments.*

Introduction

The treatment of intracranial aneurysms poses a substantial medical challenge. These novel prototypes are designed to enhance aneurysm treatment outcomes by promoting better neck healing and reducing aneurysm recanalization rates. This study focuses on assessing, optimizing, and validating the effectiveness of balloon-mesh prototypes within advanced *in-vitro* aneurysm models.

Our hypothesis is that the prototype can be successfully tested using a physiologically-relevant benchtop flow model. This model aims to demonstrate the device's ability to provide protection at the aneurysm neck during complementary device deployment while ensuring continuous blood flow in the parent artery. Achieving this balance is crucial as it maximizes device placement within the aneurysm sac, improving neointimal vessel healing and eliminating long-term aneurysm recanalization rates. Additionally, the balloon-mesh design aims to prevent device migration into the parent artery, minimize turbulent effects within the aneurysm, and provide

reduced flow in the aneurysm sac. With the help of this advanced benchtop system, we gain valuable insights into the complex hemodynamics of cerebral vessels, offering potential advancements in endovascular aneurysm treatments.

In the following sections, we investigate the details of the balloon-mesh prototypes in an *in-vitro* aneurysm model and assess their performance under physiological conditions. This includes exploring the *in-vitro* system and understanding endovascular pressures. Furthermore, we discuss potential approaches to enhance the prototypes' performance. Through these comprehensive investigations, we aim to validate our hypothesis and establish the practical applicability of the balloon-mesh device in treating cerebral aneurysms. Our objective is to significantly contribute to the development of safer and more effective treatment procedures for patients and clinicians dealing with intracranial aneurysms.

Methods

The research conducted at BDL involves a comprehensive evaluation of the innovative balloon-mesh prototypes through a two-step validation process. Step 1 focuses on prototype delivery testing, where three balloon-mesh prototypes were tested using the BDL's level 1.0 flow model. The performance of the prototypes was compared to the commercial control device – Pipeline Embolization Device (PED). Step 2, prototype efficacy testing, assessed the device's effectiveness compared to the control device. The testing was conducted in the fluoroscopic surgical suite, utilizing a 3D-printed CW model to simulate an endovascular environment. The study aimed to validate the balloon-mesh prototypes and determine its statistical comparison with the control device, preparing essential primary steps for a promising advancement in endovascular technology.

Prototype Delivery Testing

At Pivot Medical, three prototypes of a balloon-mesh were manufactured (**Figure 26**). These prototypes underwent testing using BDL's level 1.0 flow model, which simulates blood flow in a vessel with an inner diameter of 4.0 mm. The testing was conducted in an *in-vitro* flow system. During the testing, a 5F microcatheter (**Table 3**) was used to deliver the prototypes, and its performance was compared to the control device - PED.

The assessment steps for both the prototype and control device were as follows:

1. Measure: The initial outer diameter (OD) of the balloon-mesh and the control device before deployment.

2. Insert devices into the delivery catheter for deployment.

3. Device deployment: The balloon-mesh and control device were deployed in the vessel model using the attached balloon-mesh push-wire.

4. Measurement: The pressure drops across the vessel branch was measured before and after deploying the catheters and devices.

5. Noted any variations or complications in device expansion using fluoroscopy imaging.

6. Device retrieval: The devices were retrieved by pulling back on the push-wire into the catheter.

7. Note any variations or complications during the device retrieval process.

Prototype Efficacy Testing

The effectiveness of the balloon-mesh prototypes was evaluated in comparison with the control device (PED). It was conducted in the fluoroscopic surgical suite at the NAU, utilizing the device testing equipment as well as the *in vitro* flow measurement equipment located in the BDL. Statistical equivalence was determined by comparing the performance of the balloon-mesh prototypes to that of the control device. A simulated endovascular environment was used to test the prototypes. The prototypes were introduced into 3D-printed CW models under fluoroscopy using simulated interventional surgical techniques. The function of the model, the flow rate, the pulsatile pressure, and the real-time FPR were recorded during the delivery of prototypes and control devices. This bench-top system is the first system of its kind to provide a real-time measurement of the flow effects in a CW model. The *in-vitro* CW model was derived from human CT scans - all at anatomical scale - to design the *in vitro* CW model based on the flow resistance model and literature data (**Figure 44**). 3D-printed from soft UV-cured polymers (PolyJet process), the *in-vitro* CW model exhibits highly tunable mechanical properties. With this model, unlike traditional silicone and glass models, the luminal wall friction is

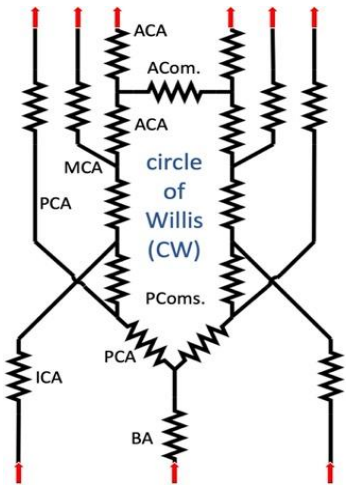

Figure 44: flow resistance branches of the CW.

physiologically accurate, eliminating the need for lubricant or surfactant additives which can interfere with the deployment and functioning of various endovascular devices. **Figure 45** shows that the distal and proximal branches of the model are equipped with flow resistance valves and pressure transducers for the monitoring of pressure, flow, and FPR (p_p and p_d) in real-time.

Advanced in vitro model:

In-vitro models of 3D-printed vessels represent the average arterial sizes on both sides (L and R) derived from human CT scans (from a previous retrospective study conducted by BNI) and from literature references.[87] We connected the 3D-printed vessel models to the BDL's advanced *in-vitro* flow model created specifically for the testing of endovascular devices in order to assess the usability of the balloon-mesh prototypes (**Figure 45**). In the model, devices are introduced while undergoing standard interventional surgical techniques (on a bench or under fluoroscopic guidance).

BDL's 3D printer, the Stratasys Object260 Connex3 (multi-material UV 3D printer), is capable of printing vessel IDs with an accuracy of 30 μm. Furthermore, Deltran© pressure transducers are connected proximally and distally to each vessel branch to verify if there has been any local disruption in the flow associated with the deployment of the balloon-mesh and control device (**Figure 45-Top**). Pressure waveforms are collected with a NI 9239 Data Acquisition (DAQ) module at the rate of 20 data points per second and displayed in real-time in LabVIEW® (**Figure 45-Bottom**). As a result of the system's ability to record average pressure drops (p_d/p_p and $\%\,\Delta P$) and flow rates over extended testing periods, it can be used to verify FPR after the device has been deployed. Using the microcatheter, the balloon-mesh prototypes were deployed into the 3D-printed CW model across an ICA para-clinoid aneurysm (**Figure 46**) following endovascular

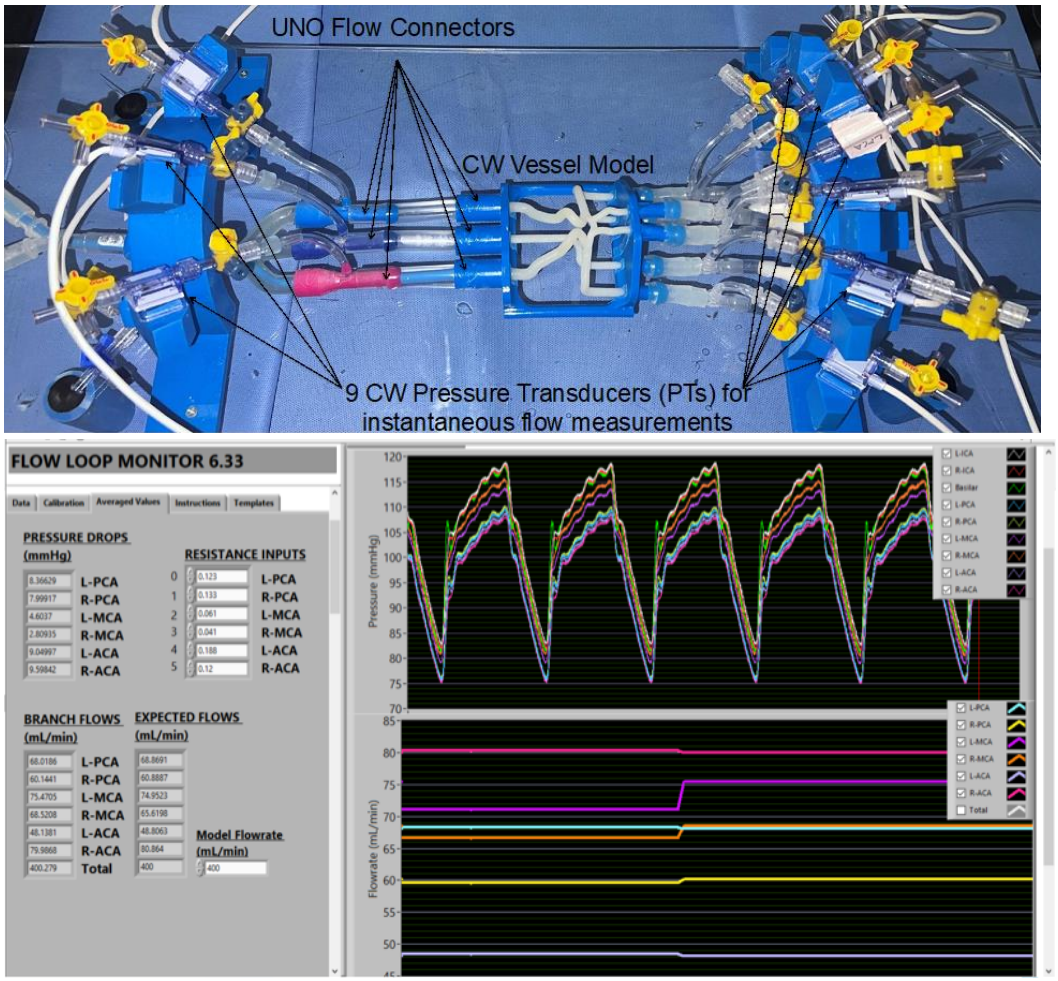

Figure 45: Top) model of the circle of Willis (CW), 3D printed by the BDL, with flow connectors and CW pressure transducers (PTs), Bottom) real-time pressure changes in each vessel branch with average flow rates (via NI-DAQ hardware and LabVIEW software).

surgical techniques under fluoroscopy. Our team determined the level of difficulty of the following prototype tracking, deployment factors, and aneurysm neck coverage:

1. Trackability, ease of pushing the balloon-mesh/control through the entire microcatheter length.
2. Deployment ease of balloon-mesh/control (retracting the microcatheter, landing the device at the aneurysm neck)
3. Fluoroscopic visualization and assessment of the deployed device.
4. Fluoroscopic contrast injection, assess Parent artery and aneurysm sac flow effects (through the device) via fluoroscopic contrast injection.

5. Balloon-mesh retrieval ease, note any retrieval variations/complications.
6. FPR calculations: pre- and post-prototype/control deployments, compared to previous CFD analysis.

To assess the trackability, deployment, and retrieval ease, a simple semi-quantitative scoring system was used (**Table 7**).

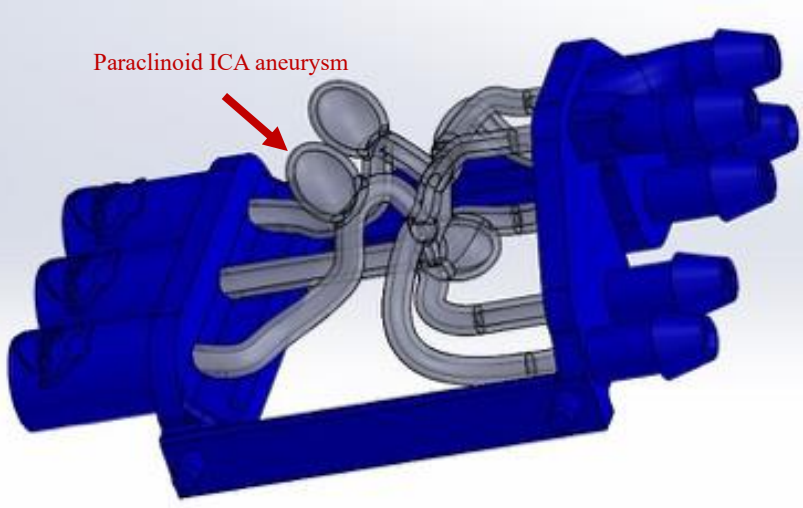

Figure 46: CAD rendering of 3D-printable ICA and basilar aneurysm model.

Aneurysm Neck Coverage Evaluation.

The evaluation of aneurysm neck coverage involved injecting contrast materials with and without devices placed in the parent artery at the aneurysm neck. Fluoroscopy videos were recorded to further assess the aneurysm neck coverage provided by each prototype and control device. A simple semi-quantitative scoring system was also employed to assess the devices effectiveness in covering the neck of the aneurysm, evaluating both intra-aneurysmal flow and flow pulsatility within the aneurysm sac. (**Table 7**).

Table 7: Semi-quantitative scoring system.

Delivery System Score		Aneurysm Neck Coverage Score	
Trackability / Deployment / Retraction		Intra-aneurysmal Flow	Pulsatile Flow
0	Minimal	Not present	Not present
1	Mild	Minimal Flow	Minimal
2	Moderate	Moderate Flow	Moderate
3	Marked	Maximum Flow	Maximum Pulsatile Flow

Results

The results of the evaluation of the innovative balloon-mesh prototypes are presented in this section. Step 1 of the validation process focused on prototype delivery testing, which involved testing three balloon-mesh prototypes using BDL's level 1.0 flow model. The performance of these prototypes was compared to that of the commercial control device - Pipeline Embolization Device (PED). During this testing, a 5F microcatheter was used to deliver the prototypes, and various parameters were measured, including pressure measurements before and after deploying the devices, and observations of stent expansion using fluoroscopy imaging. Step 2, prototype efficacy testing, aimed to assess the effectiveness of the balloon-mesh prototypes compared to the control device (PED). This testing was conducted in the fluoroscopic surgical suite at NAU, utilizing a 3D-printed CW model to simulate an endovascular environment. The functionality of the model, flow rate, pulsatile pressure, and real-time flow pressure ratio (FPR) were recorded during the delivery of prototypes and control devices. Additionally, an evaluation of aneurysm neck coverage involved injecting contrast materials with and without devices placed in the parent artery at the aneurysm neck, and fluoroscopy videos were recorded to assess the aneurysm neck coverage provided by each prototype and control device.

Prototype Delivery Testing

In the prototype delivery testing phase, the balloon-mesh prototypes were deployed in the simple vessel model (**Figure 47**), and pressure measurements were recorded before and after the deployment process. Fluoroscopy imaging was utilized to visualize any variations or complications that might arise during the deployment of the devices. Furthermore, the performance of the prototypes was directly compared to the control device (PED).

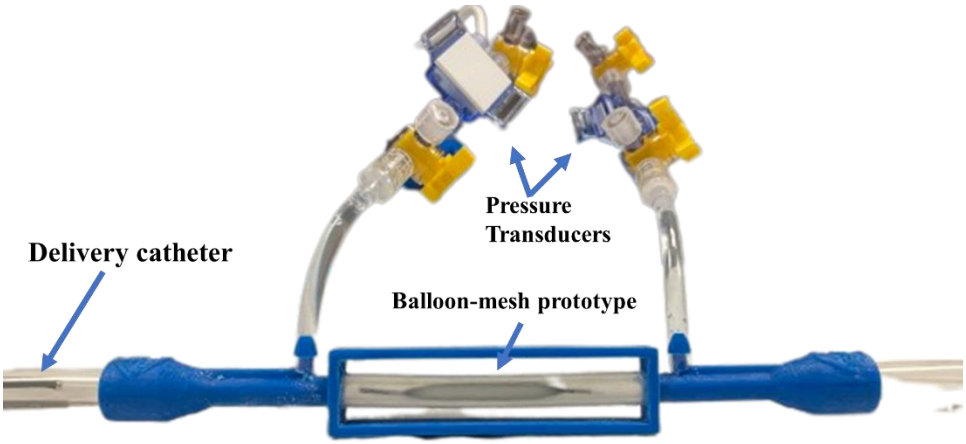

Figure 47: Placement of balloon-mesh prototypes in a simple model.

To deliver the balloon-mesh prototypes, we simulated endovascular catheter delivery and aneurysm treatment techniques. Following steps were followed (**Figure 48**):

1- A balloon-mesh catheter was inserted into the model, placed across the neck of the aneurysm.

2- Once the catheter was in position, the balloon-mesh was deployed from the microcatheter tip using an attached push-wire/retriever, allowing it to expand and conform precisely to the various morphologies of the aneurysm neck.

3- This crucial step ensures the aneurysm neck's protection.

4- The fine mesh structure of the balloon-mesh provides a continuous and smooth surface at the aneurysm neck, effectively minimizing inflow and outflow into the aneurysm sac.

5- Fully deployed balloon-mesh device significantly reduces the risk of the device migration while maintaining a continuous flow of blood through the parent artery.

6- Finally, the balloon-mesh was retrieved back into the microcatheter, completing the procedure. The balloon-mesh technique ensures a precise and controlled treatment of aneurysms, promoting better patient outcomes and reducing potential complications.

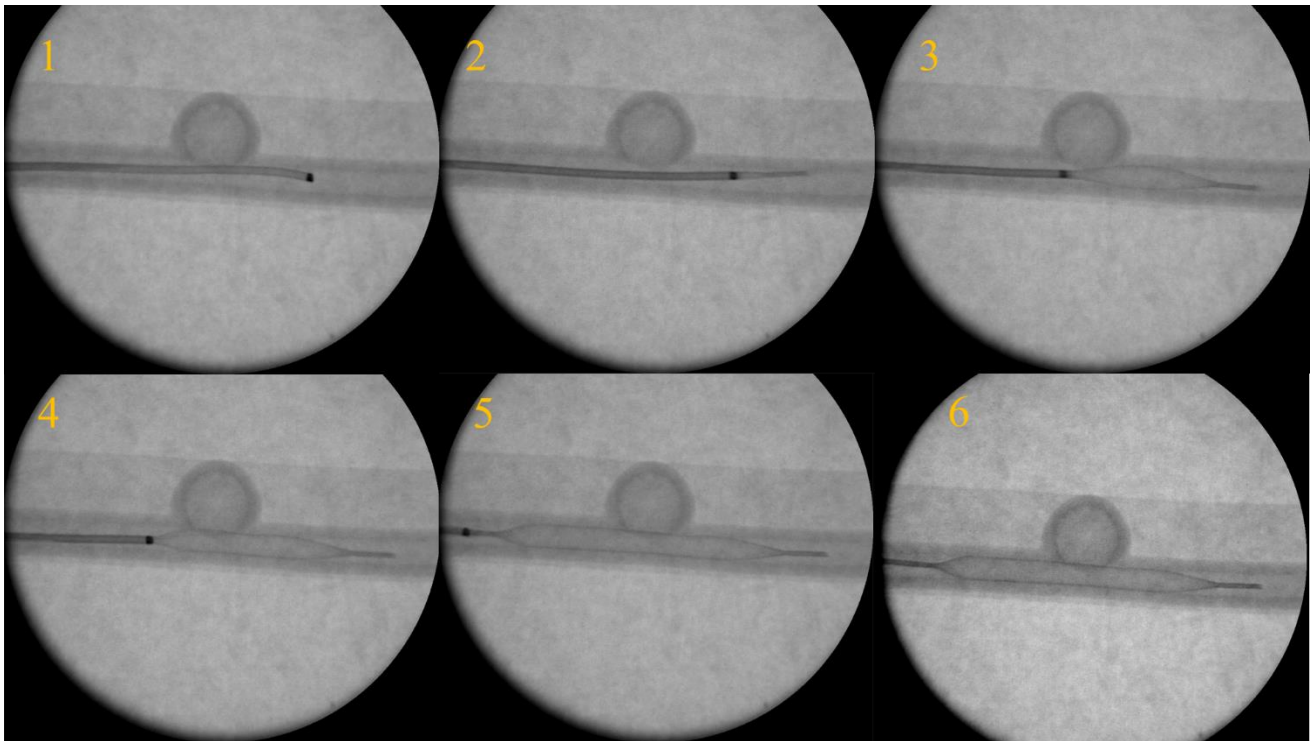

Figure 48: Balloon-mesh delivery and retrieval process: 1) Placing the delivery catheter inside the model, 2) Pushing the prototype out of the catheter while pulling the catheter back, 3) Self-expansion mechanism of balloon-mesh prototypes during deployment, 4) Ensuring a smooth surface at the aneurysm neck, 5) Fully deploying the balloon-mesh, and 6) Successfully completing the balloon-mesh delivery process.

Figure 49 shows the pressure waveform of the simple model with no device/catheter placed inside. To assess the impact of different devices placed inside the model, we utilized proximal and distal pressure transducers (**Figure 47**) to record the pressure readings. The same measurements were then repeated with delivery catheters positioned inside the model (**Appendix**). These measurements were used to normalize the pressure data across the prototypes and the control device.

The **Figure 50Figure 53** illustrate the pressure readings across the devices placed in the model. These figures demonstrate that prototypes caused a pressure drop across the model. To assess the potential ischemic risk resulting from flow disruption caused by the prototypes, the Flow Pressure Ratio (FPR) discussed in detail in Chapter 2 was employed. **Figure 54** presents the FPR result for all devices in the simple model. FPR values below 0.75 are indicative of an ischemic risk. As shown in this figure, both the prototypes and the control device do not contribute to an increased ischemic risk, suggesting that there is sufficient blood flow downstream to avoid ischemia.

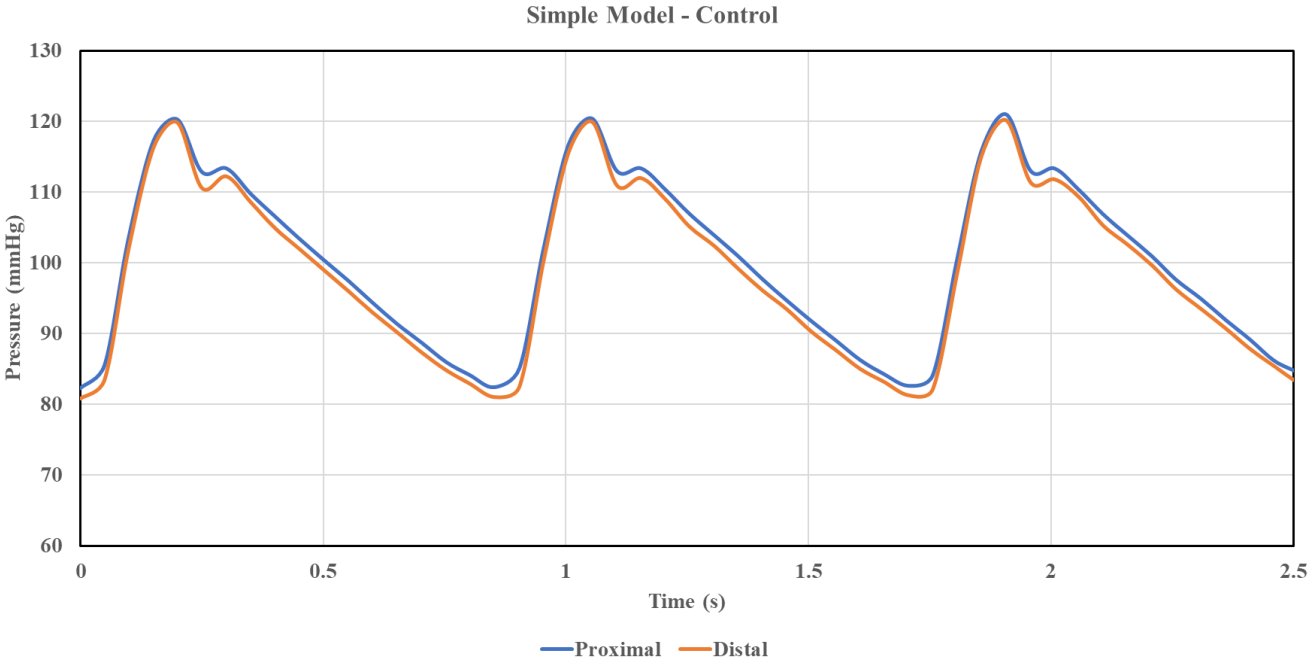

Figure 49: Proximal and distal pressures across the simple model with no devices placed.

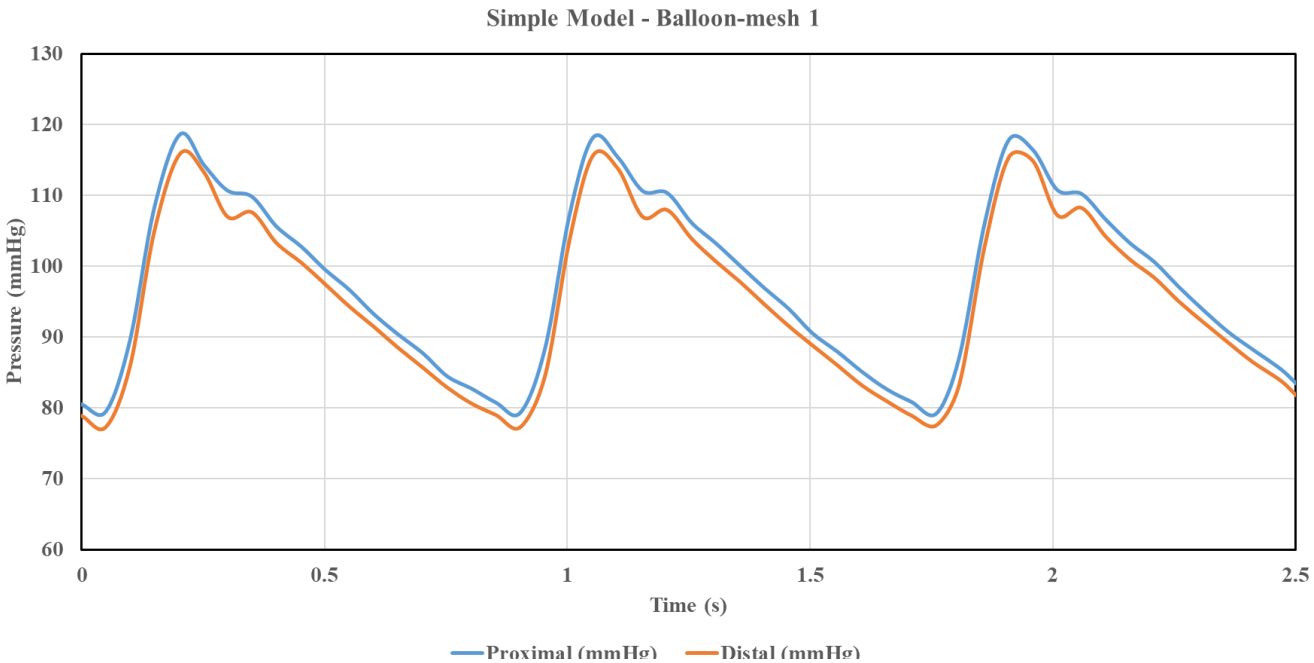

Figure 50: Proximal and distal pressures across the simple model with balloon-mesh 1 placed.

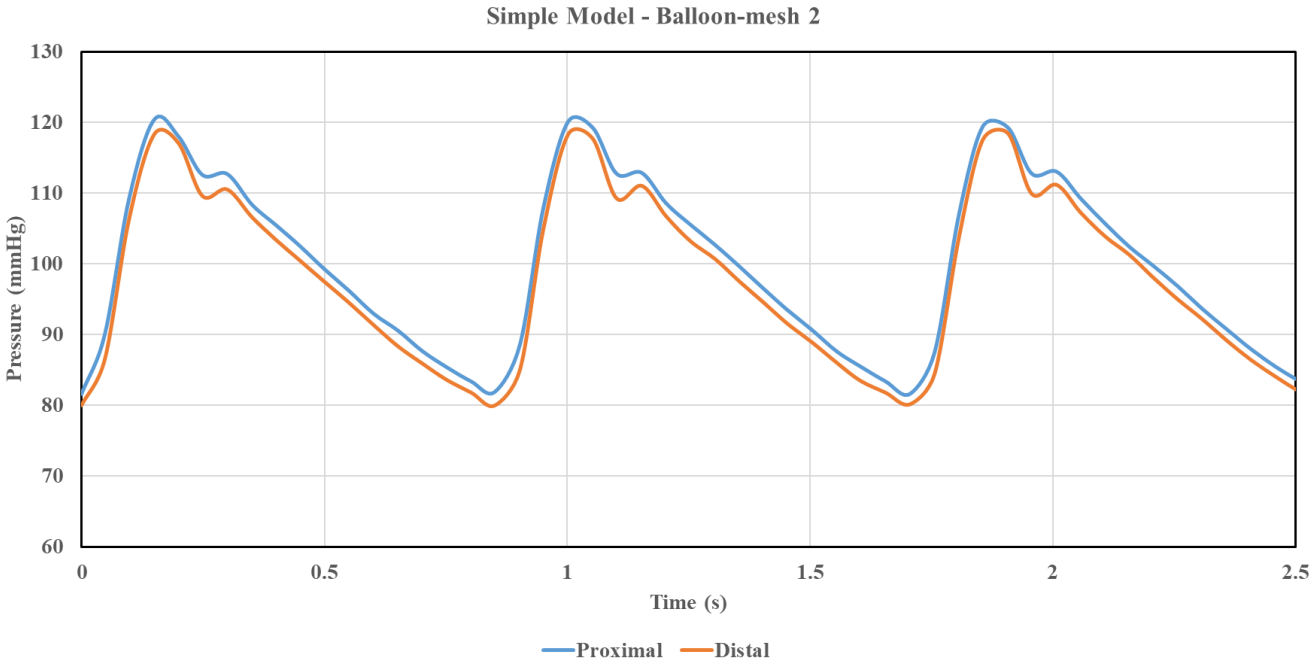

Figure 51: Proximal and distal pressures across the simple model with balloon-mesh 2 placed.

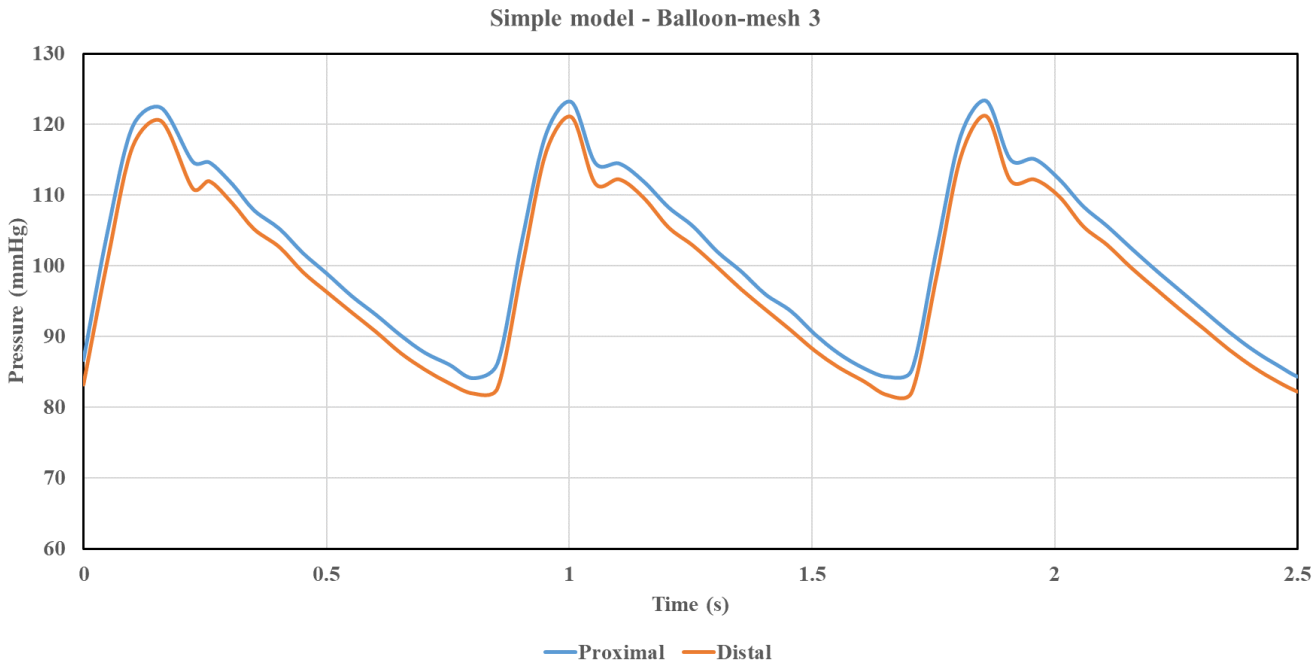

Figure 52: Proximal and distal pressures across the simple model with balloon-mesh 3 placed.

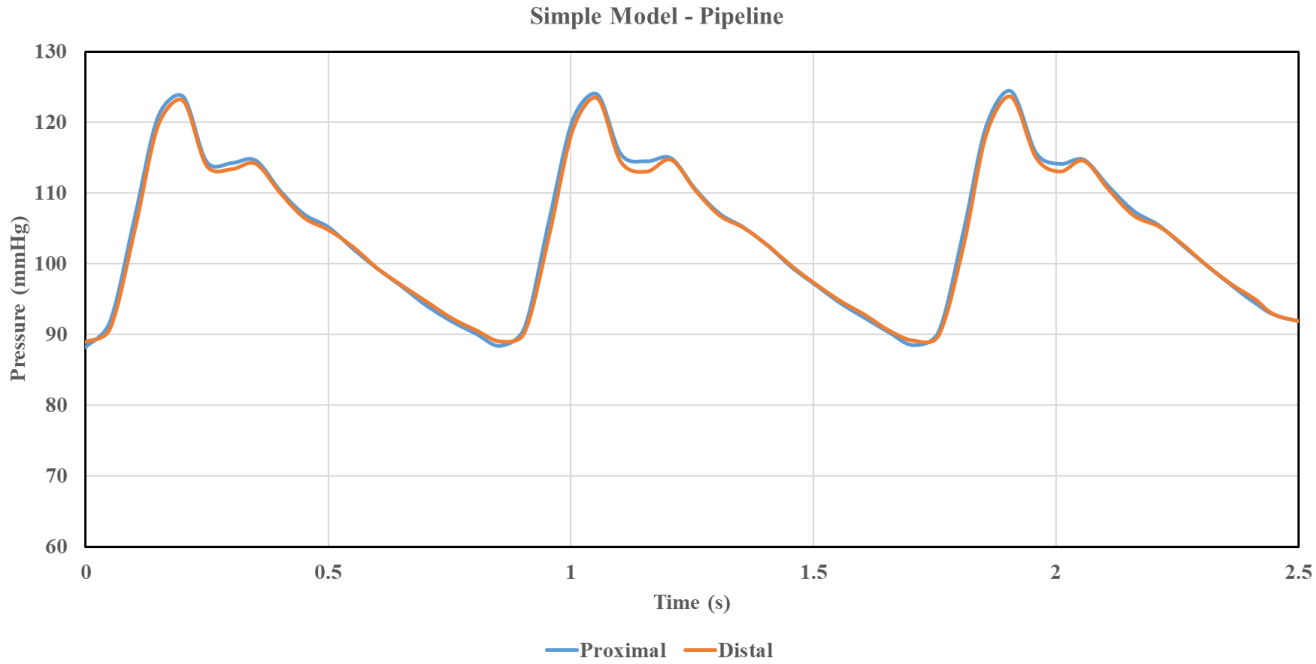

Figure 53: Proximal and distal pressures across the simple model with PED placed.

Table 8 displays the statistical analysis of pressure drops and FPR for both the prototypes and the control device – PED. Within the simple vessel model, the balloon-mesh prototype exhibited the highest pressure drop (ΔP = 2.143 mmHg), while the control device, PED, demonstrated the lowest pressure drop (ΔP = 0.312 mmHg). Notably, all devices displayed FPR values near 1, signifying that they have minimal impact on pressure drops, thus reducing the risk of ischemic stroke.

Table 8: a statistical analysis of pressure drops and FPR of devices in the simple model.

Devices	ΔP		FPR	
	Mean	σ	*Mean*	σ
BM1	2.143	0.656	0.978	0.006
BM2	1.937	0.605	0.980	0.006
BM3	1.489	0.475	0.985	0.005
PED	0.312	0.698	0.997	0.007

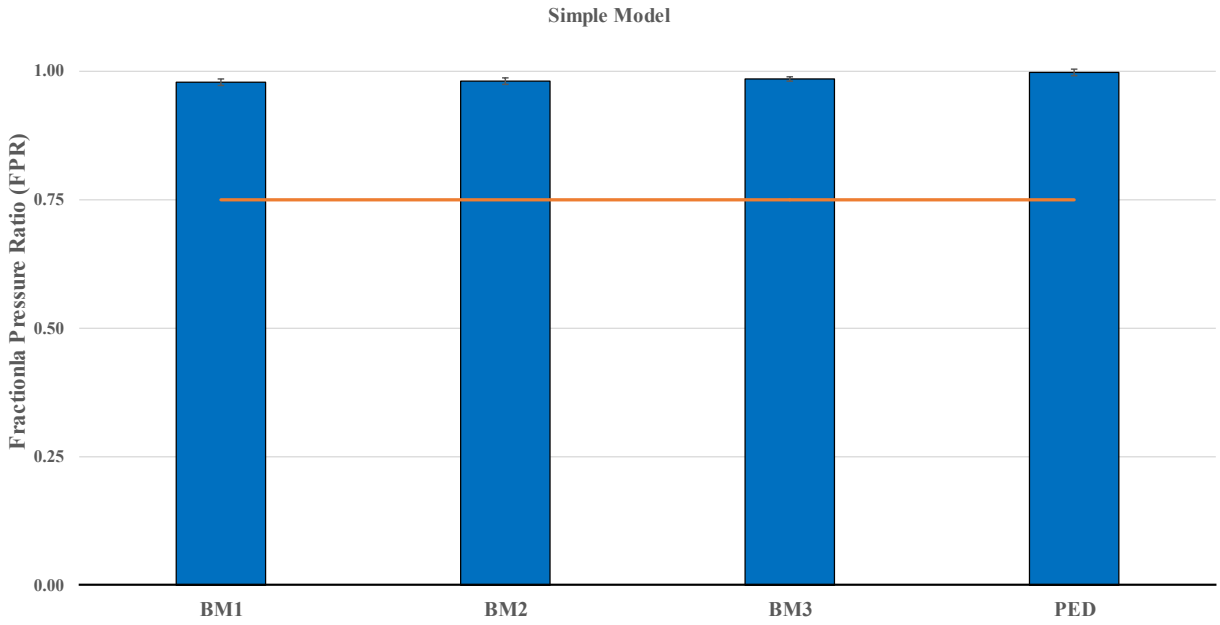

Figure 54: FPR results for all devices in the simple model.

In summary, the prototype delivery testing phase allowed for a comprehensive assessment of the balloon-mesh prototypes' performance, including their ability to be delivered successfully through microcatheters and their effectiveness in terms of stent expansion and retrieval. The results of this phase contribute crucial data for understanding the feasibility and potential of the balloon-mesh prototypes as a promising advancement in endovascular technology.

Prototype Efficacy Testing

The following section presents the results obtained from the prototype efficacy testing phase, which aimed to further evaluate the balloon-mesh prototypes' performance in comparison to the control device (PED). This phase involved utilizing the advanced *in-vitro* flow model at the BDL, simulating an endovascular environment 3D-printed CW models. Detailed assessments were performed, including tracking of the prototypes, their deployment, fluoroscopic visualization, flow assessment, and retrieval.

Prior to device placement, we recorded control pressure data (**Figure 55**). For each device, a separate control group of pressure data was also recorded when the delivery catheters were placed in the desired position without deploying any device in the model. These corresponding figures can be found in the **Appendix B**. We utilized these control groups to normalize the pressure data and isolate the effects of only the prototypes and the control device in the CW model. As shown in the **Figure 55**, the inlet branches – left and right Internal Cerebral Artery (L- and R-ICA) and Basilar artery – were set to a pressure of approximately 120/80 mmHg. Conversely, the outlet branches – Posterior Cerebral Arteries (PCA), Middle Cerebral Arteries (MCA), and Anterior Cerebral Arteries (ACA) – exhibited smaller pressure readings due to the flow being divided into six branches. Pressure drops can be assessed across various arterial groups. Cerebral inflows, the basilar and ICAs, were taken as proximal pressure references. The largest pressure drop occurs

across the ACAs due to their smaller size, resulting in higher resistance. The pressure drop concerning MCAs and PCAs is depend on artery sizes, given the physiological variability in size between left and right arteries.

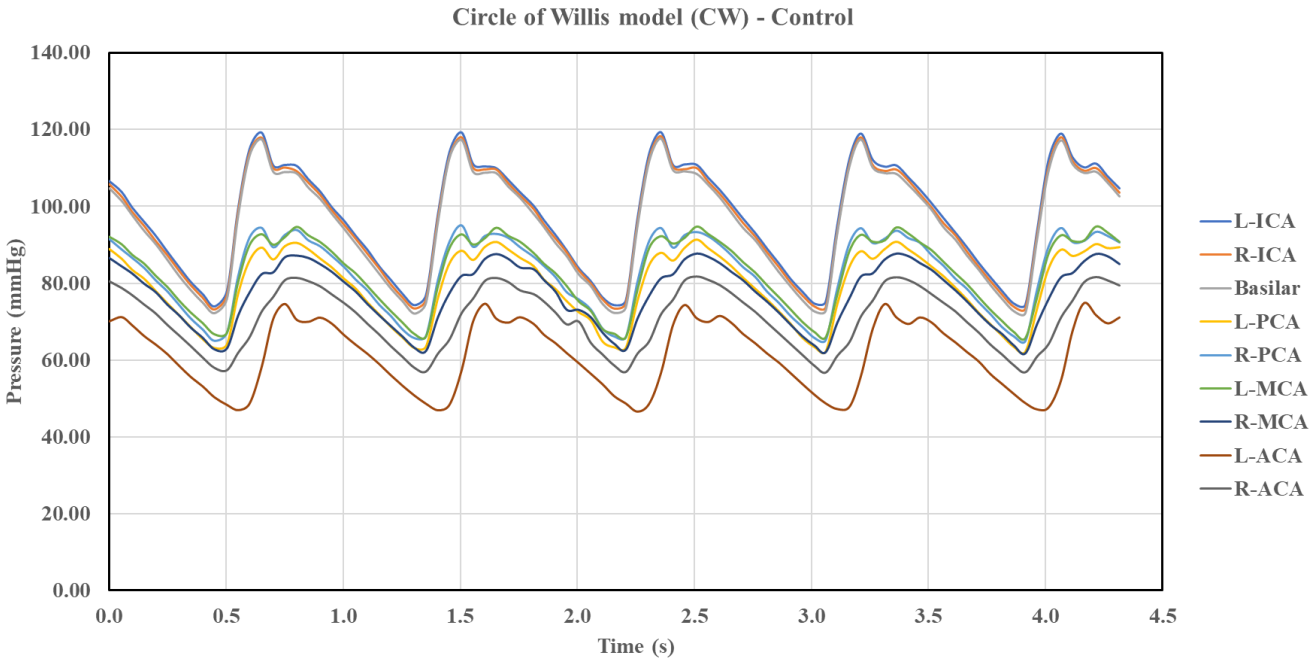

Figure 55: Control group: Pressure waveforms for the different branches in the CW model.

Next, we deployed the devices in the CW model and recorded the pressure waveforms for each specific device deployed across the ICA to the MCA (Pressure waveform figures in **Appendix B**). After isolating the effect of only devices on the pressure, the following **Figure 56** was plotted. This figure illustrates the individual effects of the devices on the pressure reading. In this study, balloon-mesh 3 caused the highest pressure drop at the distal MCA, contrary to the results obtained in the simple model, where the highest pressure drop was observed for balloon-mesh 1. This difference can be attributed to the complexities of the CW model and positioning of the devices at the aneurysm neck. In this model, the aneurysm was intentionally designed on the ICA cavernous to challenge the devices. Consequently, these factors influence the flow behavior and its interaction

with the devices, thus resulting in different outcomes compared to the relatively straightforward conditions of the simple model, where the device faces minimal challenges.

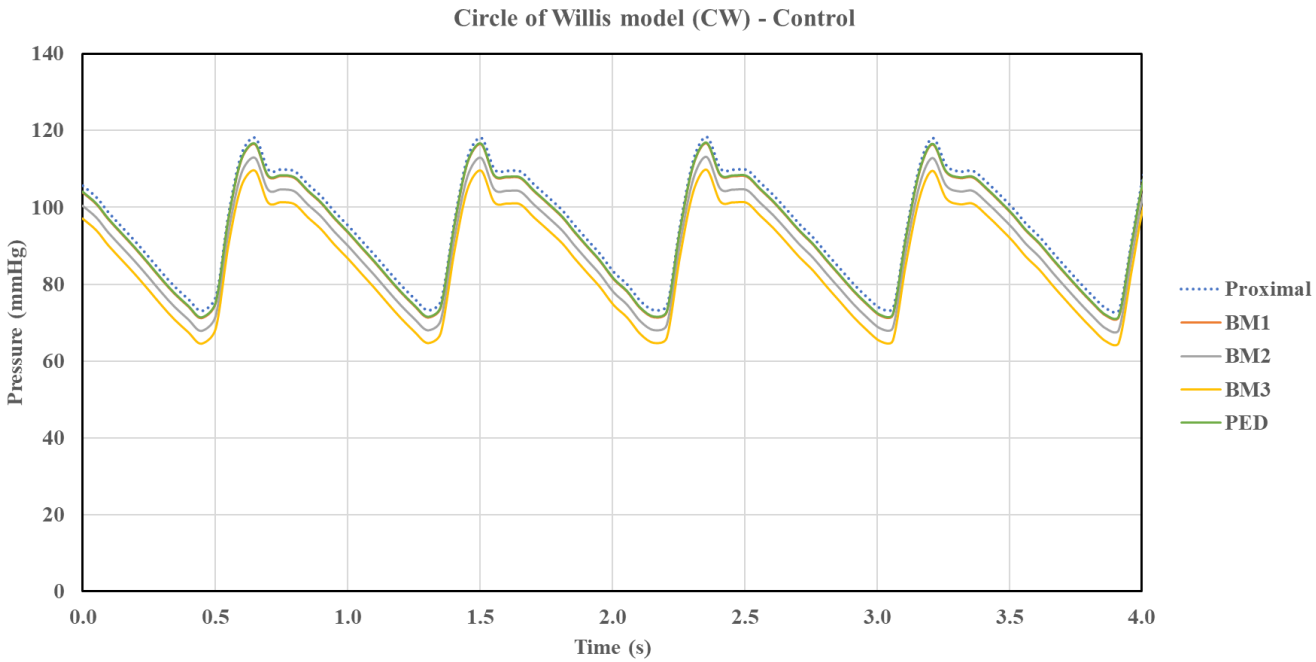

Figure 56: Isolated effect of devices on the proximal pressure in the CW model.

Despite obtaining different outcomes in pressure drop values, the FPR results still remain notably higher than the 0.75 threshold associated with the risk of ischemic stroke in the brain arteries. **Figure 57** shows the FPR results for all devices in the CW model, and the corresponding statistical analysis is available in **Table 9**.

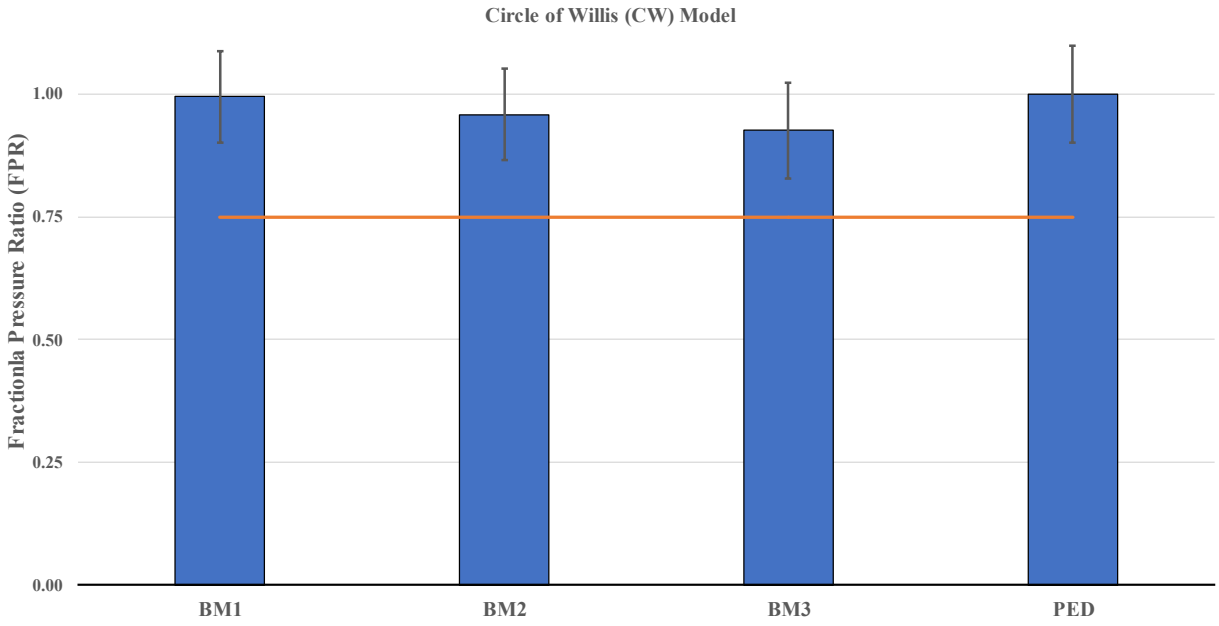

Figure 57: FPR results for all devices in the CW model.

Regarding the pressure drop values, a high standard deviation indicates that the pressure drop values are spread out over a wider range due to pulsatile flow and the complexity of the blood flow pattern in the CW model. However, despite the wide range of deviation, the large sample size and the repeated pattern of pressure waveforms suggest that the sample mean pressure drop is not heavily influenced by random fluctuations or measurement errors. Thus, it provides a robust and accurate estimation of the true average pressure drop in the population. As regards FPR values, the mean values precise and consistent within the dataset (low standard deviation). The error bar (mean ± σ) indicates no significant risk for ischemic stroke caused by using these devices, as the values are well above the ischemia threshold of FPR 0.75.

Table 9: a statistical analysis of pressure drops and FPR of devices in the CW model.

Devices	ΔP		FPR	
	Mean	σ	*Mean*	σ
BM1	1.829	9.250	0.995	0.094
BM2	5.246	9.812	0.959	0.093
BM3	8.658	11.063	0.926	0.098
PED	1.657	9.765	1.000	0.099

Aneurysm Neck Coverage Evaluation

Additionally, aneurysm neck coverage was evaluated through contrast material injections and recorded fluoroscopy videos. The recorded fluoroscopy videos indicate that the control device (PED) failed to reduce the pulsatile flow inside the aneurysm, thereby maintaining a high risk of aneurysm regrowth and rupture in the future, even after completing the treatment. On the other hand, for the balloon-mesh prototypes, it took longer for the contrast agent to fill the entire space of the aneurysms and leave the aneurysm sac. This observation suggests a stagnation of flow with

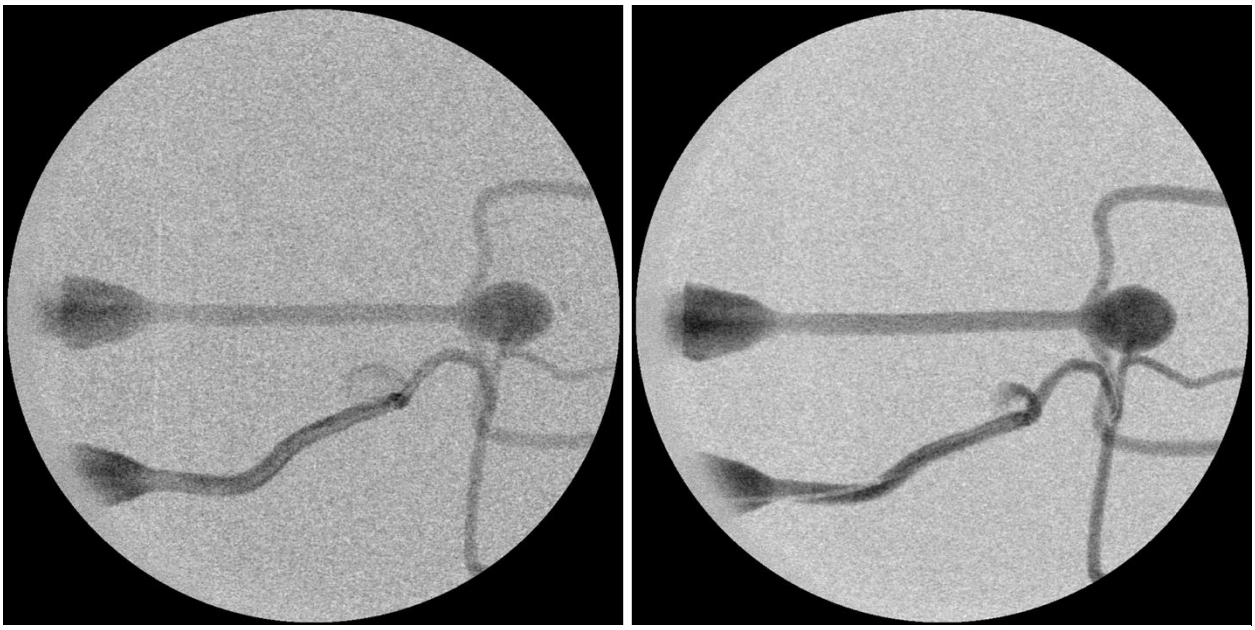

Figure 58: Fluoroscopic images at the same time of contrast injection for BM1 (left) and PED (Right) shows much faster filling of the PED aneurysm vs. the balloon-mesh.

significantly reduced pulsatility inside the aneurysm, facilitating a more consistent filling of the aneurysm with the embolic device and reducing the risk of recanalization in the long term.

We used a semi-quantitative scoring system (ranging from 0 to 3) as detailed in **Table 7**. This system allowed us to assess the ease of tracking, deployment, and retraction of the devices, and also evaluate the aneurysm coverage by considering the intra-aneurysmal flow and flow pulsatility within the aneurysm sac. The balloon-mesh prototypes received lower average scores in all assessments, indicating that controlling and navigating the balloon-mesh prototypes was easier compared to the control. Additionally, the prototypes reduce the pulsatility of flow in the aneurysm sac, and they take longer to fill the sac compared to the control device (**Table 10**).

Table 10: Semi-quantitative scoring of the devices delivery and aneurysm coverage.

Devices	Delivery Scores			Aneurysm Neck Coverage Scores	
	Tracking	Deployment	Retraction	Intra-aneurysmal Flow	Pulsatile Flow
BM 1	1	1	0	1	1
	0	1	1	2	1
	1	1	1	1	0
BM2	2	0	1	1	1
	1	1	1	2	1
	1	1	0	1	1
BM3	1	1	1	1	2
	0	0	1	1	1
	1	1	1	2	0
PED	3	2	3	3	3
	3	2	3	2	3
	3	2	3	3	3
BM Average	0.9	0.8	0.8	1.3	0.9
PED Average	3.0	2.0	3.0	2.7	3.0

Discussion

This study investigates the effectiveness of innovative balloon-mesh prototypes in treating intracranial aneurysms through a comprehensive evaluation process. The research hypothesis, which stated that the prototypes can be successfully tested using a physiologically-relevant benchtop flow model, has been validated through the prototype delivery testing and prototype efficacy testing phases. The prototype delivery testing phase allowed for a detailed assessment of the balloon-mesh prototypes' performance in a simple vessel model. The results indicated that all devices, including the prototypes and the control device (Pipeline Embolization Device - PED), showed minimal impact on pressure drops, thus reducing the risk of ischemic stroke. This finding was supported by the flow pressure ratio (FPR) values, which remained notably higher than the 0.75 threshold associated with the risk of ischemic stroke in brain arteries. These positive outcomes demonstrate the feasibility and potential of using the balloon-mesh prototypes as a promising advancement in endovascular technology for aneurysm treatment.

In the prototype efficacy testing phase, the balloon-mesh prototypes' performance was further evaluated in a more complex *in-vitro* flow model, simulating an endovascular environment using 3D-printed (CW) models. While the pressure drop results in the CW model differed from those in the simple vessel model due to the increased complexity and positioning of the devices at the aneurysm neck, the FPR values remained well above the ischemia threshold, indicating no significant risk for ischemic stroke with the use of these devices. This robust finding reinforces the potential safety and effectiveness of the balloon-mesh prototypes in treating cerebral aneurysms. A key advantage of the balloon-mesh design observed during the prototype efficacy testing was the reduction of pulsatility and stagnation of flow inside the aneurysm. This effect would aid in a more consistent filling of the aneurysm with the embolic device, potentially reducing the risk of

aneurysm regrowth and rupture in the long term. This aspect of the prototypes' performance highlights the potential for enhanced long-term aneurysm treatment outcomes.

Throughout the evaluation process, the balloon-mesh prototypes demonstrated their trackability, ease of deployment, and effective coverage of the aneurysm neck. The fluoroscopy imaging provided crucial insights into the behavior and performance of the devices, supporting their suitability for precise and controlled aneurysm treatment. It is important to note that the current study focused on an *in-vitro* setting, and further research and testing in clinical scenarios will be necessary to establish the full applicability and effectiveness of the balloon-mesh prototypes in real-world medical practice. Additionally, long-term follow-up studies will be essential to assess the durability and stability of the treatment outcomes.

Conclusion

In conclusion, the presented study validates the hypothesis that balloon-mesh prototypes can be effectively assessed using a physiologically-relevant benchtop flow model. The prototype delivery testing and prototype efficacy testing phases demonstrated the feasibility, safety, and potential advantages of the balloon-mesh design for intracranial aneurysm treatment. The balloon-mesh prototypes exhibited favorable performance in terms of pressure drops, FPR values, aneurysm neck coverage, and reduced pulsatility within the aneurysm sac. By offering enhanced aneurysm treatment outcomes and minimizing potential complications, the balloon-mesh prototypes have the potential to significantly contribute to the development of safer and more effective treatment procedures for patients and clinicians dealing with intracranial aneurysms. As the research advances, these innovative prototypes may pave the way for new and improved endovascular technologies, ultimately benefiting patients suffering from this challenging medical condition. However, further research, including clinical trials, will be necessary to confirm and expand on these promising findings.

CHAPTER 5 – CONCLUSIONS

The proposed research study involved the development of a temporary adjunctive medical device - balloon-mesh - for the minimally invasive treatment of intracranial aneurysms using. Most endovascular treatments would benefit from an adjunctive device that isolates the aneurysm sac during deployment of an embolic. Current stent devices allow blood flow through, but are unable to consistently eliminate protrusion, migration, localized vessel trauma, or downstream thrombo-embolic risk from blood platelet activation at the stent surface (requiring long-term patient dual-antiplatelet therapy). Temporary balloons are adept at isolating embolic devices and not requiring antiplatelet therapy, but they also arrest downstream blood flow. Prolonged inflations can increase ischemic risk. Additionally, the practice of balloon inflation and deflation, to avoid ischemia, can result in diffuse vessel trauma. The proposed balloon-mesh device effectively combines the advantages of both balloons and stents while reducing their respective drawbacks. This innovative solution not only provides a protective surface at the neck of the aneurysm but also ensures adequate downstream blood flow, thereby minimizing the risk of ischemia.

In Chapter 2, we investigated the relationship between flow rates, device sizes, and ischemic risk, with a focus on the flow pressure ratio (FPR) as an indicator of the risk of ischemic stroke. The combination of theoretical estimations, computational fluid dynamics (CFD) simulations, and bench-top testing creates a comprehensive view on the impact of narrowing blood vessels on flow rates and pressure drops. While acknowledging the limitations of idealized models, the chapter demonstrates the reliability of both CFD simulations and bench-top testing in assessing FPR and ischemic risk, validating the use of these methods in further research and clinical applications.

In Chapter 3, the mechanical integrity of the balloon-mesh prototypes is explored through radial force and tracking force studies. The comparison with FDA-approved control devices reveals the prototypes suitability for practical applications. The analysis of radial forces and tracking forces emphasizes the importance of differentiating between permanent and temporary devices. The chapter emphasizes the prototypes potential to serve as a promising adjunctive tool for endovascular treatments, particularly given their ease of deployment and trackability. The examination of force requirements within the catheter and model provides crucial insights for optimizing the prototypes' design for efficient navigation through complex vascular anatomy.

Chapter 4 concludes the evaluation of the prototypes effectiveness in treating intracranial aneurysms. The two-phased assessment provides a robust foundation for considering the prototypes potential clinical impact. The prototypes ability to minimize pressure drops and maintain FPR values above the ischemic risk threshold is a promising indication of their safety. Notably, the prototypes capability to reduce pulsatility within aneurysms indicated a positive reason for enhancing long-term treatment outcomes.

To sum up, this research provides a complete view of the innovative balloon-mesh prototypes potential as an advancement in endovascular technology for intracranial aneurysm treatment. The combined use of theoretical modeling, computational simulations, bench-top testing, and *in-vitro* evaluations creates a robust foundation for further research and clinical translation. The data generated from this translational research has the potential to guide the production of ultimate balloon-mesh prototypes, along with subsequent mechanical and biocompatibility assessments, all preceding the FDA approval process. This proposed project could lead to a significant improvement of treatment effectiveness for severe neurovascular aneurysms by combining the fields of bioengineering and neurointerventional surgery.

Future Work

During the FDA submission process for the balloon-mesh, the journey involves utilizing the current data to refine the prototypes. Once the optimal prototypes are achieved, the design will be frozen. A comprehensive series of mechanical tests will be conducted, followed by Biocompatibility studies performed in conjunction with NAMSA, a Contract Research Organization (CRO) specializing in medical devices. These studies will follow the standards of Good Laboratory Practices (GLP) as well as the International Standard ISO 10993 when necessary. Subsequently, animal studies will be conducted using canine models to assess the device's effectiveness and efficacy. The findings will be presented in an Investigational Device Exemption (IDE) meeting with the FDA to decide the device classification.

REFRENCES

1. Brisman JL, Song JK, Newell DW. Medical Progress Cerebral Aneurysms. 2006. www.nejm.org. Accessed September 29, 2021.
2. Hackenberg KAM, Etminan N. *Neurovascular Disease, Diagnosis, and Therapy: Brain Aneurysms*. Vol 176. 1st ed. Elsevier B.V.; 2021. doi:10.1016/B978-0-444-64034-5.00001-8
3. Savastano LE, Bhambri A, Andrew D, Pandey AS. *Chapter 2 - Biology of Cerebral Aneurysm Formation, Growth, and Rupture*. Elsevier Inc.; 2018. doi:10.1016/B978-0-12-811740-8.00002-2
4. Etminan N, Rinkel GJ. Unruptured intracranial aneurysms: Development, rupture and preventive management. *Nat Rev Neurol*. 2016;12(12):699-713. doi:10.1038/nrneurol.2016.150
5. Ascending and Arch Aortic Aneurysms and Dissection | BCM. https://www.bcm.edu/healthcare/specialties/cardiovascular-medicine/cardiothoracic-surgery/ascending-and-arch-aortic-aneurysms-and-dissection. Accessed October 13, 2021.
6. Brain Aneurysms - Neurosurgery. https://neurosurgery.wustl.edu/items/aneurysms/. Accessed October 13, 2021.
7. Statistics and Facts - Brain Aneurysm Foundation. https://bafound.org/about-brain-aneurysms/brain-aneurysm-basics/brain-aneurysm-statistics-and-facts/. Accessed December 2, 2019.
8. SHELDEN CH, PUDENZ RH, BRANNON LE. Intracranial aneurysms. *Arch Surg*. 1950;61(2):294-304. doi:10.1001/archsurg.1950.01250020298011
9. Diaz O, Rangel-Castilla L. *Endovascular Treatment of Intracranial Aneurysms*. Vol 136.

1st ed. Elsevier B.V.; 2016. doi:10.1016/B978-0-444-53486-6.00067-3

10. Merritt W, Berns H, Ducruet AF, Becker TA. Definitions of Intracranial Aneurysm Size and Morphology: A Call for Standardization. *Surg Neurol Int*. 2021;Manuscript(506):1-7. doi:10.25259/SNI

11. The Circle of Willes in Cryonics Perfusion - Biostasis. https://www.biostasis.com/the-circle-of-willes-in-cryonics-perfusion/. Accessed October 5, 2021.

12. Palma A, Galarza-paez L, Fargen KM, Singh J, Wilson JA, Wolfe SQ. *Specifics of Aneurysm Treatment Distal Aneurysms*. Elsevier Inc.; 2018. doi:10.1016/B978-0-12-811740-8.00035-6

13. Graaf V Der, Williams L. Aneurysms , Intracranial. 1997:660-664.

14. Lodi YM, Thomas JG, Fessler RD. Dissecting Intracranial Aneurysms. 2018:629-643. doi:10.1016/B978-0-12-811740-8.00059-9

15. HUTTON CF. Subarachnoid haemorrhage. *Br J Radiol*. 1954;27(320):471-472. doi:10.1259/0007-1285-27-320-471

16. Subarachnoid Hemorrhage Symptoms & Treatment | Pacific Stroke & Neurovascular Center. https://www.pacificneuroscienceinstitute.org/stroke-neurovascular/conditions-and-treatments/stroke/hemorrhagic-stroke/subarachnoid/. Accessed October 6, 2021.

17. Morton RP, Kelly CM, Levitt MR. *Endovascular Treatment of Intracranial Aneurysms*. Seventh Ed. Elsevier Inc.; 2018. doi:10.1016/B978-0-323-43140-8.00024-X

18. Dandy WE. INTRACRANIAL ANEURYSM OF THE INTERNAL CAROTID ARTERY: CURED BY OPERATION. *Ann Surg*. 1938;107(5):654-659. doi:10.1097/00000658-193805000-00003

19. Caplan JM, Naval N, Huang J, Tamargo RJ. *Aneurysm Surgery*. Elsevier Inc.; 2018.

doi:10.1016/B978-0-323-32106-8.00009-1

20. Ross IB, Dhillon GS. Complications of endovascular treatment of cerebral aneurysms. *Surg Neurol*. 2005;64(1):12-18. doi:10.1016/j.surneu.2004.09.045

21. Cognard C, Pierot L, Boulin A, et al. Intracranial aneurysms: Endovascular treatment with mechanical detachable spirals in 60 aneurysms. *Radiology*. 1997. doi:10.1148/radiology.202.3.9051034

22. Cognard C, Weill A, Castaings L, Rey A, Moret J. Intracranial berry aneurysms: angiographic and clinical results after endovascular treatment. *Radiology*. 1998;206(2):499-510. doi:10.1148/radiology.206.2.9457205

23. Zhu Y, Zhang H, Zhang Y, et al. Endovascular metal devices for the treatment of cerebrovascular diseases. *Adv Mater*. 2019;31(8):1805452.

24. Li W, Tian Z, Zhu W, et al. Hemodynamic Analysis of Postoperative Rupture of Unruptured Intracranial Aneurysms after Placement of Flow-Diverting Stents: A Matched Case-Control Study. *Am J Neuroradiol*. 2019;(2016). doi:10.3174/ajnr.a6256

25. Madaelil TP, Moran CJ, Cross DT, Kansagra AP. Flow diversion in ruptured intracranial aneurysms: A meta-analysis. *Am J Neuroradiol*. 2017;38(3):590-595. doi:10.3174/ajnr.A5030

26. Brinjikji W, Piano M, Fang S, et al. Treatment of ruptured complex and large/giant ruptured cerebral aneurysms by acute coiling followed by staged flow diversion. *J Neurosurg*. 2016;125(1):120-127.

27. Wakhloo A, Lylyk P, De Vries J, et al. O-008 A New Generation of Flow Diverters for Endovascular Treatment of Intracranial Aneurysms-A Multicentre Preliminary Clinical and Angiographic Experience in 161 patients with 186 Aneurysms. *J Neurointerv Surg*.

2013;5(Suppl 2):A5-A6.

28. Piotin M, Blanc R. Balloons and stents in the endovascular treatment of cerebral aneurysms: Vascular anatomy remodeled. *Front Neurol*. 2014. doi:10.3389/fneur.2014.00041

29. Gounis M, Patel N, Norbash A, et al. O-009 Cone beam CT of cerebrovascular stents. *J Neurointerv Surg*. 2010;2(Suppl 1):A4-A5.

30. Jeon P, Kim BM, Kim DJ, Kim DIK, Park KY. Y-configuration double-stent-assisted coiling using two closed-cell stents for wide-neck basilar tip aneurysms. *Acta Neurochir (Wien)*. 2014. doi:10.1007/s00701-014-2163-0

31. Kim Y-J, Ko JHO. Sole stenting with large cell stents for very small ruptured intracranial aneurysms. *Interv Neuroradiol*. 2014;20(1):45-53.

32. Cho YD, Lee WJ, Kim KM, Kang HS, Kim JE, Han MH. Stent-assisted coil embolization of posterior communicating artery aneurysms. *Am J Neuroradiol*. 2013. doi:10.3174/ajnr.A3541

33. Gerbay A, Terreaux J, Cerisier A, Vola M, Isaaz K. Impact of very high pressure stent deployment on angiographic and long-term clinical outcomes in true coronary bifurcation lesions treated by the mini-crush stent technique: A single center experience. *Indian Heart J*. 2017. doi:10.1016/j.ihj.2016.05.013

34. Tateshima S, Jones JG, Basto FM, Vinuela F, Duckwiler GR. Aneurysm pressure measurement before and after placement of a Pipeline stent: Feasibility study using a 0.014 inch pressure wire for coronary intervention. *J Neurointerv Surg*. 2016. doi:10.1136/neurintsurg-2014-011214

35. Klisch J, Sychra V, Strasilla C, Liebig T, Fiorella D. The Woven EndoBridge cerebral

aneurysm embolization device (WEB II): initial clinical experience. *Neuroradiology*. 2011;53(8):599-607. doi:10.1007/s00234-011-0891-x

36. Ozpeynirci Y, Braun M, Schmitz B. CT Angiography in Occlusion Assessment of Intracranial Aneurysms Treated with the WEB Device. *J Neuroimaging*. 2019. doi:10.1111/jon.12622

37. Fiorella D, Arthur A, Byrne J, et al. Interobserver variability in the assessment of aneurysm occlusion with the WEB aneurysm embolization system. *J Neurointerv Surg*. 2015. doi:10.1136/neurintsurg-2014-011251

38. Caroff J, Mihalea C, Ikka L, Moret J, Spelle L. Interobserver variability in the assessment of aneurysm occlusion with the WEB aneurysm embolisation system. *J Neurointerv Surg*. 2017. doi:10.1136/neurintsurg-2015-011862

39. Kabbasch C, Goertz L, Siebert E, et al. Factors that determine aneurysm occlusion after embolization with the Woven EndoBridge (WEB). *J Neurointerv Surg*. 2019. doi:10.1136/neurintsurg-2018-014361

40. Ding YH, Lewis DA, Kadirvel R, Dai D, Kallmes DF. The woven endobridge: A new aneurysm occlusion device. *Am J Neuroradiol*. 2011. doi:10.3174/ajnr.A2399

41. Piotin M, Biondi A, Sourour N, et al. O-025 the luna aneurysm embolization system: immediate and 12 month follow-up of the european pmcf study: Abstract O-025 Table 1. *J Neurointerv Surg*. 2015. doi:10.1136/neurintsurg-2015-011917.25

42. Ding YH, Dai D, Schroeder D, Kadirvel R, Kallmes DF. Experimental testing of the dual-layer Woven EndoBridge device using an elastase-induced aneurysm model in rabbits. In: *Interventional Neuroradiology*. ; 2016. doi:10.1177/1591019916628202

43. White AC, Khattar NK, Aljuboori ZS, Obiora JC, James RF. Chapter 21 - Basic

Endovascular Techniques: Direct, Balloon-Assisted, and Stent-Assisted Coil Embolization. In: Ringer AJBT-IA, ed. Academic Press; 2018:329-356. doi:https://doi.org/10.1016/B978-0-12-811740-8.00023-X

44. Pierot L, Wakhloo AK. Endovascular treatment of intracranial aneurysms: Current status. *Stroke*. 2013;44(7):2046-2054. doi:10.1161/STROKEAHA.113.000733

45. Lazareska M, Aliji V, Stojovska-jovanovska E, Businovska J, Mircevski V. Endovascular Treatment of Wide Neck Aneurysms. 2018;6(12):2316-2322.

46. WEB™ SL & WEB™ SLS | Microvention. https://www.microvention.com/product/web-family. Accessed October 20, 2021.

47. Woven EndoBridge (WEB) Intrasaccular Therapy for Treatment of Wide Neck Bifurcation Intracranial Aneurysms. 2018:1-109. https://www.fda.gov/media/123225/download.

48. Tevah J, Senf R, Cruz J, Fava M. Endovascular treatment of complex cerebral aneurysms with Onyx hd-500® in 38 patients. *J Neuroradiol*. 2011;38(5):283-290.

49. Cekirge HS, Saatci I, Ozturk MH, et al. Late angiographic and clinical follow-up results of 100 consecutive aneurysms treated with Onyx reconstruction: Largest single-center experience. *Neuroradiology*. 2006. doi:10.1007/s00234-005-0007-6

50. Ayad M, Eskioglu E, Mericle RA. Onyx®: A unique neuroembolic agent. *Expert Rev Med Devices*. 2006. doi:10.1586/17434440.3.6.705

51. Preiß H. A contribution to the controversy over dimethyl sulfoxide toxicity: Anesthesia monitoring results in patients treated with Onyx embolization for intracranial aneurysms [1]. *Neuroradiology*. 2006. doi:10.1007/s00234-005-0028-1

52. Struffert T, Roth C, Romeike B, Grunwald IO, Reith W. Onyx in an experimental

aneurysm model: Histological and angiographic results: Laboratory investigation. *J Neurosurg*. 2008. doi:10.3171/JNS/2008/109/7/0077

53. Pamuk AG, Saatci I, Cekirge HS, Aypar U. A contribution to the controversy over dimethyl sulfoxide toxicity: Anesthesia monitoring results in patients treated with Onyx embolization for intracranial aneurysms. *Neuroradiology*. 2005. doi:10.1007/s00234-004-1323-y

54. Piske RL, Kanashiro LH, Paschoal E, Agner C, Lima SS, Aguiar PH. Evaluation of onyx hd-500 embolic system in the treatment of 84 wide-neck intracranial aneurysms. In: *Neurosurgery*. ; 2009. doi:10.1227/01.NEU.0000340977.68347.51

55. Song DL, Leng B, Zhou LF, Gu YX, Chen XC. Onyx in treatment of large and giant cerebral aneurysms and arteriovenous malformations. *Chin Med J (Engl)*. 2004.

56. Molyneux AJ, Cekirge S, Saatci I, Gál G. Cerebral Aneurysm Multicenter European Onyx (CAMEO) Trial: Results of a Prospective Observational Study in 20 European Centers. *Am J Neuroradiol*. 2004.

57. Cekirge HS, Saatci I, Geyik S, Yavuz K, Öztürk H, Pamuk G. Intrasaccular combination of metallic coils and Onyx liquid embolic agent for the endovascular treatment of cerebral aneurysms. *J Neurosurg*. 2006. doi:10.3171/jns.2006.105.5.706

58. Wu Y, Huang Q, Yang P, Zhang L, Li Q, Liu J. Onyx combined with coiling embolization for endovascular treatment of complex intracranial ruptured aneurysms. *J Interv Radiol*. 2011;20(4):261-264.

59. Linfante I, Wakhloo AK. Brain aneurysms and arteriovenous malformations: Advancements and emerging treatments in endovascular embolization. *Stroke*. 2007. doi:10.1161/01.STR.0000259824.10732.bb

60. Berenstein A, Song JK, Tsumoto T, Namba K, Niimi Y. Treatment of experimental aneurysms with an embolic-containing device and liquid embolic agent: Feasibility and angiographic and histological results. *Neurosurgery*. 2009;64(2):367-373. doi:10.1227/01.NEU.0000335790.91413.64

61. Berenstein A. Treatment of experimental aneurysms with a new liquid embolic agent and a retrievable stent: Proof of concept and feasibility study. *J Neurointerv Surg*. 2016;8(9):934-939. doi:10.1136/neurintsurg-2015-011930

62. G. A, M. S, O. P, A. B, D. K. Celiomesenteric aneurysms related to local high-flow conditions: Combined approach with small-caliber stent graft. *J Vasc Interv Radiol*. 2014. doi:10.1016/j.jvir.2014.03.001

63. Brennecka C, Preul M, Becker T, Vernon B. In vivo embolization of lateral wall aneurysms in canines using the liquid-to-solid gelling PPODA-QT polymer system: 6-month pilot study. *J Neurosurg*. 2013;119(1):228-238. doi:10.3171/2013.3.JNS121865

64. Takigawa T, Suzuki K, Sugiura Y, et al. Thromboembolic events associated with single balloon-, double balloon-, and stent-assisted coil embolization of asymptomatic unruptured cerebral aneurysms: evaluation with diffusion-weighted MR imaging. doi:10.1007/s00234-014-1421-4

65. Rahme R, Grande A, Jimenez L, Abruzzo TA, Ringer AJ. Onyx HD-500 embolization of intracranial aneurysms: Modified technique using continuous balloon inflation under conscious sedation. *J Clin Neurosci*. 2014;21(8):1383-1387. doi:10.1016/J.JOCN.2014.01.004

66. Fischer S, Weber A, Carolus A, Drescher F, Götz F, Weber W. Coiling of wide-necked carotid artery aneurysms assisted by a temporary bridging device (Comaneci): preliminary

experience. doi:10.1136/neurintsurg-2016-012664

67. Sirakov A, Minkin K, Penkov M, Ninov K, Karakostov V, Sirakov S. Comaneci-Assisted Coiling as a Treatment Option for Acutely Ruptured Wide Neck Cerebral Aneurysm: Case Series of 118 Patients. *Neurosurgery*. 2020;0(0):1-9. doi:10.1093/neuros/nyaa200

68. He R, Zhao L, Silberschmidt V V. Mechanical performance of self-expandable nitinol stent with lesion-specific design. *Procedia Struct Integr*. 2019;15:24-27. doi:10.1016/j.prostr.2019.07.005

69. Chen PR, Ortiz R, Page JH, Siddiqui AH, Veznedaroglu E, Rosenwasser RH. SPONTANEOUS SYSTOLIC BLOOD PRESSURE ELEVATION DURING TEMPORARY BALLOON OCCLUSION INCREASES THE RISK OF ISCHEMIC EVENTS AFTER CAROTID ARTERY OCCLUSION. *Neurosurgery*. 2008;63(2):256-265. doi:10.1227/01.NEU.0000320443.15090.C1

70. Brennecka CR, Preul MC, Bichard WD, Vernon BL. In vivo experimental aneurysm embolization in a swine model with a liquid-to-solid gelling polymer system: Initial biocompatibility and delivery strategy analysis. *World Neurosurg*. 2012. doi:10.1016/j.wneu.2011.10.029

71. Thompson JW, Elwardany O, McCarthy DJ, et al. In vivo cerebral aneurysm models. *Neurosurg Focus*. 2019;47(1):1-8. doi:10.3171/2019.4.FOCUS19219

72. Herting SM, Ding Y, Boyle AJ, et al. In vivo comparison of shape memory polymer foam-coated and bare metal coils for aneurysm occlusion in the rabbit elastase model. *J Biomed Mater Res - Part B Appl Biomater*. 2019;107(8):2466-2475. doi:10.1002/jbm.b.34337

73. Asgari O, Berns H, Arzani A, Becker T. O-006 Prototyping a balloon stent for minimally

invasive temporary aneurysm occlusion and embolization. In: *Oral Abstracts*. BMA House, Tavistock Square, London, WC1H 9JR: BMJ Publishing Group Ltd.; 2021:A3.2-A4. doi:10.1136/neurintsurg-2021-SNIS.6

74. Asgari O, Sodawalla H, Becker T. E-228 A novel stent-balloon device for treatment of sidewall intracranial aneurysms. In: *Electronic Poster Abstracts*. BMA House, Tavistock Square, London, WC1H 9JR: BMJ Publishing Group Ltd.; 2020:A153.2-A154. doi:10.1136/neurintsurg-2020-SNIS.259

75. Asgari O, Fennell B, Norris N, Ducruet A, Becker T. P-013 Designing and prototyping a novel balloon-stent device for minimally invasive temporary aneurysm occlusion and embolization. In: *SNIS 19th Annual Meeting Oral Poster Abstracts*. BMA House, Tavistock Square, London, WC1H 9JR: BMJ Publishing Group Ltd.; 2022:A56-A57. doi:10.1136/neurintsurg-2022-SNIS.85

76. Asgari O, Wells J, Fisher C, Becker T, Ducruet A. E-264 A novel temporary balloon-stent device for adjunctive aneurysm protection during embolization. In: *SNIS 20th Annual Meeting Electronic Poster Abstracts*. BMA House, Tavistock Square, London, WC1H 9JR: BMJ Publishing Group Ltd.; 2023:A236.1-A236. doi:10.1136/jnis-2023-SNIS.363

77. Pijls NHJ, Van Gelder B, Van Der Voort P, et al. Fractional flow reserve: A useful index to evaluate the influence of an epicardial coronary stenosis on myocardial blood flow. *Circulation*. 1995;92(11):3183-3193. doi:10.1161/01.CIR.92.11.3183/FORMAT/EPUB

78. Liu J, Yan Z, Pu Y, et al. Functional assessment of cerebral artery stenosis: A pilot study based on computational fluid dynamics. *J Cereb Blood Flow Metab*. 2017;37(7):2567-2576. doi:10.1177/0271678X16671321

79. Pu Y, Lan L, Leng X, Wong LKS, Liu L. Intracranial atherosclerosis: From anatomy to

pathophysiology. *Int J Stroke*. 2017;12(3):236-245. doi:10.1177/1747493016685716

80. Lee KE, Ryu AJ, Shin ES, Shim EB. Physiome approach for the analysis of vascular flow reserve in the heart and brain. *Pflugers Arch Eur J Physiol*. 2017;469(5-6):613-628. doi:10.1007/s00424-017-1961-7

81. Feske SK. Ischemic Stroke. *Am J Med*. 2021;134(12):1457-1464. doi:10.1016/J.AMJMED.2021.07.027

82. Dare AO, Chaloupka JC, Putman CM, Fayad PB, Awad IA. Failure of the hypotensive provocative test during temporary balloon test occlusion of the internal carotid artery to predict delayed hemodynamic ischemia after therapeutic carotid occlusion. *Surg Neurol*. 1998;50(2):147-156. doi:10.1016/S0090-3019(97)00444-8

83. Blanco PJ, Müller LO, Spence JD. Blood pressure gradients in cerebral arteries: A clue to pathogenesis of cerebral small vessel disease. *Stroke Vasc Neurol*. 2017. doi:10.1136/svn-2017-000087

84. Updegrove A, Wilson NM, Merkow J, Lan H, Marsden AL, Shadden SC. SimVascular: An Open Source Pipeline for Cardiovascular Simulation. *Ann Biomed Eng*. 2017;45(3):525-541. doi:10.1007/S10439-016-1762-8/FIGURES/14

85. Norris NG, Merritt WC, Becker TA. Application of nondestructive mechanical characterization testing for creating in vitro vessel models with material properties similar to human neurovasculature. *J Biomed Mater Res Part A*. 2021;(September):1-11. doi:10.1002/jbm.a.37314

86. Lidington D, Wan H, Bolz SS. Cerebral Autoregulation in Subarachnoid Hemorrhage. *Front Neurol*. 2021;12:1229. doi:10.3389/FNEUR.2021.688362/BIBTEX

87. Rai AT, Hogg JP, Cline B, Hobbs G. Cerebrovascular geometry in the anterior circulation:

An analysis of diameter, length and the vessel taper. *J Neurointerv Surg*. 2013;5(4):371-375. doi:10.1136/neurintsurg-2012-010314

Appendix A

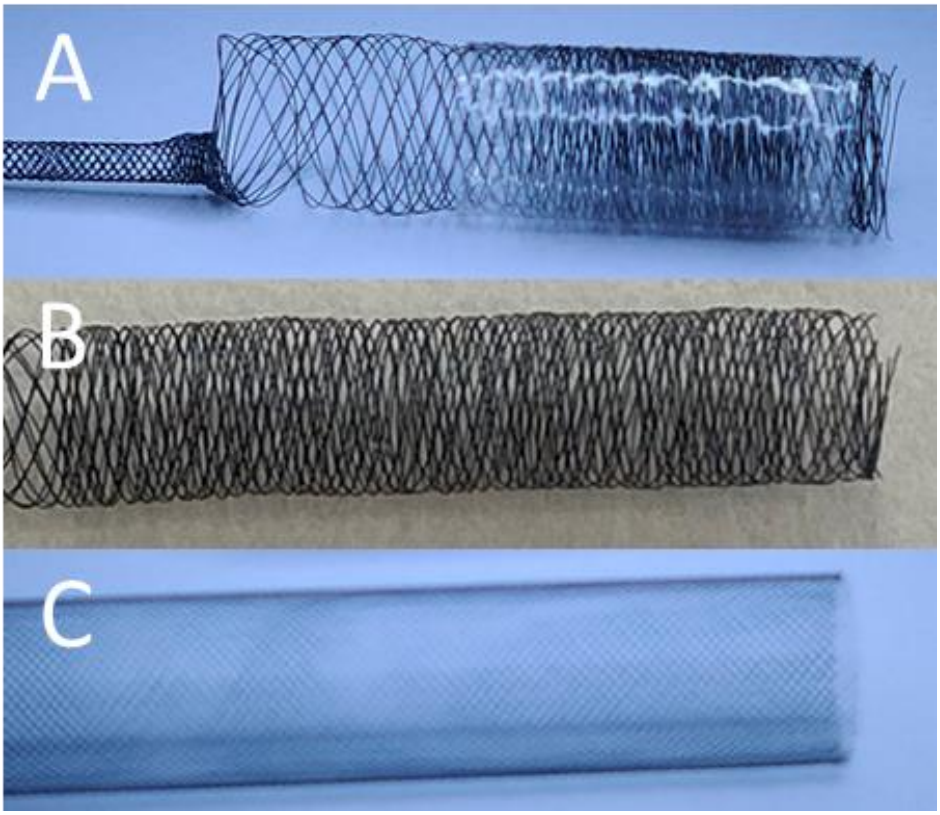

Figure 59: Initial balloon-mesh prototype builds: A) urethane coating, B) without coating, C) fine mesh - 100μm pores.

Radial Force Study

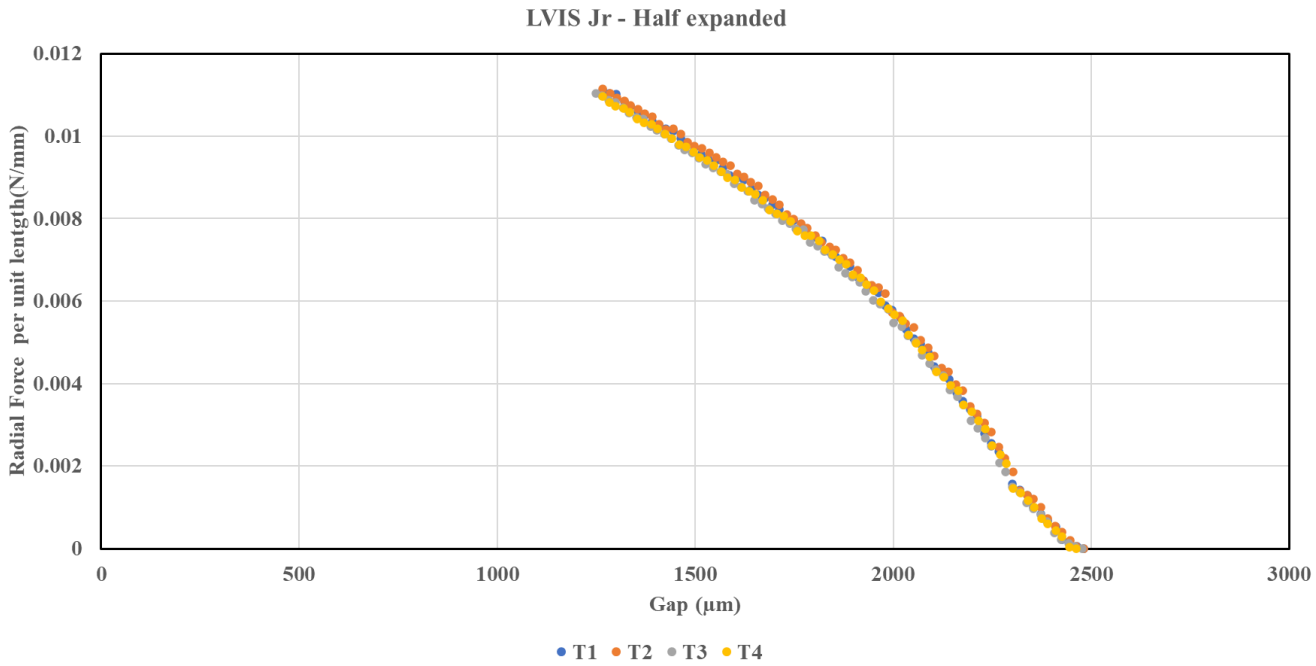

Figure 60: Radial force per unit length with respect to gap (OD of the device) for LVIS Jr – half expanded.

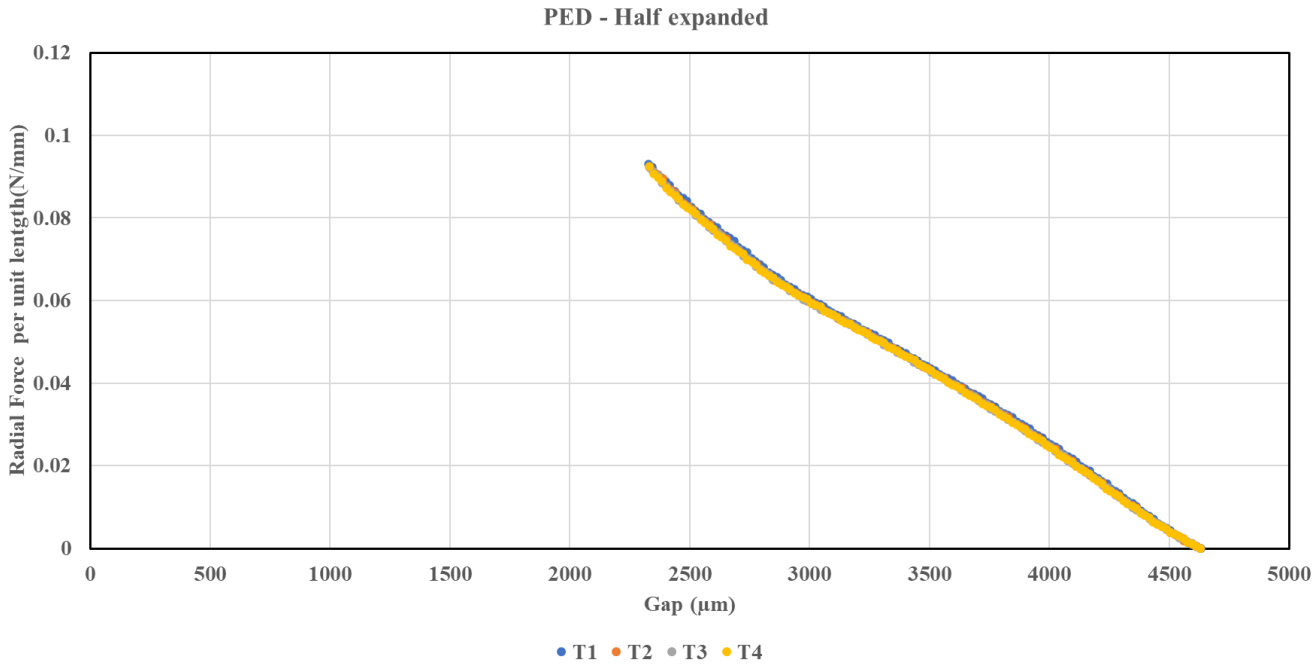

Figure 61: Radial force per unit length with respect to gap (OD of the device) for PED – half expanded.

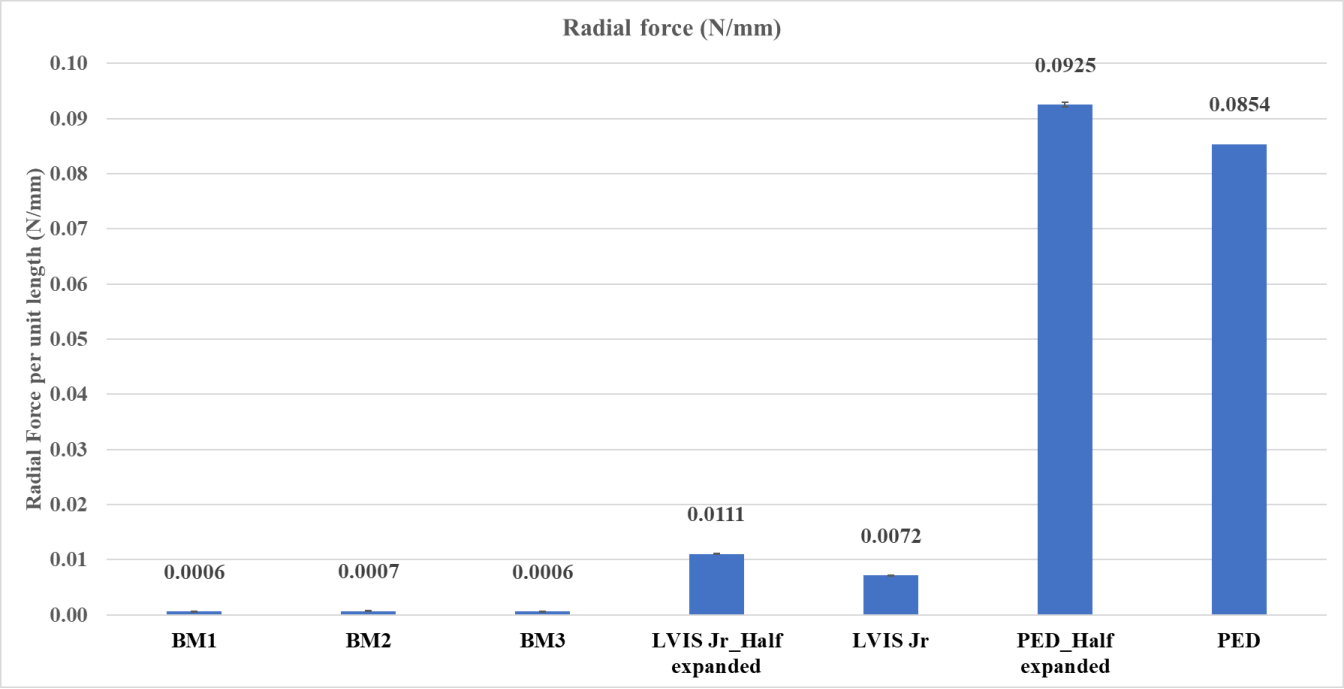

Figure 62: Radial force per unit length at 50% compression for all devices.

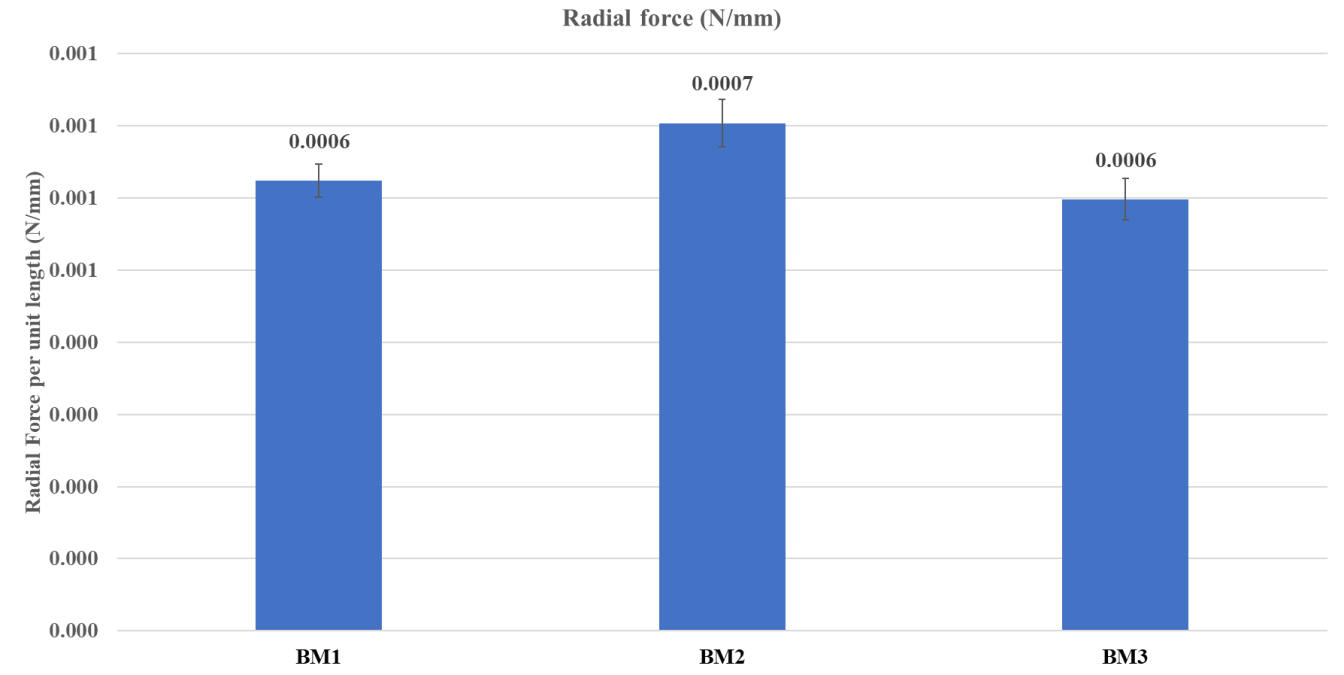

Figure 63: Radial force per unit length at 50% compression for balloon-mesh prototypes.

Tracking Force Study

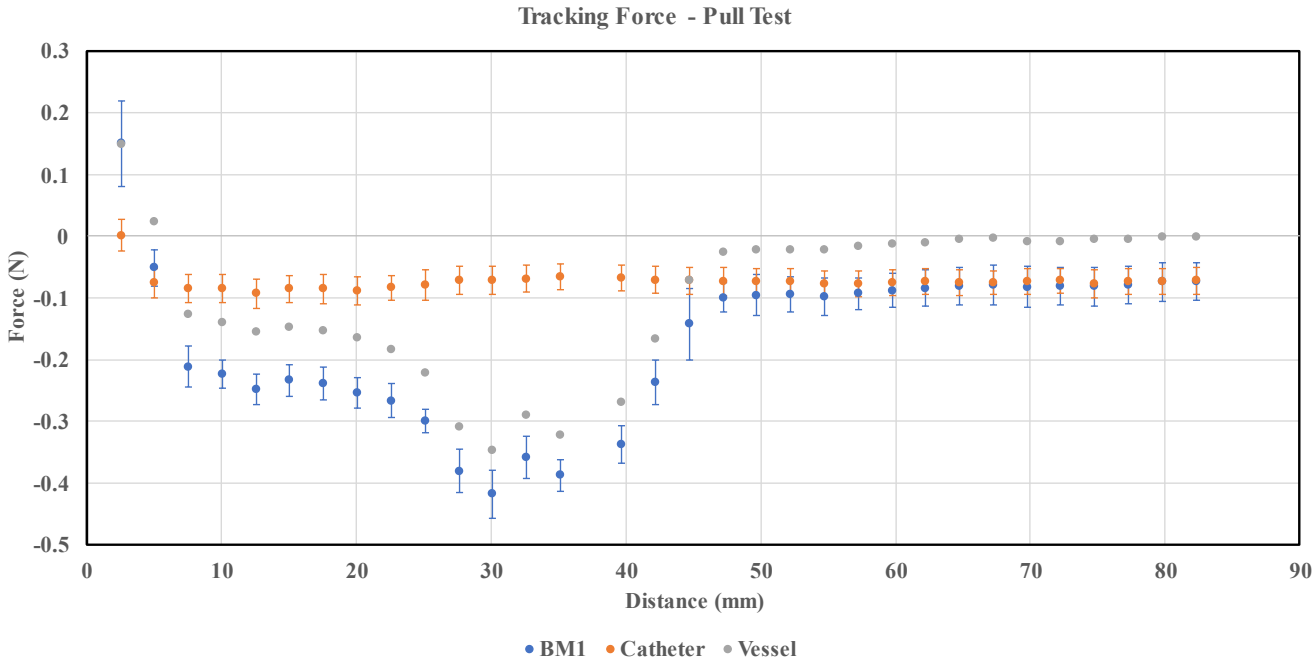

Figure 64: Tracking force to pull BM1 into the CW model. Blue: total force with device and vessel tortuosity friction, orange: vessel tortuosity friction, and gray: vessel tortuosity friction alone.

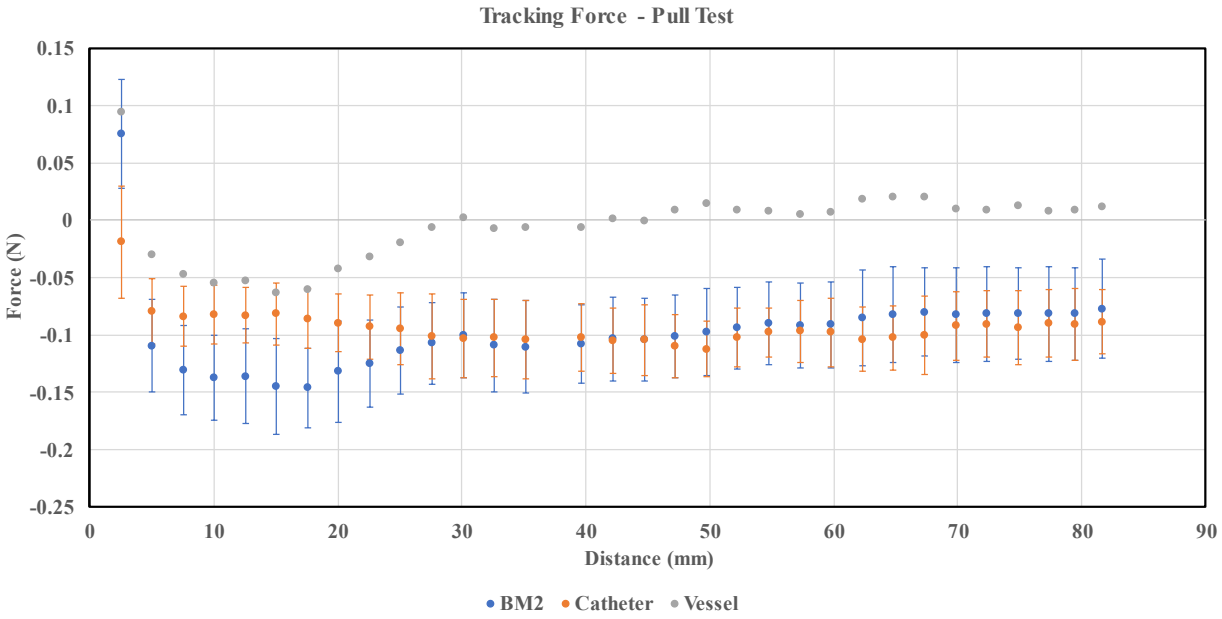

Figure 65: Tracking force to pull BM1 into the CW model. Blue: total force with device and vessel tortuosity friction, orange: vessel tortuosity friction, and gray: vessel tortuosity friction alone.

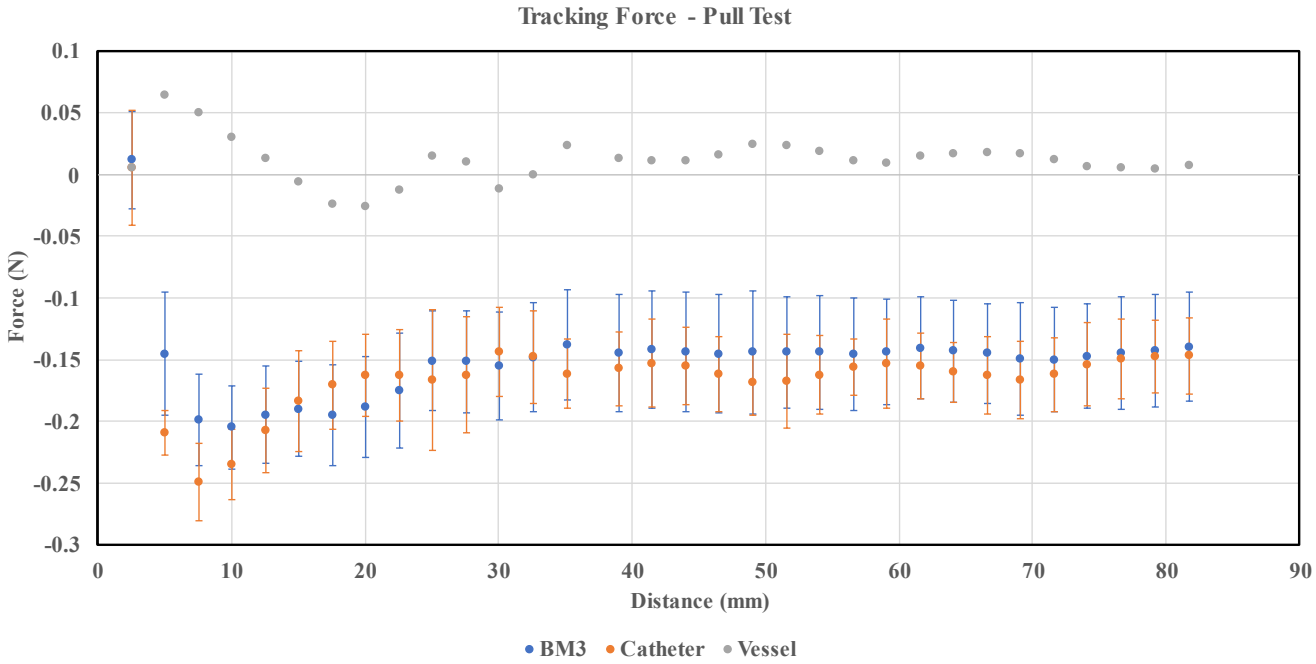

Figure 66: Tracking force to pull BM3 into the CW model. Blue: total force with device and vessel tortuosity friction, orange: vessel tortuosity friction, and gray: vessel tortuosity friction alone.

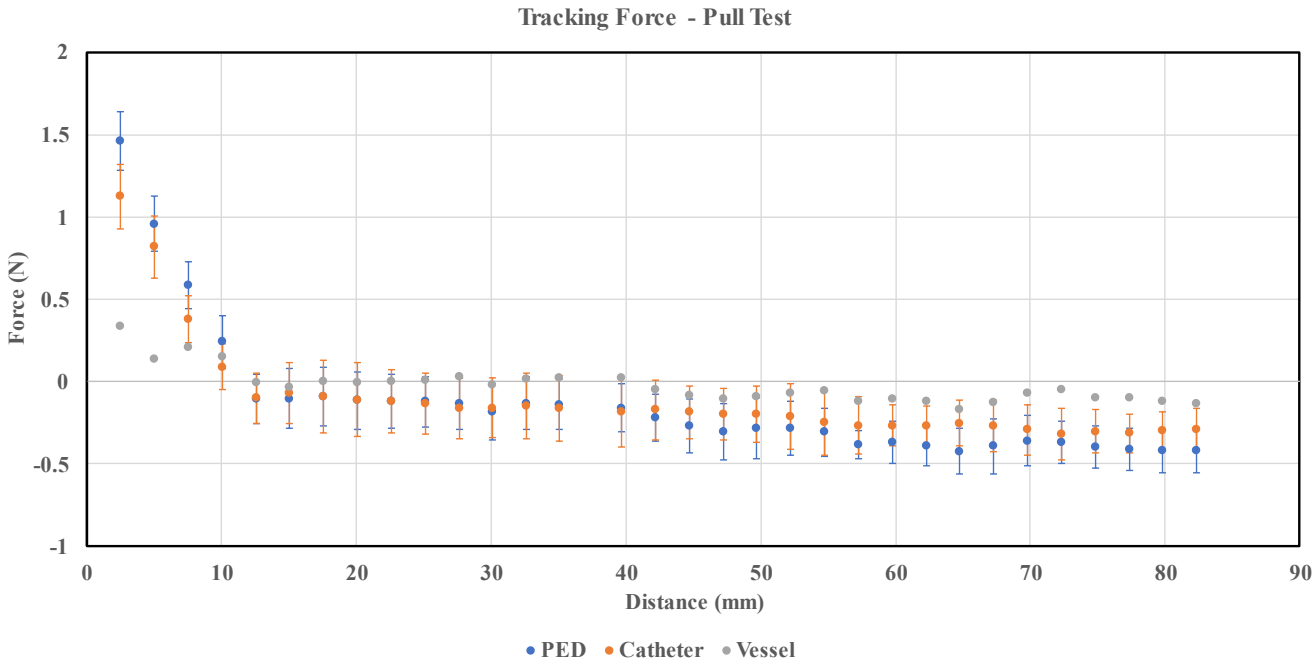

Figure 67: Tracking force to pull PED into the CW model. Blue: total force with device and vessel tortuosity friction, orange: vessel tortuosity friction, and gray: vessel tortuosity friction alone.

Appendix B

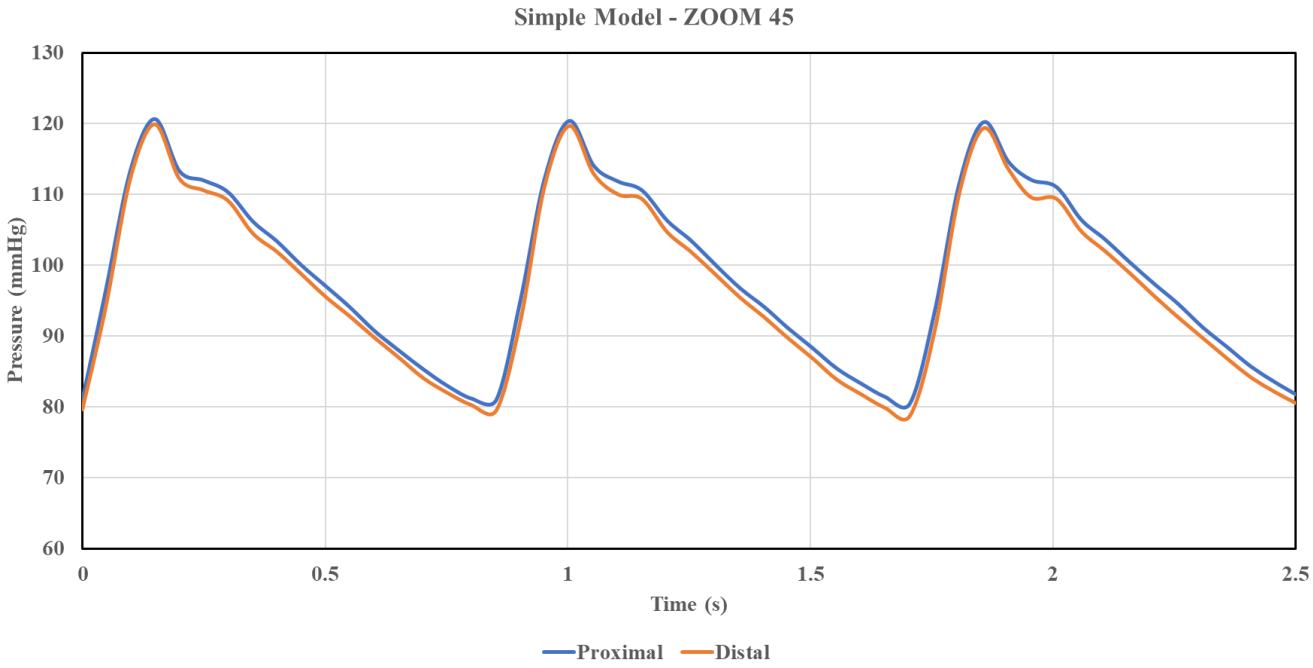

Figure 68: Proximal and distal pressures of the simple model with delivery catheter.

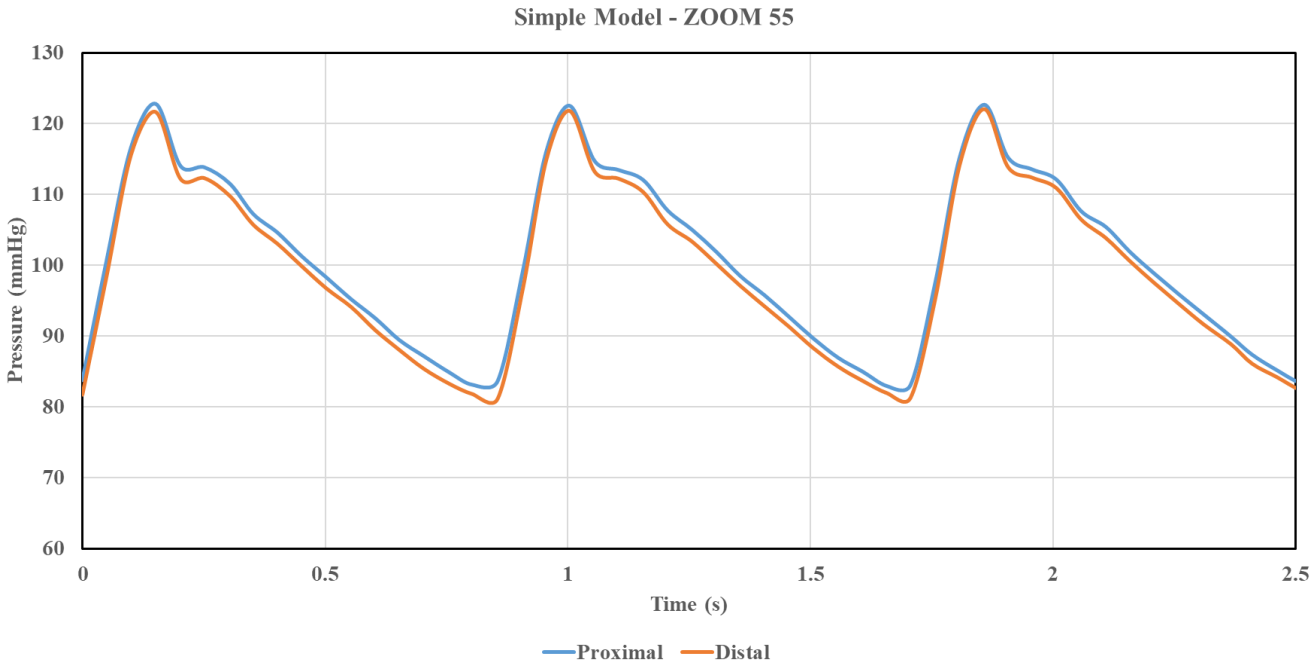

Figure 69: Proximal and distal pressures of the simple model with delivery catheter.

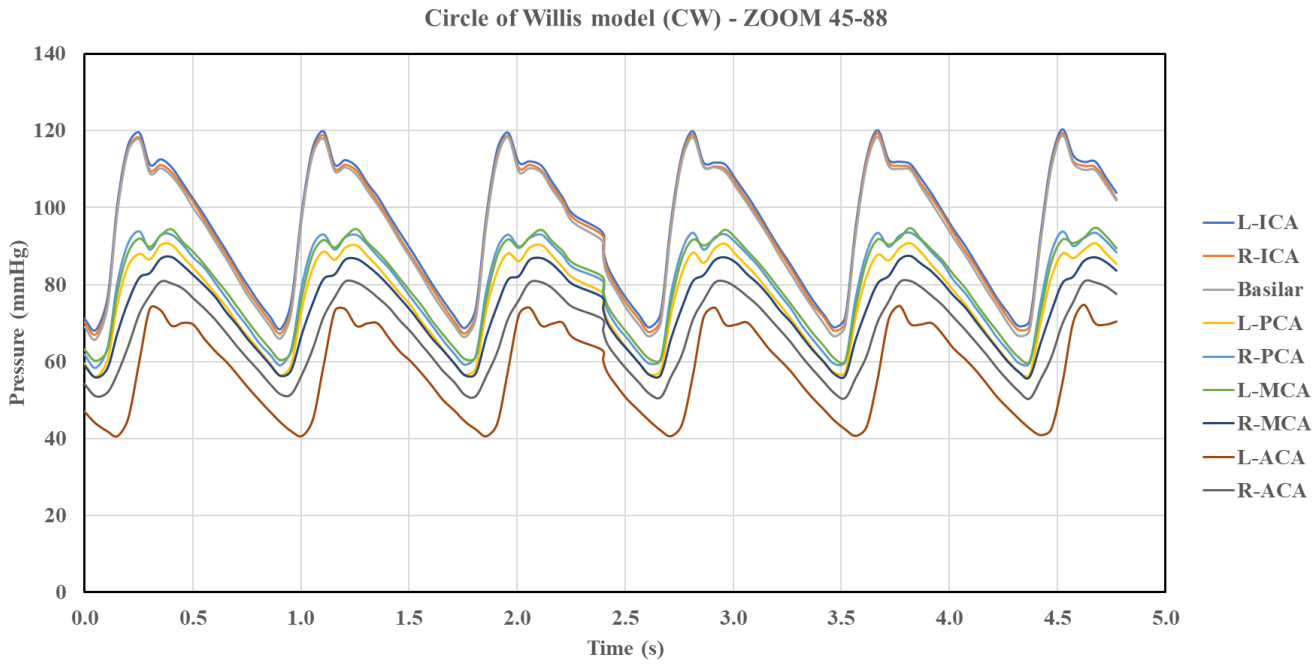

Figure 70: Control group for BM1: Pressure waveforms for the different branches in the CW model.

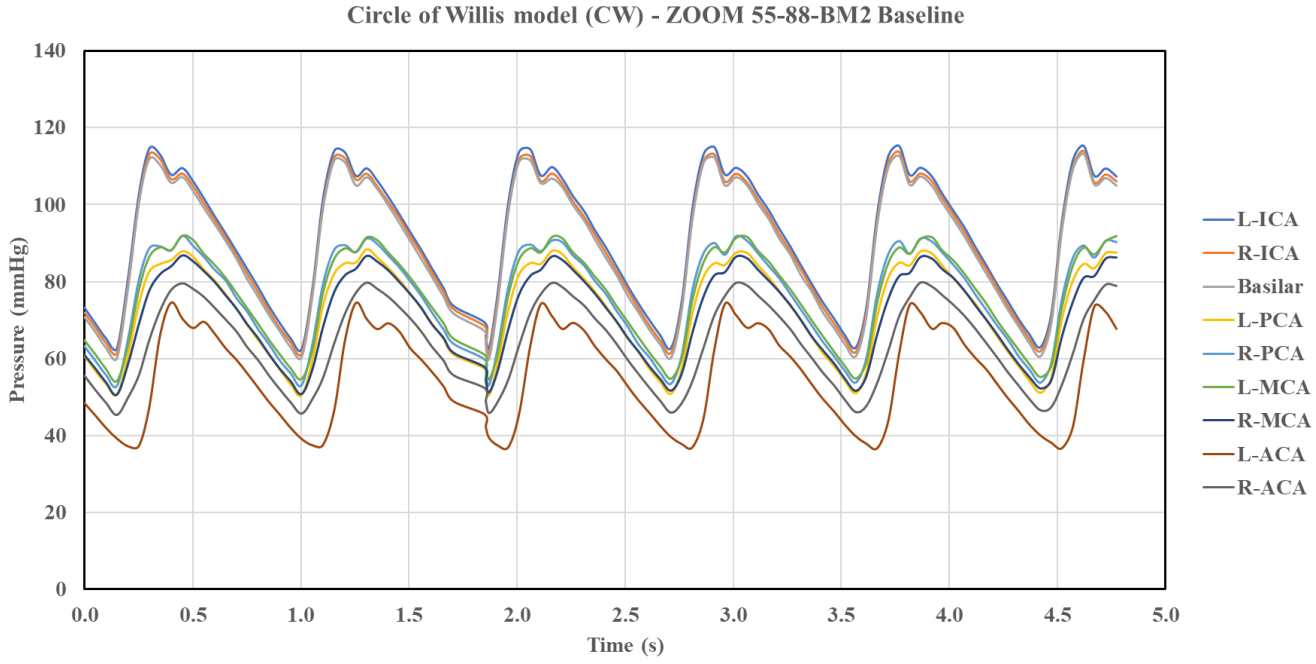

Figure 71: Control group for BM2: Pressure waveforms for the different branches in the CW model.

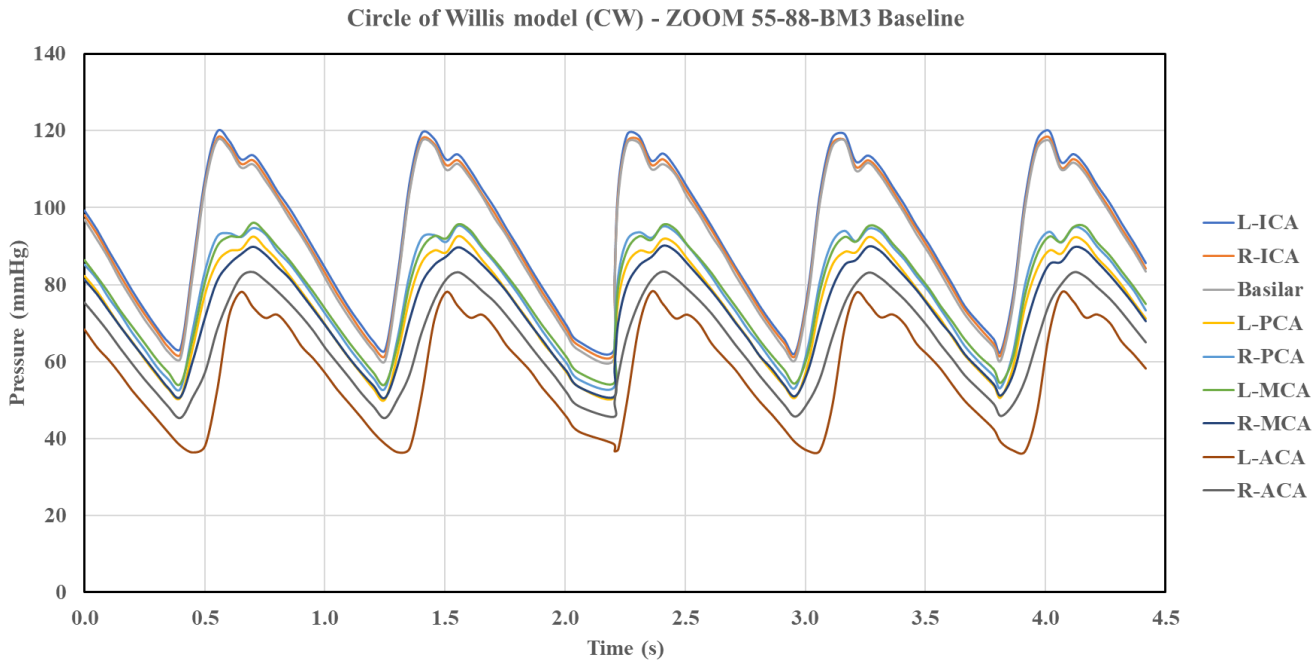

Figure 72: Control group for BM3: Pressure waveforms for the different branches in the CW model.

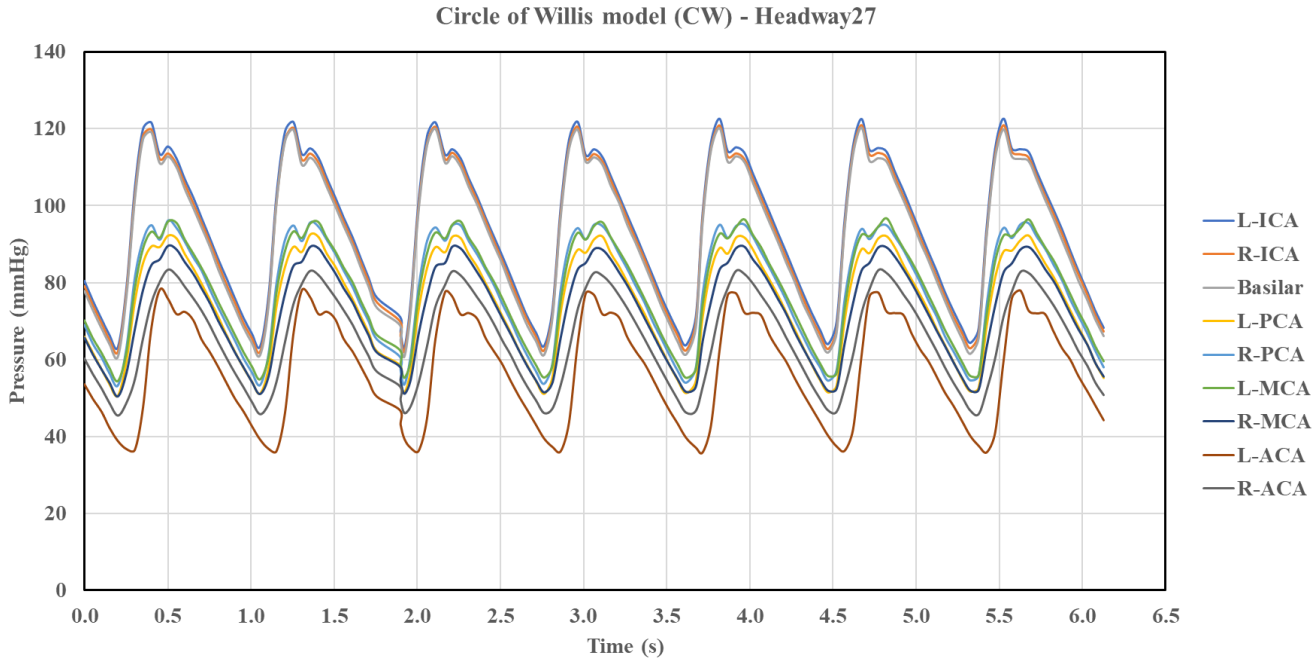

Figure 73: Control group for PED: Pressure waveforms for the different branches in the CW model.

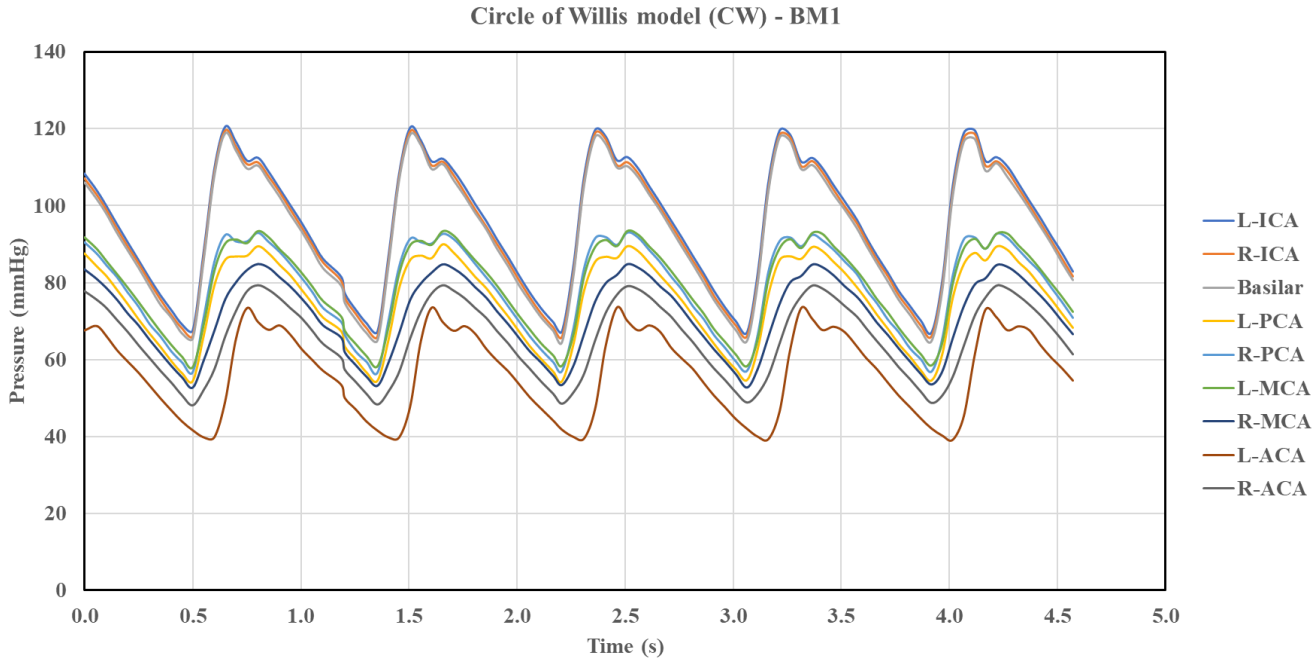

Figure 74: BM1: Pressure waveforms for the different branches in the CW model.

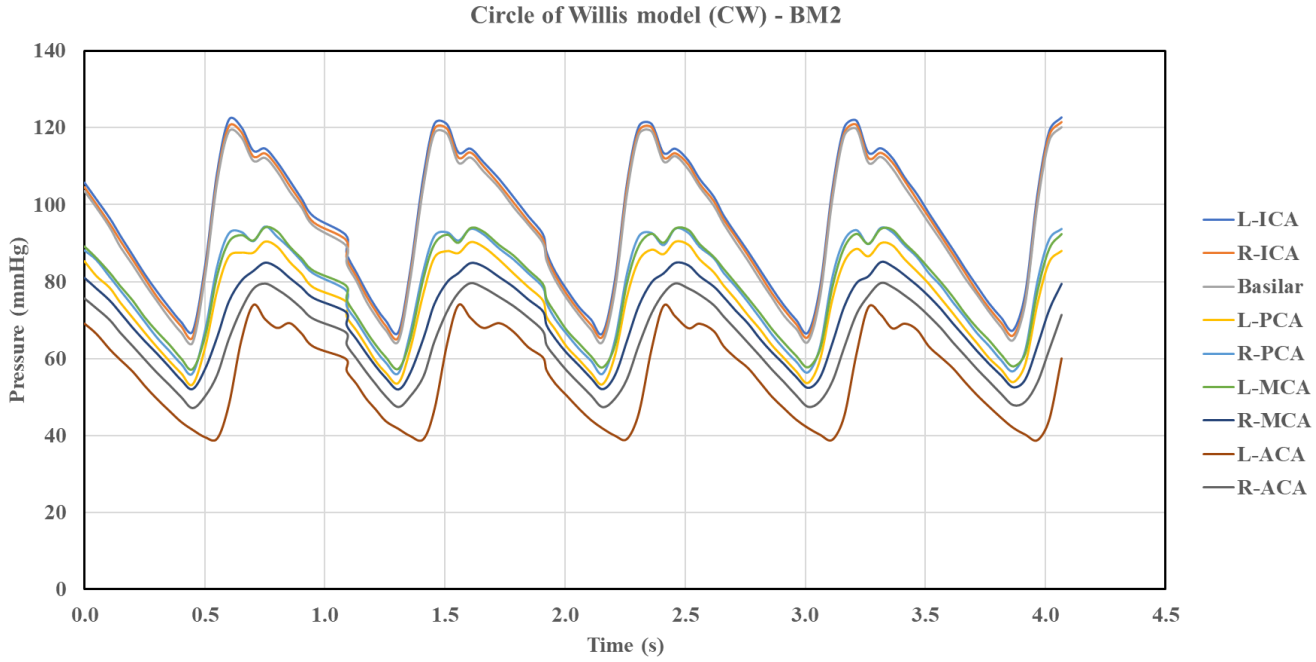

Figure 75: BM2: Pressure waveforms for the different branches in the CW model.

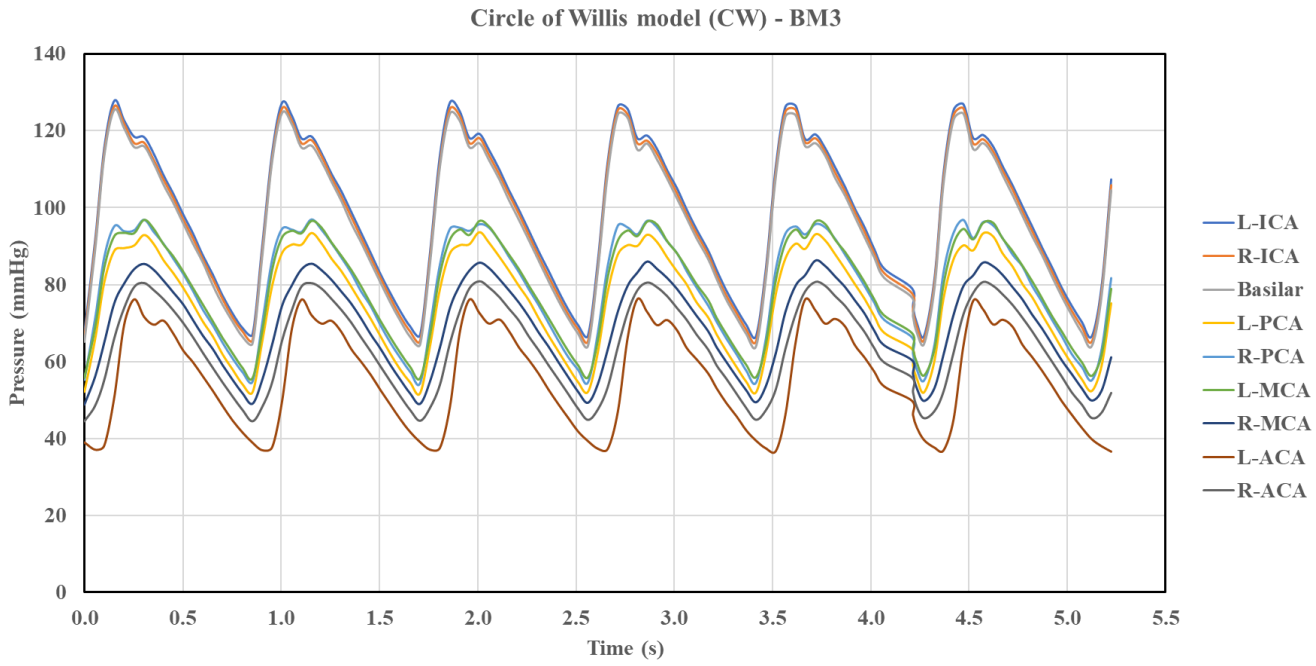

Figure 76: BM3: Pressure waveforms for the different branches in the CW model.

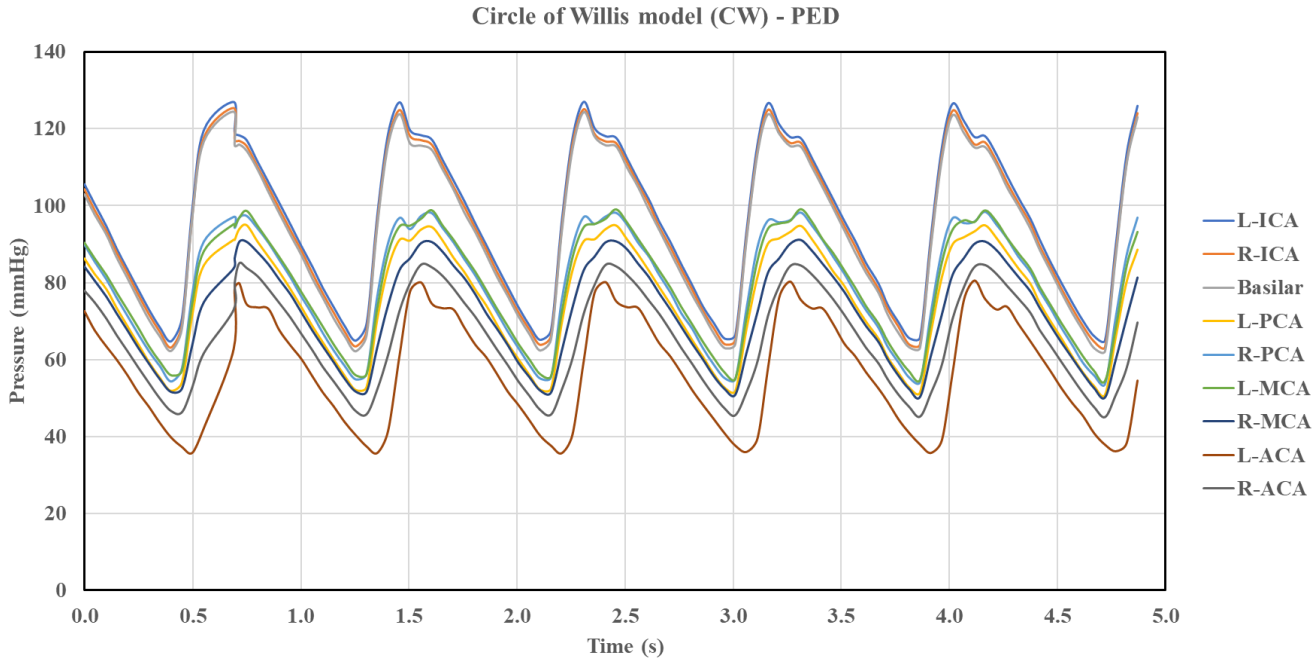

Figure 77: PED: Pressure waveforms for the different branches in the CW model.